NASA CR - 175119

NASA-CR-175119
19860017944

ADVANCED ELECTRIC PROPULSION

AND

SPACE PLASMA CONTACTOR RESEARCH

Prepared For

LEWIS RESEARCH CENTER

NATIONAL AERONAUTICS AND SPACE ADMINISTRATION

Grant NGR-06-002-112

Annual Report

January 1986

Paul J. Wilbur
Department of Mechanical Engineering
Colorado State University
Fort Collins, CO 80523

DISPLAY 08/2/1

86N27416** ISSUE 18 PAGE 2870 CATEGORY 20 RPT#: NASA-CR-175119 NAS 1.26:175119 CNT#: NGR-06-002-112 86/01/00 151 PAGES UNCLASSIFIED DOCUMENT

UTTL: Advanced electric propulsion and space plasma contactor research TLSP: Annual Report, 1 Oct. 1984 - 1 Jan. 1986

AUTH: A/WILBUR, P. J.

CORP: Colorado State Univ., Fort Collins. CSS: (Dept. of Mechanical Engineering.) AVAIL.NTIS

SAP: HC A08/MF A01

CIO: UNITED STATES

MAJS: /*COLD PLASMAS/*ELECTRIC PROPULSION/*ELECTROSTATIC ENGINES/*HOLLOW CATHODES/*MERCURY ION ENGINES/*RARE GASES/*SPACE PLASMAS

MINS: / ELECTRODYNAMICS/ PLASMAS (PHYSICS)/ TETHERING

ABA: Author

ABS: A series of experiments performed on an 8 cm dia. ring cusp magnetic field ion thruster are described. The results show the effects of anode and cathode position and size, ring cusp axial location and discharge chamber length on plasma ion energy cost and extracted ion fraction. Thruster performance is shown to be improved substantially when optimum values of these parameters are used. Investigations into the basic plasma phenomena associated with the process of plasma contacting are described. The results show the process of electron collection from a background plasma

ENTER:

1. Report No.	2. Government Accession No.	3. Recipient's Catalog No.
NASA CR 175119		

4. Title and Subtitle	5. Report Date
ADVANCED ELECTRIC PROPULSION AND SPACE PLASMA CONTACTOR RESEARCH	Jan. 1986
	6. Performing Organization Code
7. Author(s)	8. Performing Organization Report No.
Paul J. Wilbur	
	10. Work Unit No.
9. Performing Organization Name and Address	
Department of Mechanical Engineering Colorado State University Fort Collins, Colorado 80523	11. Contract or Grant No. NGR-06-002-112
	13. Type of Report and Period Covered Annual, Oct. 1, 1984-Jan. 1 1986
12. Sponsoring Agency Name and Address	14. Sponsoring Agency Code
National Aeronautics and Space Administration Washington, D.C. 20546	

15. Supplementary Notes

Grant Monitor - Vincent K. Rawlin, NASA Lewis Research Center, Cleveland, Ohio 44135

16. Abstract

A series of experiments performed on an 8 cm dia. ring cusp magnetic field ion thruster are described. The results show the effects of anode and cathode position and size, ring cusp axial location and discharge chamber length on plasma ion energy cost and extracted ion fraction. Thruster performance is shown to be improved substantially when optimum values of these parameters are used. Investigations into the basic plasma phenomena associated with the process of plasma contacting are described. The results show the process of electron collection from a background plasma to a hollow cathode plasma contactor exhibits a higher impedance than the process of electron emission from the hollow cathode. The importance of having cold ions present to facilitate the plasma contacting process is shown. Results of experiments into the behavior of hollow cathodes operating at high interelectrode pressures (up to $\sim$ 100 Torr) on nitrogen and ammonia are presented. They suggest that diffuse emission from the insert of a hollow cathode can be sustained at high interelectrode pressures if the cathode is made of non-conducting material and the cathode internal pressure is reduced by evacuating the cathode interior. A theoretical model of discharge chamber operation developed for inert gas thrusters is extended so it can be used to evaluate the performance of mercury ion thrusters. Predictions of the model are compared to experimental results obtained on two 30 cm dia. thrusters.

17. Key Words (Suggested by Author(s))	18. Distribution Statement
Electrostatic Thruster Hollow Cathode Electrodynamic Tether Plasma Contactor	Unclassified - Unlimited

19. Security Classif. (of this report)	20. Security Classif. (of this page)	21. No. of Pages	22. Price*
Unclassified	Unclassified	145	

* For sale by the National Technical Information Service, Springfield, Virginia 22161

NASA-C-168 (Rev. 10-75)

LIST OF FIGURES

LIST OF TABLES

RING CUSP DISCHARGE CHAMBER PERFORMANCE OPTIMIZATION*

Jeffrey M. Hiatt

Introduction

Over the years discharge chamber dimensions and magnetic field configurations and strengths have been altered in a continuing effort to improve ion thruster improve discharge chamber performance. The detailed mechanisms by which such design alterations induce performance changes have, however, not been well understood. As a result it has been difficult to separate out the cause-and-effect relationships associated with each of the thruster design variables and it has therefore not been possible to develop models that facilitate design of new thrusters without experimental optimization. Recently, however, both a model that enables one to describe discharge chamber performance in terms of two physically meaningful parameters (plasma ion energy cost and extracted ion fraction) and an experimental technique that can be applied to measure these parameters have been proposed.[1,2]

An objective of the work described herein has been to apply this experimental technique to determine the effects of changes in anode and cathode locations and magnetic field shape on these key performance parameters. A further objective has been to apply the discharge chamber model to infer the mechanisms by which such changes induce improvements in discharge chamber performance.

---

* This is a revision of AIAA paper No. 85-2007 presented at the 18th International Electric Propulsion Conference in October 1985.

A small (8 cm diameter) thruster has been selected for this study because a small thruster should tend to perform more poorly than a larger one[2] and it was expected that the performance of a small thruster would be more sensitive to the geometric changes being investigated. The ring cusp discharge chamber design[3] was selected for the study because it shows substantial promise as a very efficient configuration for ion thruster applications.

Apparatus and Procedure

The side schematic view of the 8 cm dia. discharge chamber used in these studies is shown in Fig. 1a. A unique feature of this discharge chamber design is its loop anode which can be moved axially during operation (variable ℓ_a) by means of the lead screw, yoke and guidepost assembly. This capability, coupled with the option of installing anode loops varying in diameter (d_a) from 4 cm to 6.6 cm, facilitates investigation of the effects of changes in the position of the anode relative to the magnetic ring cusp on the performance of a discharge chamber. The loop anode was selected for the study because its axisymmetric configuration and small cross section facilitate the definition of a small circular zone at which electrons are being extracted from the plasma.

While the various anode loops could be moved either upstream or downstream of the cusp location, preliminary tests[4] showed that performance was always best when they were moved downstream toward the grids. It is postulated that upstream anode movement gives poorer performance because it induces a greater fraction of the total ion production upstream of the cusp and the probability of an ion being extracted into the beam from this region is lower than the probability for extraction of an ion from a region closer to the grids. For the data presented herein only anode positions downstream of the loop anode will be investigated and values of ℓ_a will be positive. The magnetic field for the

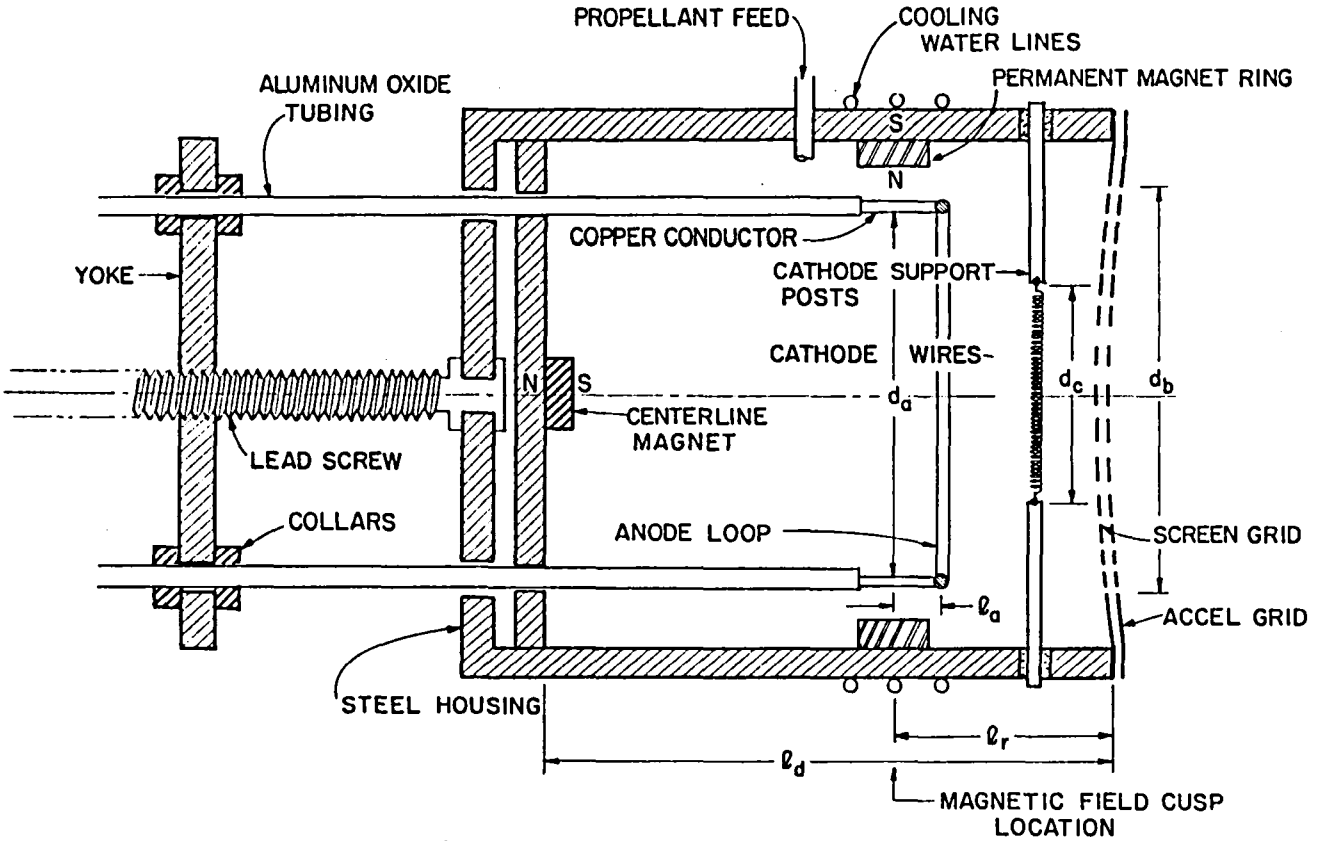

a. MOVABLE LOOP ANODE

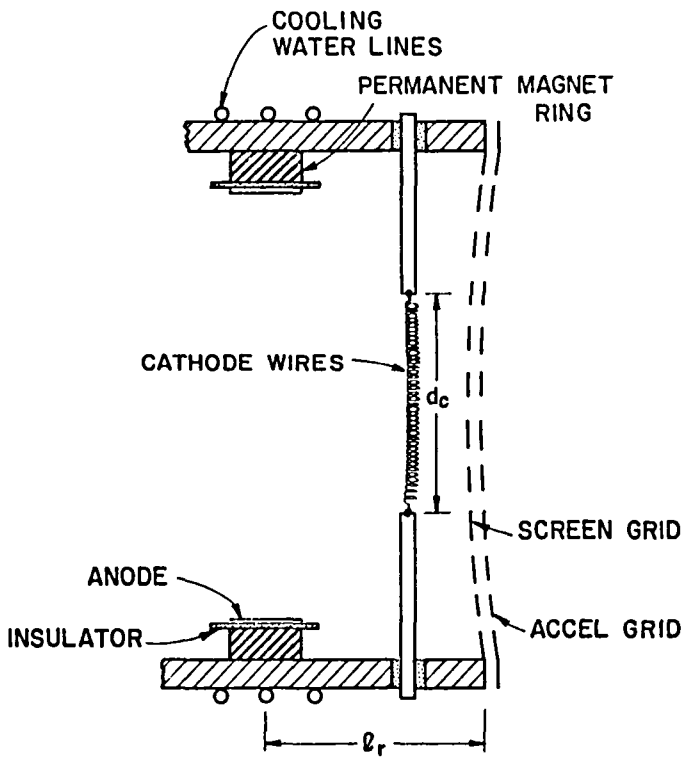

b. ANODE ON CUSP

Fig. 1 Ion Source Configurations

thruster of Fig. 1a is produced by small samarium cobalt magnets placed end-to-end to form a ring located a distance ℓ_r upstream of the grids and the samarium cobalt upstream centerline magnet shown. These magnets have a flux density of 0.27 T at their surfaces and they are arranged so the polarity on the outer surface of the ring of magnets (or ring magnet) is opposite to that at the outer surface of the centerline magnet.

While most tests were run with the movable anode configuration of Fig. 1a, it was considered important to compare performance measurements made with this apparatus to those made with the anode located at the magnetic field cusp on the surface of the magnet. The ion source was modified for this comparative test by removing the anode loop, yoke, and lead screw of Fig. 1a and installing the thin sheet steel anode adjacent to but isolated from the magnet ring surface by the thin flexible mica insulator shown in Fig. 1b.

Electrons were supplied to the discharge from a toroidal, thermionic cathode located 1.5 cm upstream of the screen grid so its axis would be coincident with the discharge chamber axis (Fig. 1a). The major diameter of the cathode torus (d_c) could be varied by altering the cathode support post heights. The total length of the 0.25 mm dia. tungsten wire used to fabricate the torus was always the same. It was formed into a spiral coil which was stretched to various extents to produce cathode torus major diameters that ranged from 1 cm to 6 cm. The ion beam diameter (d_b), which could be varied by changing the extent to which the screen grid was masked down, was 8 cm unless noted otherwise. The discharge chamber length (ℓ_d), which could also be varied, was generally maintained at 11.8 cm. The upstream distance from the screen grid to the ring cusp (ℓ_r) was 3.7 cm unless noted otherwise. The physical transparencies of the screen and accelerator grids were 0.68 and 0.54 respectively.

In conducting specific tests the discharge voltage (V_D) was held constant at 50 v, the argon flow rate ($\dot{m}$) was varied over the range 100 to 700 mA eq. and at each flow rate the discharge current (J_D) was varied through the range $\sim$0.1 to $\sim$2 A. At each operating condition the variables just identified, the beam current (J_B), and the total ion production rate (J_p) were measured. When the movable anode was installed it was positioned initially at the axial location of the magnetic field cusp produced at the ring magnet ($\ell_a = 0$) and it was then moved downstream after each sequence of data collection. When the anode had been moved too far from the axial location of the magnetic field cusp the discharge would go out. The axial location of the anode at which this occurred repeatedly for a given anode loop diameter will be referred to herein as the extinction point for that anode loop diameter. More detailed descriptions of the apparatus and procedures used in conducting these tests are presented in References 4 and 5.

The test results will be presented in terms of the parameters describing the energy cost of a plasma ion (ε_p) and the fraction of ions produced that are extracted into the beam (f_B). These parameters have been computed from experimental data using the equations.[2]

$$f_B = J_B/J_p \tag{1}$$

$$\varepsilon_p = (J_D - J_p)\, V_D/J_p \tag{2}$$

All the quantities appearing on the right hand sides of these equations except the ion production current were measured directly. The ion production current was measured by biasing the thruster body and screen grid $\sim$30v negative of

cathode potential to repel electrons so the ion currents to each of these surfaces could be measured. The sum of ion currents to these surfaces and the beam current approaches the total ion production current (J_p).*

Data will also be presented herein in terms of the neutral density parameter. This parameter, which is proportional to the neutral density in the discharge chamber is defined by the expression $\dot{m}(1-\eta_u)$ where $\dot{m}$ is the propellant flow rate into the thruster and η_u is the propellant utilization efficiency. It has been shown by Brophy[2] that the plasma ion energy cost is related to the neutral density parameter by the equation

$$\varepsilon_p = \varepsilon_p^* \left[1 - e^{-C_o \dot{m}(1 - \eta_u)}\right]^{-1} . \qquad (3)$$

In this equation the parameter ε_p^*, the baseline plasma ion energy cost, is the average energy required to produce an ion at high neutral densities. When the neutral density is sufficiently high, primary electrons are not lost directly to the anode and the only losses associated with ion production are those related to atomic excitation reactions and Maxwellian electron energy losses to the anode. A more detailed description of the relationship between Maxwellian electron losses and the baseline plasma ion energy cost, including a model for calculating this cost, is contained in Ref. 2. The other parameter contained in Eq. 3, the primary electron utilization factor, C_o, is given by the equation

---

* The error between the true ion production current and the measured one is due to the collection of ions on the anode and the cathode wires and support posts. This error should be small because the effective collection areas of these surfaces are small compared to the total area exposed to the plasma.[2]

$$C_o = \frac{4\sigma_o' \ell_e}{e v_o A_g \phi_o} \qquad (4)$$

where σ_o is the total inelastic collision cross section for primary electron-neutral atom collisions, ℓ_e is the primary electron containment length (i.e. the average distance primary electrons would travel in the thruster before they would reach the anode if they had no inelastic collisions), e is the electron charge, A_g is the grid area, ϕ_o is the grid transparency to neutral atoms, and v_o is the mean velocity of the neutral atoms. A higher value of C_o is indicative of good primary electron containment.

While the plasma ion energy cost and extracted ion fraction are useful in determining the cause-and-effect relationships that are the focus of this work, it is the beam ion energy cost (ε_B) that is of primary concern to a propulsion system designer. This beam ion energy cost is related to the other two parameters through the equation[2]

$$\varepsilon_B = \frac{\varepsilon_p}{f_B} + \frac{1-f_B}{f_B} V_D \quad . \qquad (5)$$

Hence data presented in the form of plasma ion energy costs and extracted ion fractions can be readily converted into beam ion energy cost data.

Experimental Results

Effect of Anode Axial Position on Plasma Ion Energy Cost

As the anode loop shown schematically in Fig. 1a was moved downstream from the axial location of the magnetic field cusp the plasma ion energy cost was observed to decrease continuously until it reached a point where the discharge extinguished. The lowest (optimum) plasma ion energy cost was realized as this threshold of discharge extinction was approached. The extent of the reduction

in plasma ion energy costs induced by changing the region of electron collection from the surface of the cusp (configuration of Fig. 1b) to the downstream loop anode location where discharge extinction is approached (configuration of Fig. 1a) is seen by comparing the square and circular data symbols on Fig. 2. The parameters associated with each curve shown (ε_p^* and C_o) are the ones that correspond to the best fit of Eq. 3 to the data. The higher value of C_o associated with the optimized anode location data of Fig. 2 reflects a corresponding improvement in the primary electron containment when the anode is positioned properly (specifically this comes about because of an increase in the primary electron containment length, ℓ_e). The lower value of ε_p^* observed when the anode loop is in its optimum location is probably due to lower Maxwellian electron energy losses to the anode although it may also reflect reduced ion losses to the anode.

It is noteworthy that the square symbol data of Fig. 2, while they do tend collectively to follow the theoretical curve shown, may not follow it well at any one flow rate (e.g. at 178 mA eq.). This tendency to depart from the theory embodied in Eq. 3 as neutral density is reduced at a given flow rate was also observed by Brophy.[2] The departure is believed to be caused by an increase in the average energy of the Maxwellian electrons collected at the anode that tends to accompany reductions in neutral density (i.e. increases in propellant utilization efficiency) at some operating conditions. Such a change would induce an increase in the value of the parameter ε_p^* which has been held constant to obtain the curves of Fig. 2.

Effect of Anode Position on Extracted Ion Fraction and Beam Ion Energy Cost

It is apparent from Eq. 5 that the extracted ion fraction (f_B) can have a

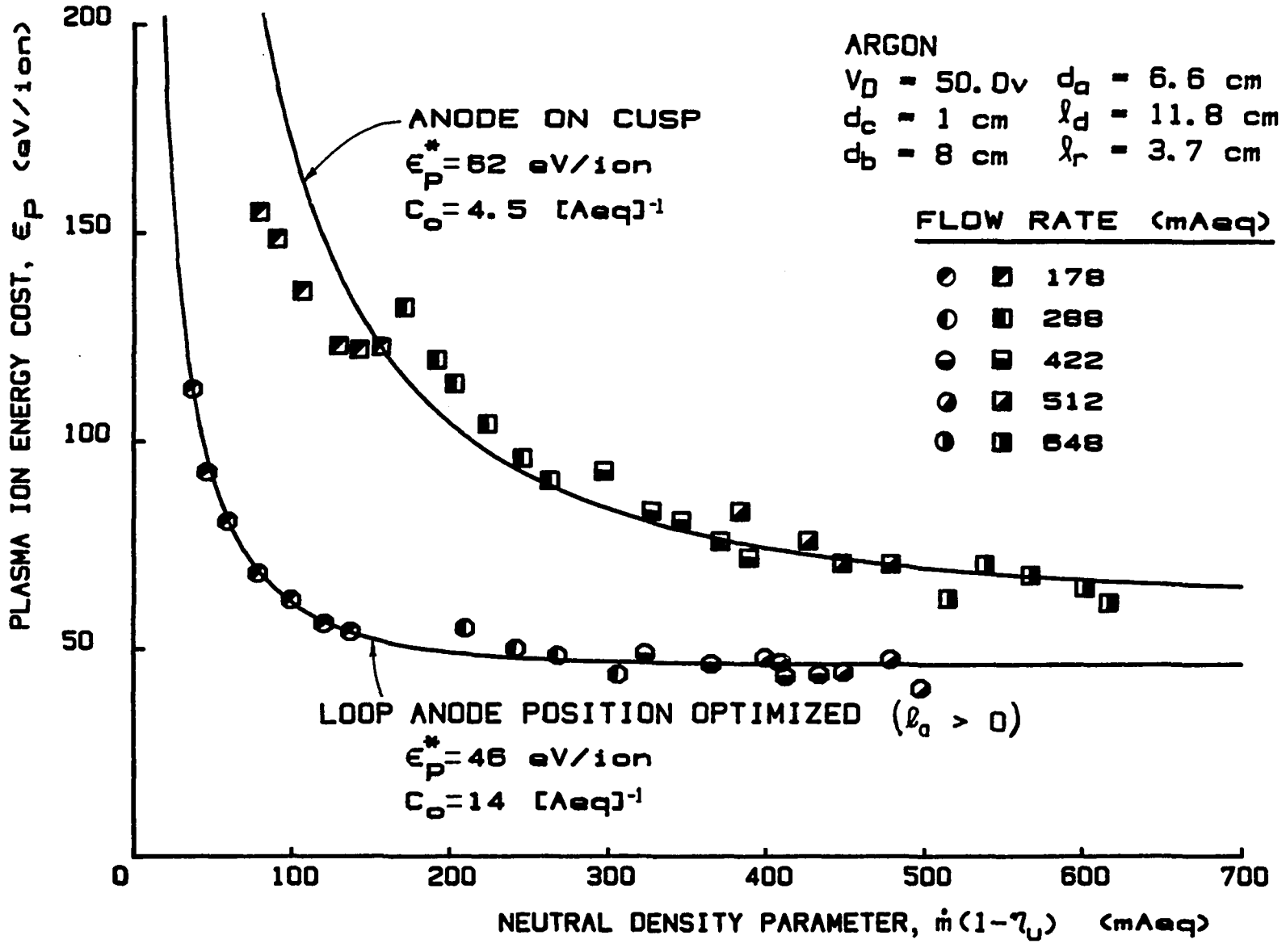

Fig. 2 Typical Results Showing the Effect of Anode Position on Plasma Ion Energy Costs

dominant effect on the beam ion energy cost (ε_B). In these tests it was found, however, that anode movement from the cusp location to the optimized location did not induce significant changes in the extracted ion fraction. Typically it was found that varying the anode axial location from the position over the cusp to the discharge extinction point and varying flow rates over the range given in Fig. 2 resulted in an extracted ion fraction that remained at $f_B = 0.23 \pm 0.02$. Hence, the minimum beam ion energy cost was realized when the plasma ion energy cost was a minimum (i.e. at the optimized anode location). The extent of the typical performance improvement induced in more traditional performance curves by moving the anode from the cusp to the optimized anode location is shown in Fig. 3. These typical performance curves have been computed using Eqs. 3 and 5 the values of the parameters (ε_p^*, C_o) associated with the data of Fig. 2, a mass flow rate of 250 mAeq and $f_B = 0.23$. Experimental data points are not given on Fig. 3 or other performance curves (ε_B vs. η_u) appearing in this paper because the focus of the tests was measurement of plasma ion energy costs and extracted ion fractions and control of the many experimental parameters was not always adequate to assure small data scatter on the performance curves. For example, the data of Fig. 2 were collected with toroidal cathodes which had slightly different major diameters. This variation in diameter did not affect the plasma ion energy cost curves, but it did affect the extracted ion fractions. A subsequent test demonstrated the minor effect anode position and flow rate had an extracted ion fraction. The plots of Fig. 3 represent therefore what would be expected if everything but anode position were held constant.

Optimum Anode Locations Relative to the Magnetic Field Lines

A series of tests was conducted to determine how the optimum anode axial position varied as the anode diameter was changed. With the beam diameter,

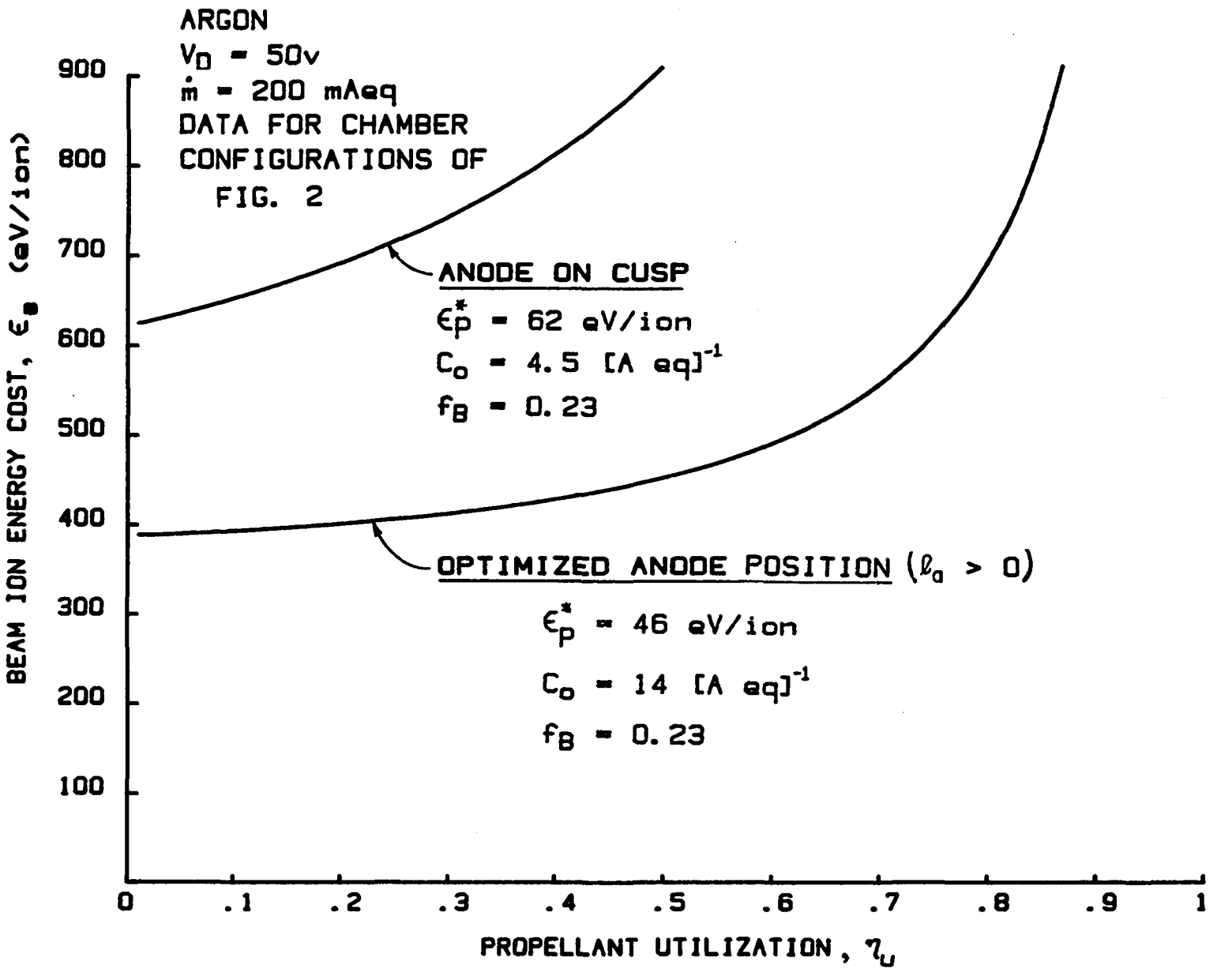

Fig. 3 Typical Effect of Anode Position on Thruster Performance

discharge chamber length and cathode diameter held as near the same as possible, the chamber was operated in three tests, each characterized by an anode loop with a different major diameter. When the anode was moved near the discharge extinction point in each of these three tests, the performance was again observed to be optimized. The most striking feature of the test results, however, was that the resulting plasma ion energy cost/neutral density parameter data points measured at these optimized anode positions fell on a common curve. This curve is shown along with the data points corresponding to each anode diameter in Fig. 4. The consistency of these data illustrates that proper placement of any anode potential surface within the discharge chamber yields the same optimum discharge chamber performance. This consistency is also reflected in the parameters C_o and ε_p^* used to define the curve fit of the separate sets of data in Figs. 2 and 4. The values of these parameters are observed to agree exactly in the case of ε_p^* and to within $\pm$ 10% in the case of C_o. It is noteworthy that for the 4 cm dia. anode, the performance remained at the same high level as the anode was moved through a rather large range of axial positions (0.95 cm $\leq \ell_a \leq$ 2.0 cm).

Some insight into why the locations of the anode loop identified in Fig. 4 yield this optimum performance can be gained by plotting the optimum anode loop positions on the iron filings map of the magnetic field shown in Fig. 5. This iron filings map was made using a new technique[4] developed for high field strength permanent magnet ion thrusters. Careful examination of these anode locations suggests that to first order they fall along a common magnetic field line. Since performance was optimum for each of anode positions plotted in Fig. 5 they lie along the optimum virtual anode field line and its surface of revolution would represent the optimum surface for collecting electrons.[6] In more general terms one can say that the same peformance is achieved in a

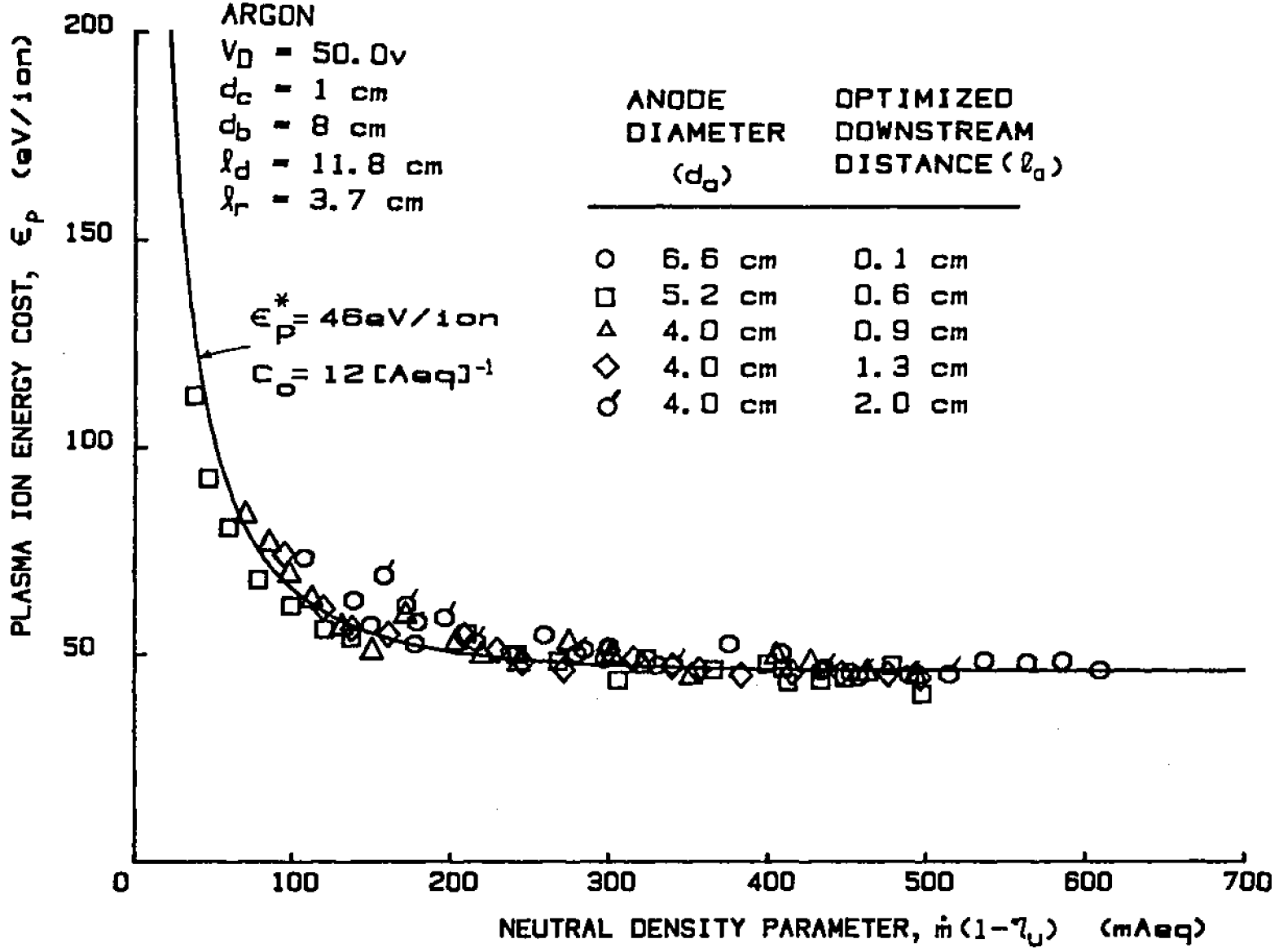

Fig. 4 Effect of Anode Diameter on Plasma Ion Energy Cost Curve for Anode Axial Position Optimized

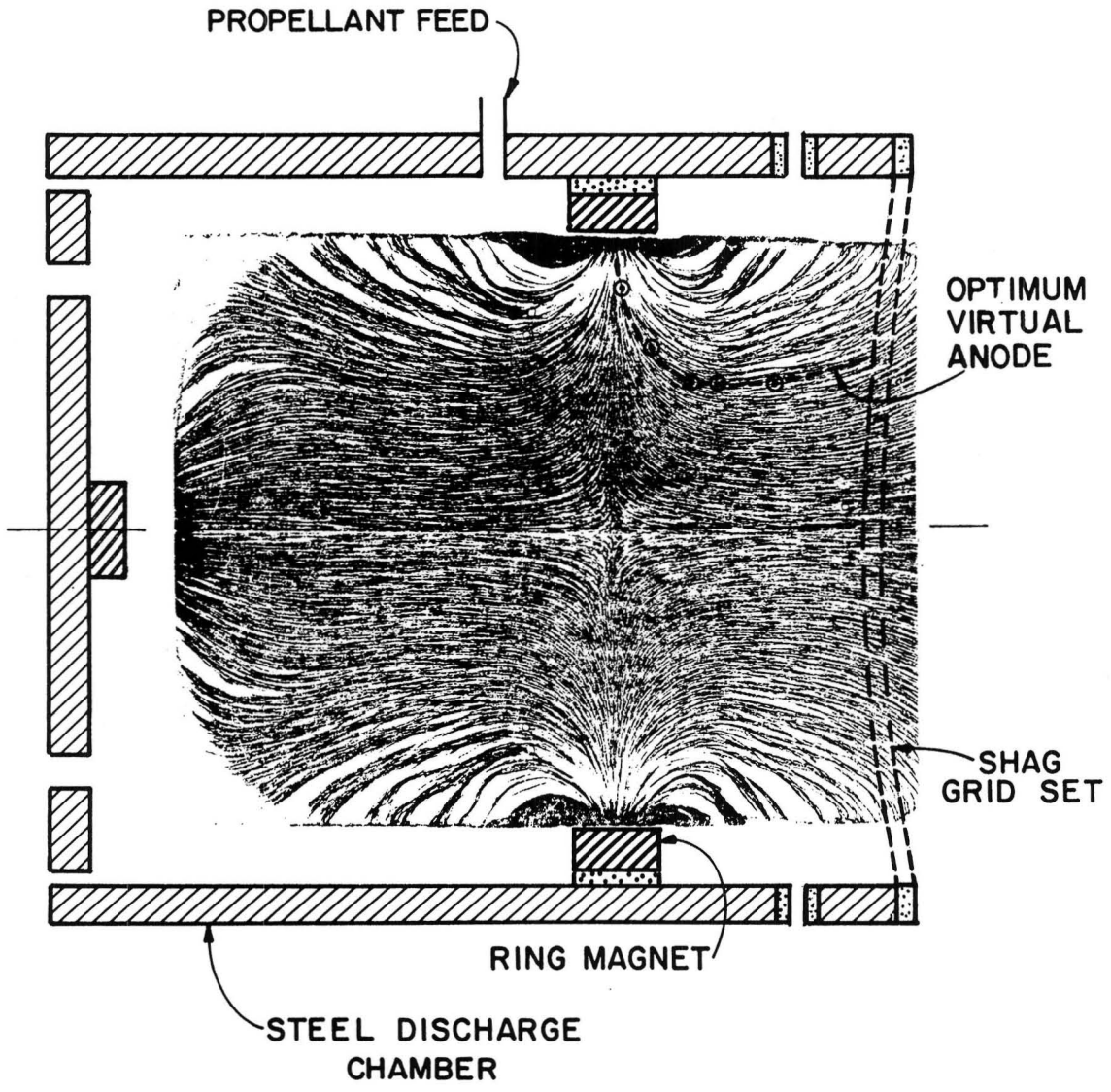

Fig. 5 8 cm dia. Ring Cusp Thruster Magnetic Field Map

discharge chamber for an anode positioned to collect electrons at any place along the surface of revolution of a given virtual anode field line and this performance is optimized when this field line is properly selected.

The effect of the alignment between the direction of anode motion and the direction of the magnetic field lines on the distance over which the anode could be moved without inducing substantial changes in the plasma ion energy cost are illustrated by the data in the legend of Fig. 4. These data show the 4 cm dia. anode loop could be moved axially for more than 1 cm, and because it was moving along the optimum virtual anode field line, shown in Fig. 5, the plasma ion energy cost remained essentially constant. With the 6.6 cm dia. anode loop in place, however, axial movement was essentially normal to the field lines (Fig. 5) and a mere 0.5 mm upstream movement from the location of discharge extinction caused substantial increases in plasma ion energy costs. A preferred anode diameter (i.e. one that is least sensitive to anode axial position) was for this experiment, therefore, one which allowed the anode loop to move along the optimum virtual anode field line at the location where this field line ran parallel to the axis of the discharge chamber.

As the anode loop was moved downstream during typical investigations of anode position on performance it was observed that on some occasions the plasma ion energy cost was decreasing dramatically as the point of discharge extinction was approached. On other occasions it was found that the anode could be moved over a substantial distance with no significant change in plasma ion energy cost. The distance over which the anode could be moved toward the point of discharge extinction with no substantial change in plasma ion energy cost was observed to be a function of both the neutral atom density and the extent to which the anode was being moved along magnetic field lines. Typical results

showing the effect of the neutral density parameter on the range of anode positions over which the plasma ion energy cost remained nearly constant can be seen in Fig. 6. Here the plasma ion energy cost is plotted against anode position (measured downstream from the cusp location). At a neutral density parameter of 145 mA eq. the curve drawn through the square data symbols shows a very sharp drop in the plasma ion energy cost as the anode loop is moved downstream of the magnetic ring cusp. In this case the discharge could not be sustained with the anode loop positioned beyond the 2 mm downstream position. Operating at a neutral density parameter of 480 mA eq. did, however, make it possible to vary the anode loop position through a range of about 1 mm while achieving approximately the same plasma ion energy cost. This increase in the range of acceptable anode positions is apparently related to an increase in the collision frequency of electrons with neutral atoms in the discharge plasma. This is presumably related in turn to the fact that an increased collision frequency facilitates electron migration across field lines.

An analytical criterion that could be used to identify the magnetic field line that defines the optimum virtual anode field line would be desirable. Research conducted to date gives some insight into the formulation of such a criterion. This research has shown that the position of this line should be measured relative to the position of the outermost magnetic field line that can receive primary electrons directly from the cathode. It should be noted that electrons from the cathode can migrate along magnetic fields within the discharge chamber with relative ease and they can also migrate inward, where there is no anode to collect them and where magnetic fields are weaker. Electrons released from the cathode should therefore fill the region within the surface of revolution of the magnetic field line that intersects the outer edge of

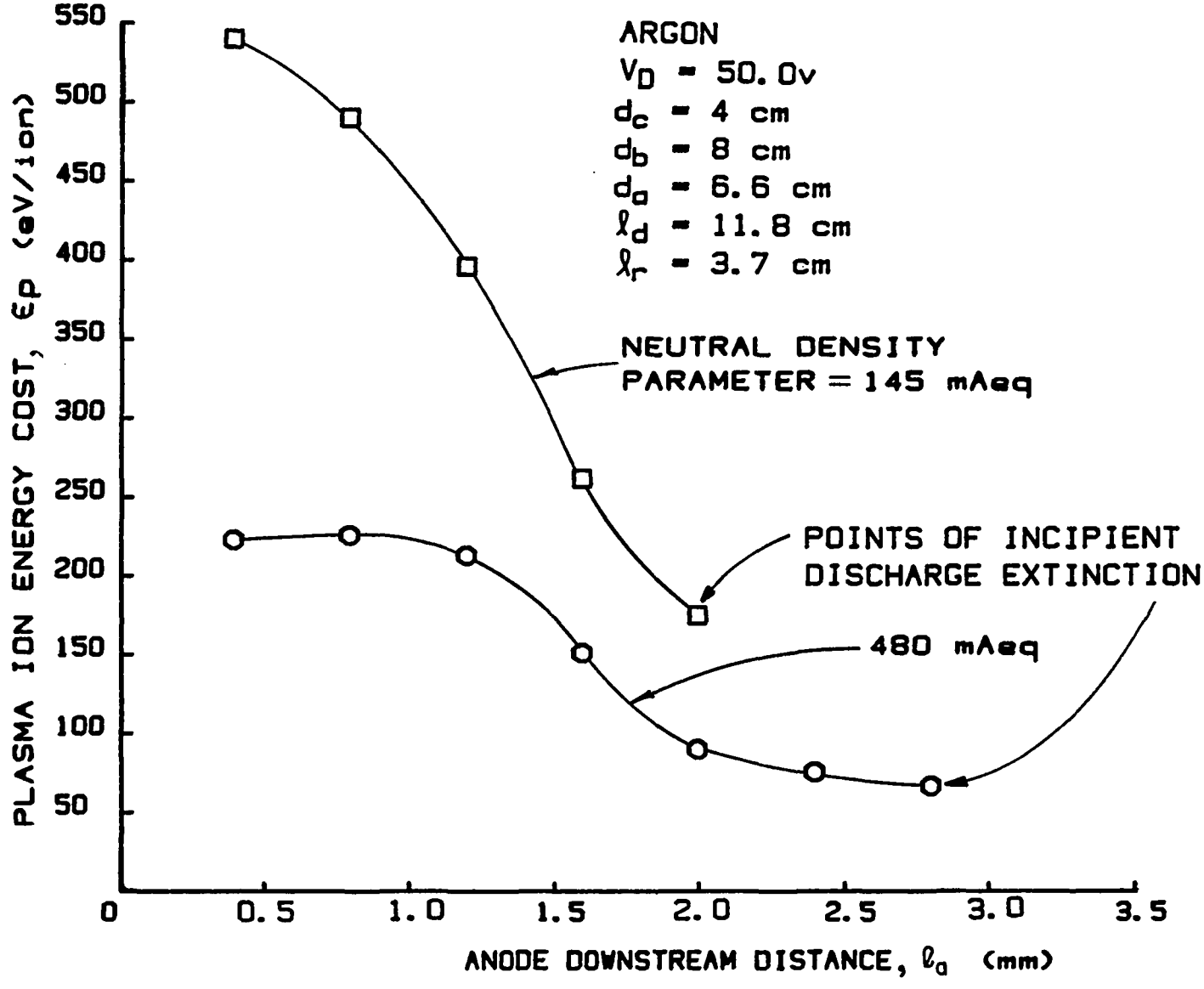

Fig. 6 Effect of Anode Position and Neutral Density on Plasma Ion Energy Cost

the cathode. This field line, which will be called the virtual cathode magnetic field line herein, has also been labeled the critical magnetic field line.[7] Figure 7 is an illustration showing the selected magnetic field lines within the discharge chamber that have just been defined. Primary electrons emitted from the cathode with diameter d_c would have access to the dotted region shown which is bounded by the solid virtual cathode field lines. These electrons would migrate through the cross-hatched region toward the optimum virtual anode field lines where they would be collected, usually as Maxwellian electrons. If these two field lines were too close together then significant numbers of primary electrons would reach the virtual anode and be lost and high plasma ion energy cost would result. If on the other hand the virtual anode and cathode field lines were too far apart the discharge would tend to extinguish. An example of a criterion that might be used to define an acceptable separation distance between the virtual field lines would be the magnetic field integral criterion suggested by Robinson.[8]

Effect of Ring Cusp Location on Performance

Based on the model just discussed ionization may be presumed to occur within the region bounded by the optimum virtual anode field lines of Fig. 7. For the magnetic field line configuration designated by the solid field lines of Fig. 7 this implies that the ion production region (dotted and cross hatched) does not extend to the outer ring of holes in the grid set and that the ion beam profile would be peaked. It might be postulated that this situation could be corrected by moving the ring magnet upstream and repositioning the anode onto the new optimum virtual anode line. The optimum virtual anode and the virtual cathode field lines that might be expected in this situation are shown as the dashed lines in Fig. 7. In order to test this hypothesis a test was run in

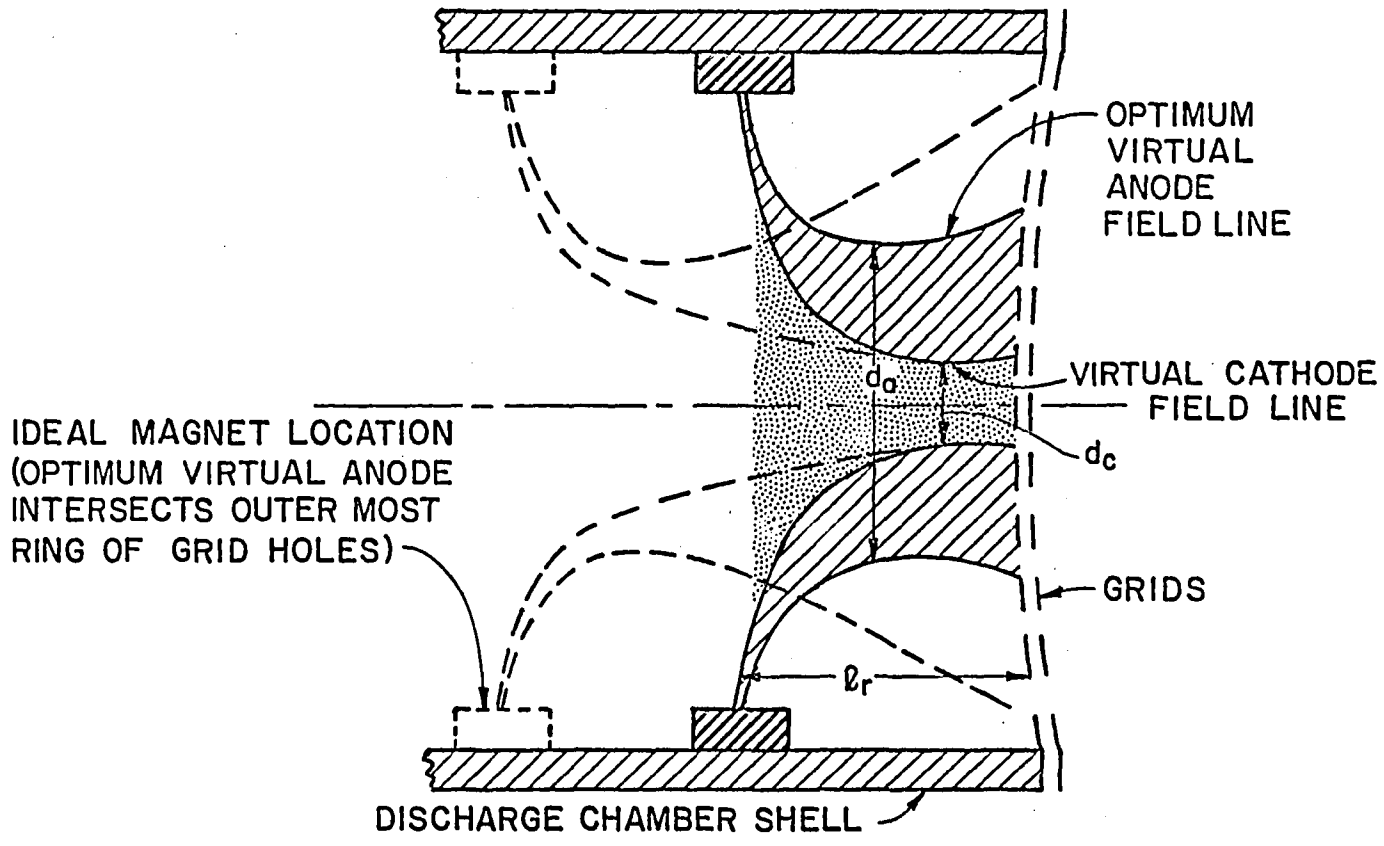

Fig. 7 Schematic Diagram of Important Magnetic Field Lines

which the ring cusp/screen grid separation distance (ℓ_r) was increased from the standard value (3.7 cm) to 4.5 cm. The results, which confirmed the hypothesis, showed that this change induced an increase in the extracted ion fraction from 23% to 33%. Further, an iron filings map taken with ℓ_r equal to 4.5 cm suggested qualitatively at least that the optimum virtual anode field lines shown dashed in Fig. 7 were realized.

Effect of Cathode Diameter on Performance

The cathode diameter d_c could also be increased to alter the ion production region from that shown in Fig. 7 so both the ion beam profile and extracted ion fraction would be improved. The anode would also have to be repositioned onto the new optimum virtual anode field line in this case to keep the plasma ion energy cost at its optimum level. The effect of cathode diameter on extracted ion fraction for the case where the anode position was readjusted to yield minimum plasma ion energy costs is shown in Fig. 8. These data were obtained at the discharge chamber configuration defined by Fig. 1a with the chamber configured to have the lengths and diameters cited in the legend of Fig. 8. These data show that the extracted ion fraction more than doubles as the cathode diameter (d_c) is increased from 1 cm to 4 cm. This improvement in the extracted ion fraction is believed to be caused in part by an increase in the grid area exposed to the primary electron plasma and in part by an increase in the fraction of the total ion production that is effected adjacent to the grids.

Increasing the diameter of the cathode has the adverse effect of increasing plasma ion energy costs as the curves of Fig. 9 illustrate. The actual data points on which these curves are based are not shown in this figure because there were a large number of them and they tend to complicate the figure without providing significant additional information. The increase in plasma ion energy

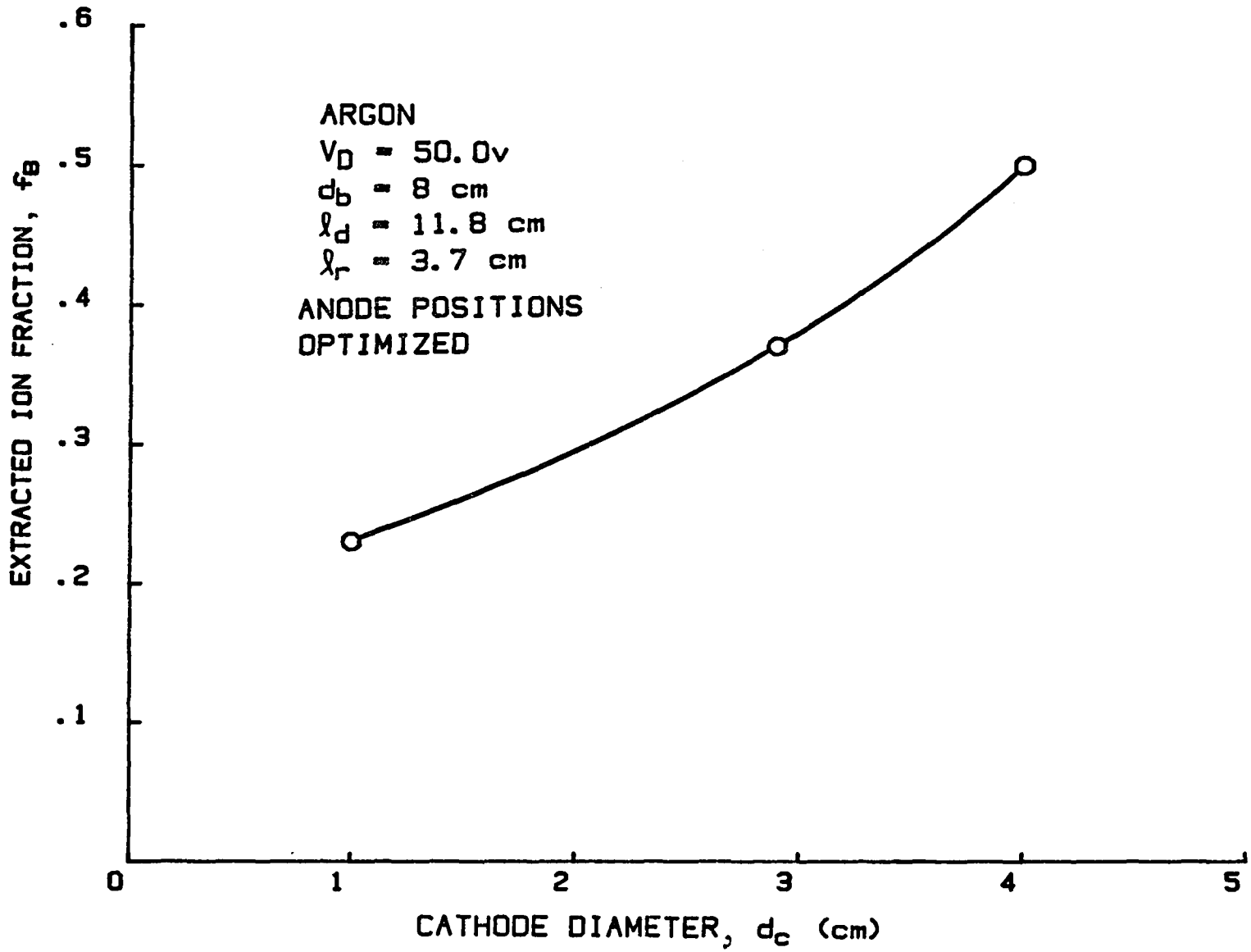

Fig. 8 Effect of Cathode Diameter on Extracted Ion Fraction

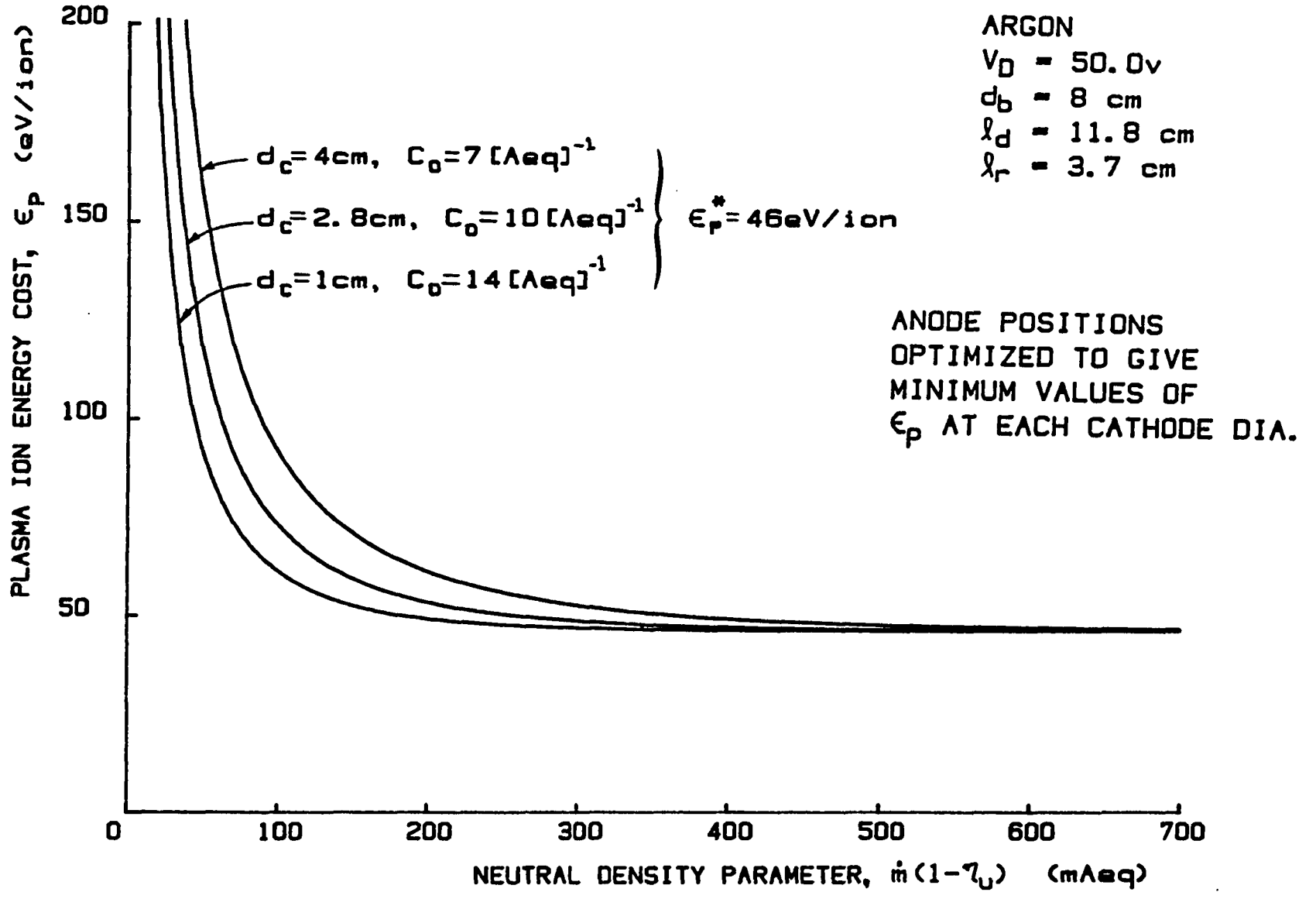

Fig. 9 Effect of Cathode Diameter on Plasma Ion Energy Cost

cost induced by increases in cathode diameter is shown in Fig. 9 to be relatively modest at low propellant utilization levels (high neutral density parameters). This is shown by the fact that increasing the cathode diameter from 1 cm to 4 cm leaves the baseline plasma ion energy cost unchanged. This change in cathode diameter is, however, observed to cause the primary utilization factor, C_o to decrease. Lower primary electron utilization factors imply less effective containment of the primary electrons in the discharge until after they have had inelastic collisions (cf. Eq. 4). This leads to the conclusion that larger diameter cathodes induce a larger primary electron loss rate to the anode. Fortunately the improvement in the extracted ion fraction (f_B) induced by increasing the cathode diameter outweighs the effect of the reduced primary electron utilization factor (C_o). As a result the overall performance of the discharge chamber is greatly improved by increases in cathode diameter. This is shown by the plots of Fig. 10 which present performance curves computed using Eqs. 3 and 5 and the curve fit values of the parameters f_B, ε_p^* and C_o identified on Figs. 8 and 9. Specifically they illustrate the dramatic improvement in performance achieved as cathode diameter (d_c) is increased from 1 cm to 4 cm and f_B, the extracted ion fraction, increases from 23% to 50%. The measured data are in excellent agreement with the curves of Fig. 10 up to the dashed lines, at which point the discharge could no longer be sustained at each particular operating condition. The dashed lines do, however, represent the performance projected by the model (Eqs. 3 and 5) at higher propellant utilizations.

The limitations on propellant utilization which prevented operation at values indicated by the dashed lines in Fig. 10 were due primarily to the fact that the anode loop was located too close to the final discharge extinction point. This limitation was mentioned in discussing Fig. 6 but it is described in more general terms by the data of Fig. 11. This figure shows a typical plot

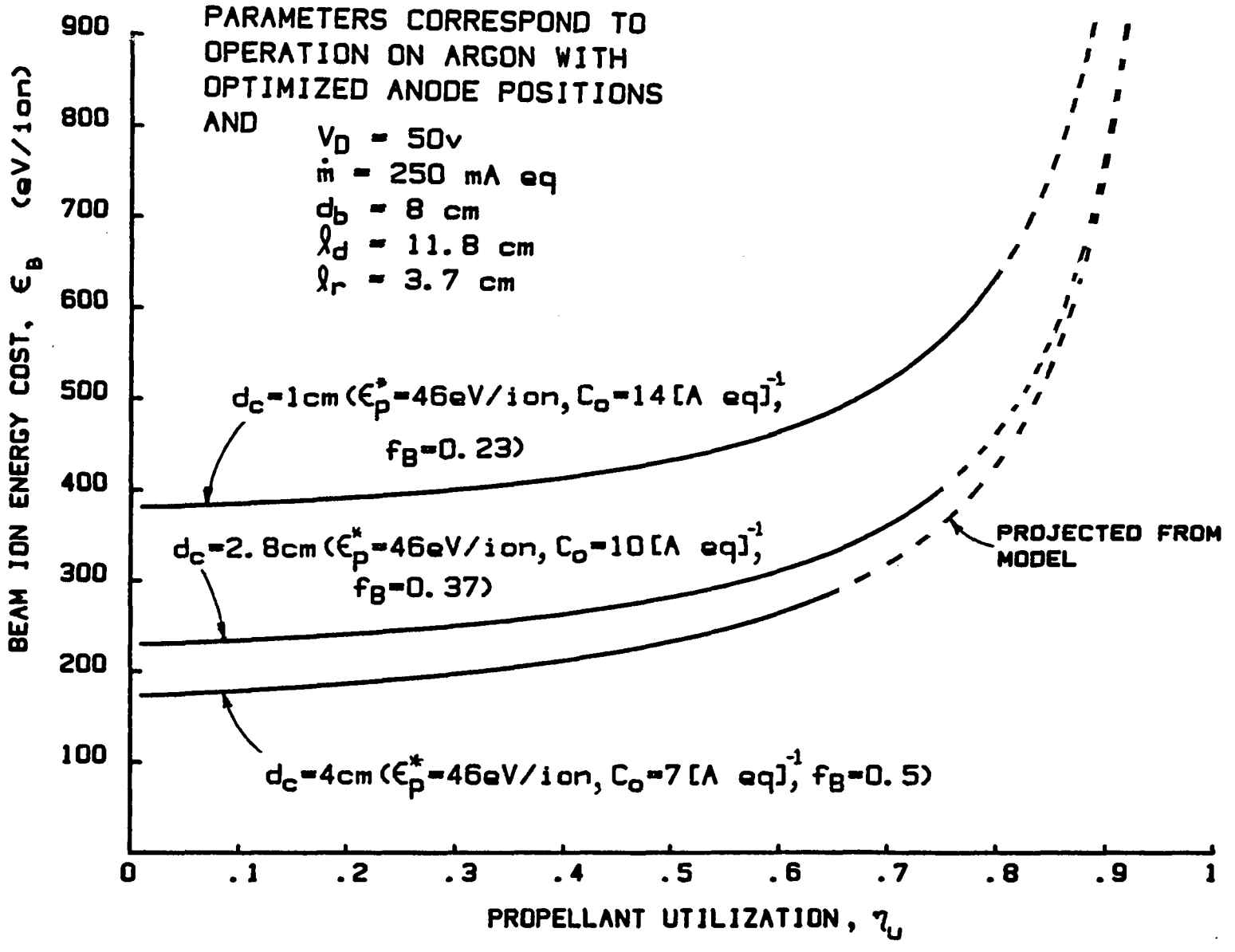

Fig. 10 Effect of Cathode Diameter on Thruster Performance

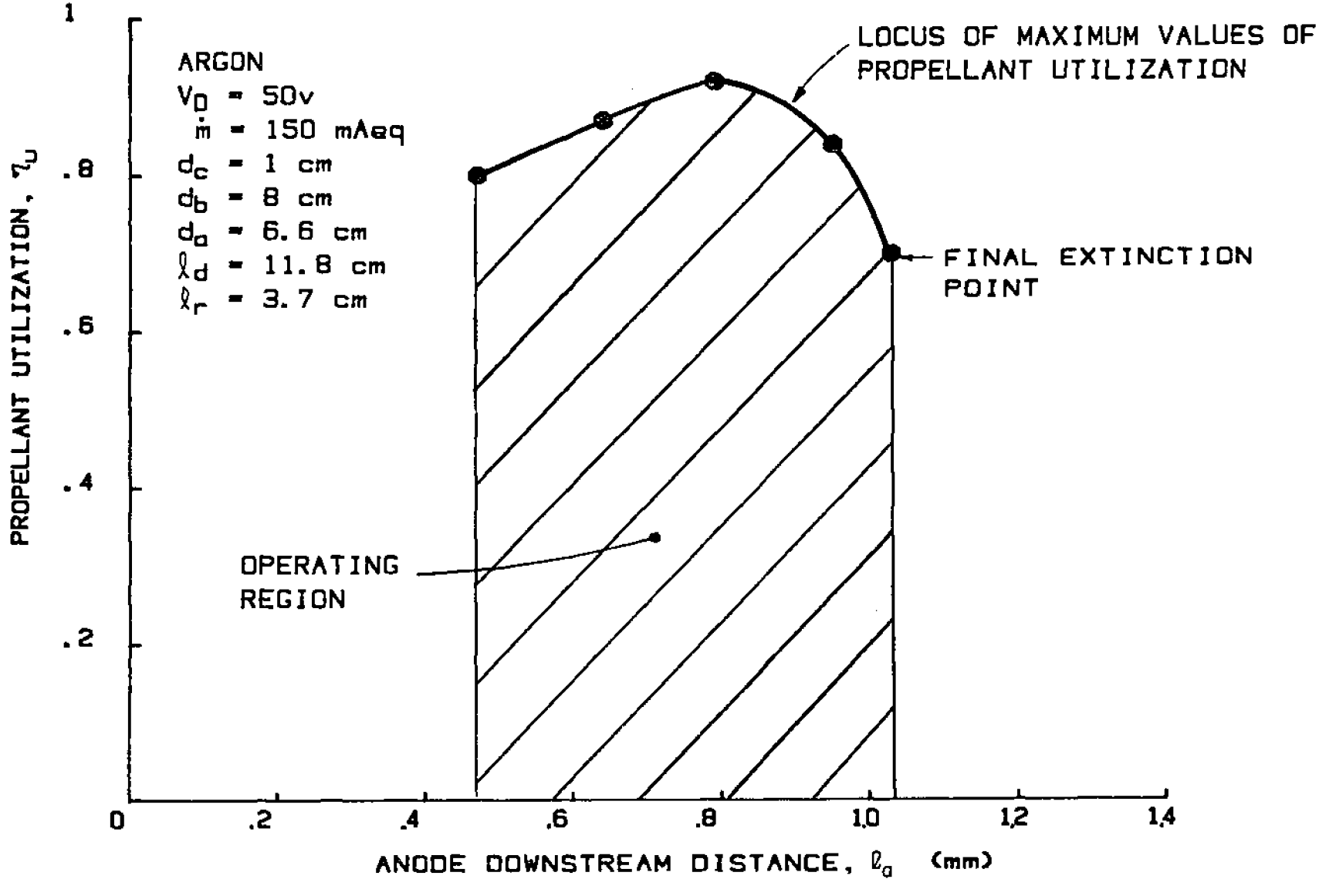

Fig. 11 Typical Effect of Anode Position on Propellant Utilization Range

of the propellant utilization, η_u against the anode downstream distance ℓ_a measured at the particular condition defined in the legend. The figure shows that operation near the final extinction point, where the plasma ion energy costs are lowest, limits the maximum propellant utilizatiion to approximately 70%, while operation with the anode loop positioned 2 mm further upstream, where the plasma ion energy costs are only slightly higher, makes it possible to achieve propellant utilizations greater than 90% before discharge extinction occurs. This observation suggests the optimum anode location for a given discharge chamber will involve a compromise between the maximum propellant utilization and the minimum plasma ion energy cost.

The operating range of the thruster seems to be limited at the left hand boundary of the cross-hatched region of Fig. 11 by excessive primary electron losses to the anode (i.e. many primary electrons go directly to the anode without having Maxwellian electron producing collisions). It is postulated that such losses reduce the electron density to the point where the required total anode current (i.e. that due to both primary and Maxwellian electrons) cannot be sustained at the prevailing discharge voltage. On the right hand boundary the thruster operation seems to be limited because the conductivity of the plasma between the virtual anode and cathode field liner surfaces becomes too low and the demanded discharge current cannot be conducted with the available potential difference. It should be noted that the data of Fig. 11 were obtained at a 150 mA eq. flow rate and that the range of anode downstream distances and propellant utilizations over which operation can be sustained increases with flow rate.

The cathode diameter was also found to affect the ion beam profile of this 8 cm dia ring cusp thruster. Beam profile data measured at a 64 mA beam current for 4 different cathodes with diameters varying from 1 cm to 6 cm are plotted in

Fig. 12. Each of these curves integrate to yield the measured beam current to within several percent. The flatness parameter corresponding to each curve in Fig. 12 is plotted against the cathode diameter in Fig. 13. This figure shows that increasing the diameter from 1 cm to 4 cm result in a modest improvement in the flatness parameter, while the change in d_c from 4 cm to 6 cm results in a more substantial improvement. Since a flatter beam profile must be induced by a flatter plasma density profile in the discharge chamber[9,10] increasing the cathode diameter must improve the discharge plasma uniformity at the grids.

Effect of Discharge Chamber Length

Changing the locations of the virtual cathode and virtual anode magnetic field lines by changing the anode and cathode positions have been shown to affect the overall performance of an 8 cm dia. ring cusp thruster substantially. Changing the discharge chamber length, however, had no effect on the plasma ion energy cost and only a minor effect on the fraction of ions extracted into the beam. The discharge chamber performance plot of Fig. 14 illustrates this insensitivity of the performance data to changes in the discharge chamber length over the range of values from 5.3 to 11.8 cm. For each chamber length, the anode loop location was optimized as described earlier, and although the optimum anode position for each chamber length was different, the plasma ion energy cost data at a given neutral density remained unchanged. It should be noted that the relatively high value of the primary electron utilization factor $C_o \simeq 17$ Aeq^{-1} is due primarily to the masked-down grid (d_b = 4 cm) used in this particular test, and that an even higher value would be expected based on the data of Fig. 4 and Eq. 4. This equation suggests halving the grid area would quadruple C_o which would imply a C_o of $\sim$48 for the data of Fig. 14. The reason why the C_o for Fig. 4 is not this large is not clear, but it is believed to be related to

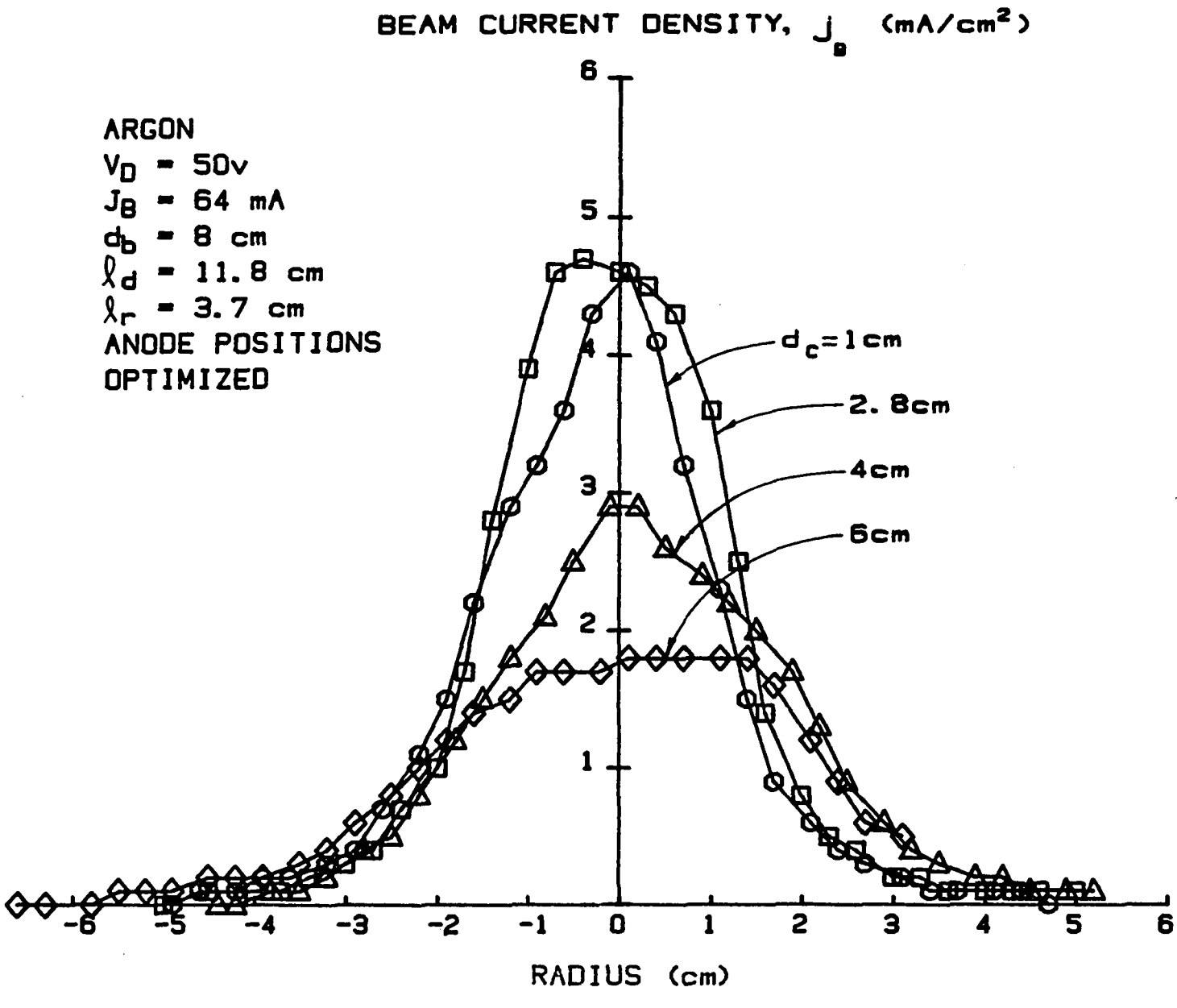

Fig. 12 Effect of Cathode Diameter on Ion Beam Profile

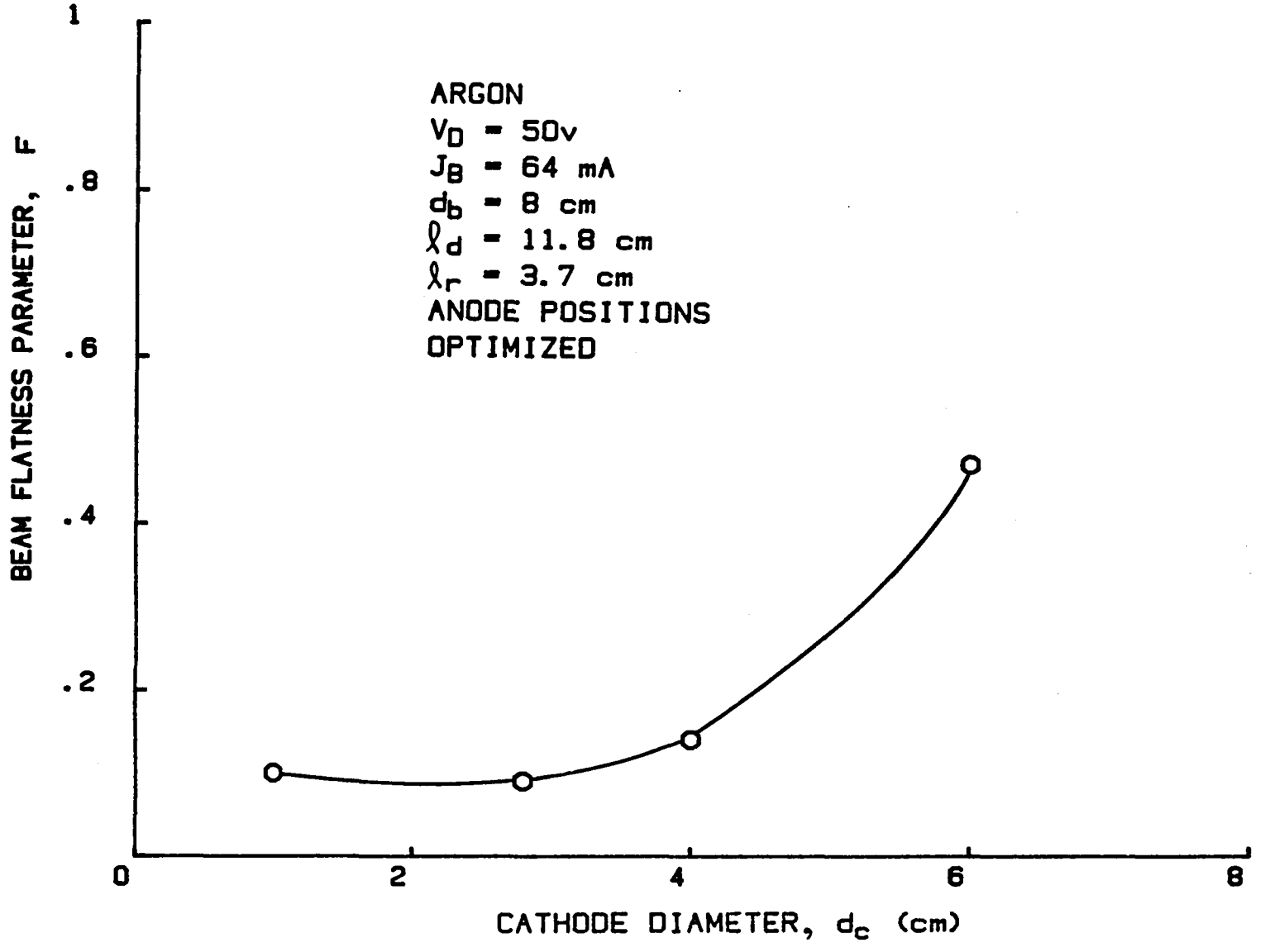

Fig. 13 Effect of Cathode Diameter on Ion Beam Flatness Parameter

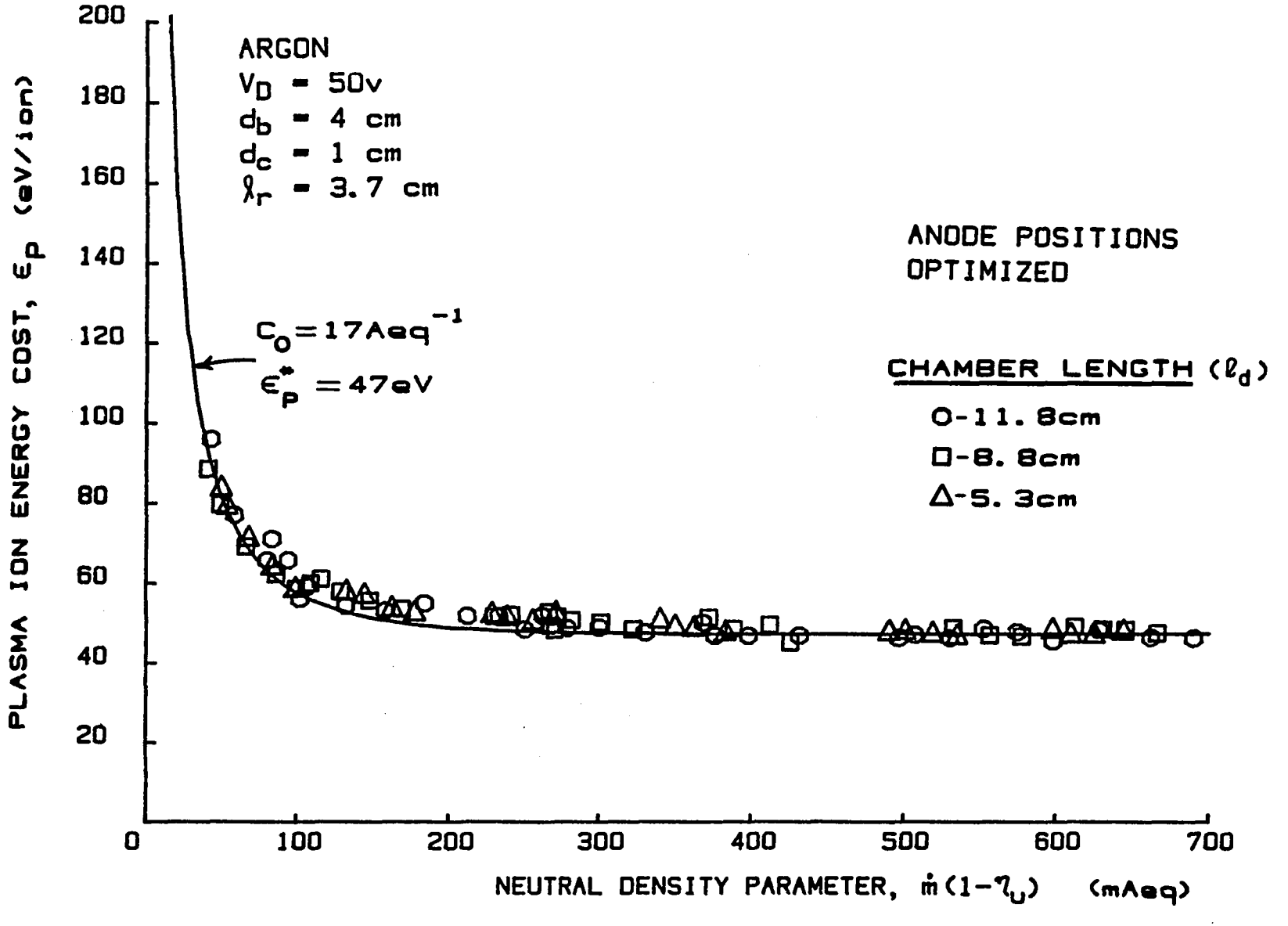

Fig. 14 Effect of Discharge Chamber Length on Plasma Ion Energy Cost Curve - Anode Axial Position Optimized

the small thruster size and the plasma non-uniformity that exists in such a thruster. In a larger, 15 cm dia. thruster Brophy[2] did observe the changes in C_o with beam diameter that are predicted by Eq. 4.

While shortening the discharge chamber length does not change the plasma ion energy cost curves, it does increase the extracted ion fraction. This improvement in f_B, which may have been caused by the altered magnetic field shape upstream of the magnetic ring cusp and/or the reduction in the total area to which ions in the discharge plasma could be lost, is shown in Fig. 15. It should be noted that, while the data of Fig. 15 were obtained at a neutral density parameter of 150 mA eq., the extracted ion fraction is independent of neutral density[2] so these data may be taken as typical. In fact it was observed in collecting the data for Figs. 14 and 15 that the extracted ion fraction varied less than 2% as the neutral density parameter was varied over the full range investigated at any discharge chamber length. The increase in the extracted ion fraction f_B from 0.2 to 0.3 caused by reducing the discharge chamber length from $\sim$11.8 cm to 5.3 cm are predicted to change the performance curves of the thruster defined in the legends of Fig. 14 and 15 in the manner suggested in Fig. 16. These curves show the pronounced effect of extracted ion fraction on performance as embodied in Eqs. 3 and 5.

Overall Performance Optimization

In order to optimize the overall performance of the 8 cm dia. ring cusp thruster studied here, it has been shown that certain geometrical relationships should be satisfied. These relationships, which are admittedly incomplete at this time, should eventually lead to a theoretical discharge chamber model that would enable a designer to specify the optimum geometry of a thruster without resorting to experimental optimization procedures. In conducting the

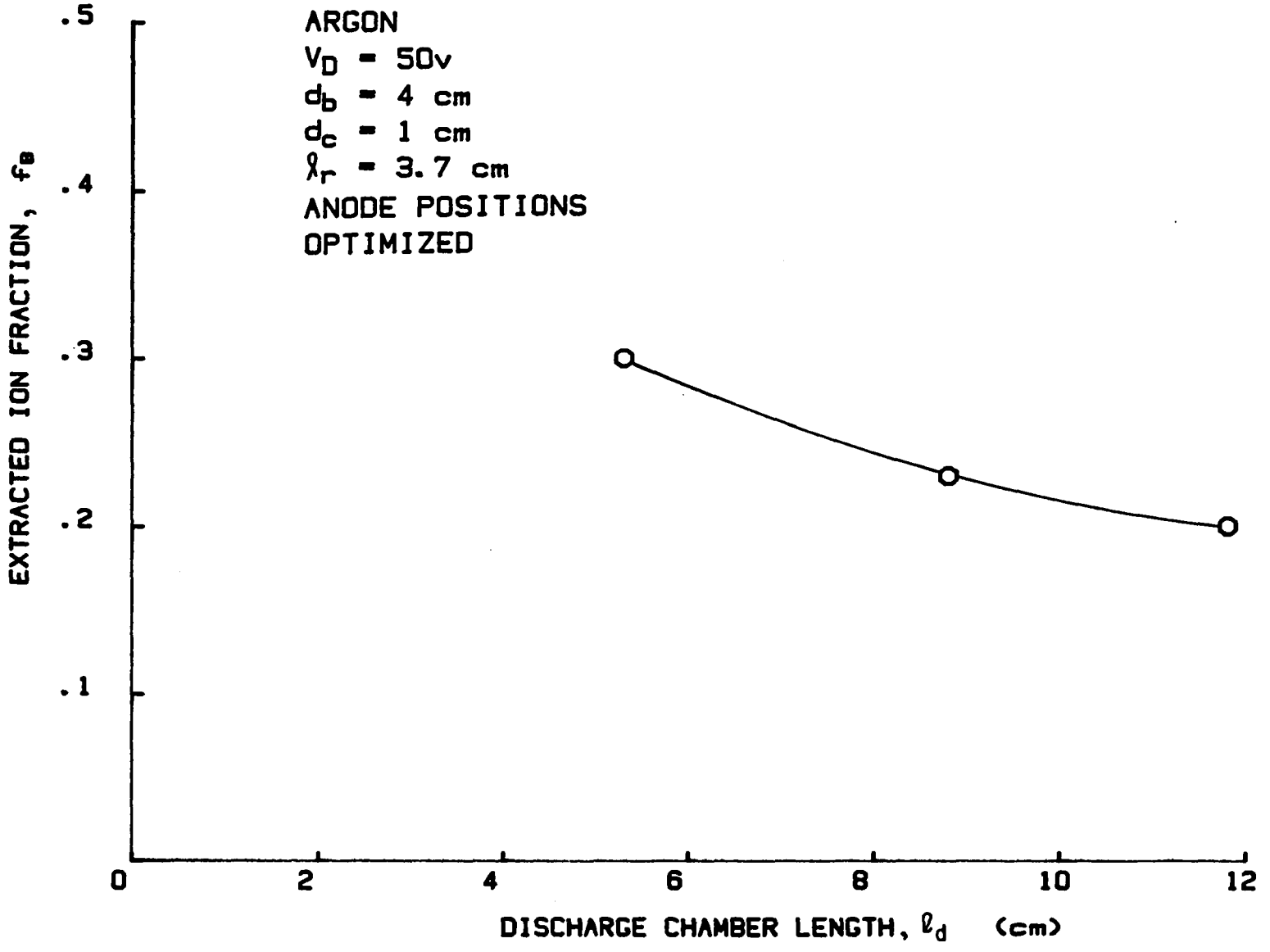

Fig. 15 Effect of Discharge Chamber Length on Extracted Ion Fraction

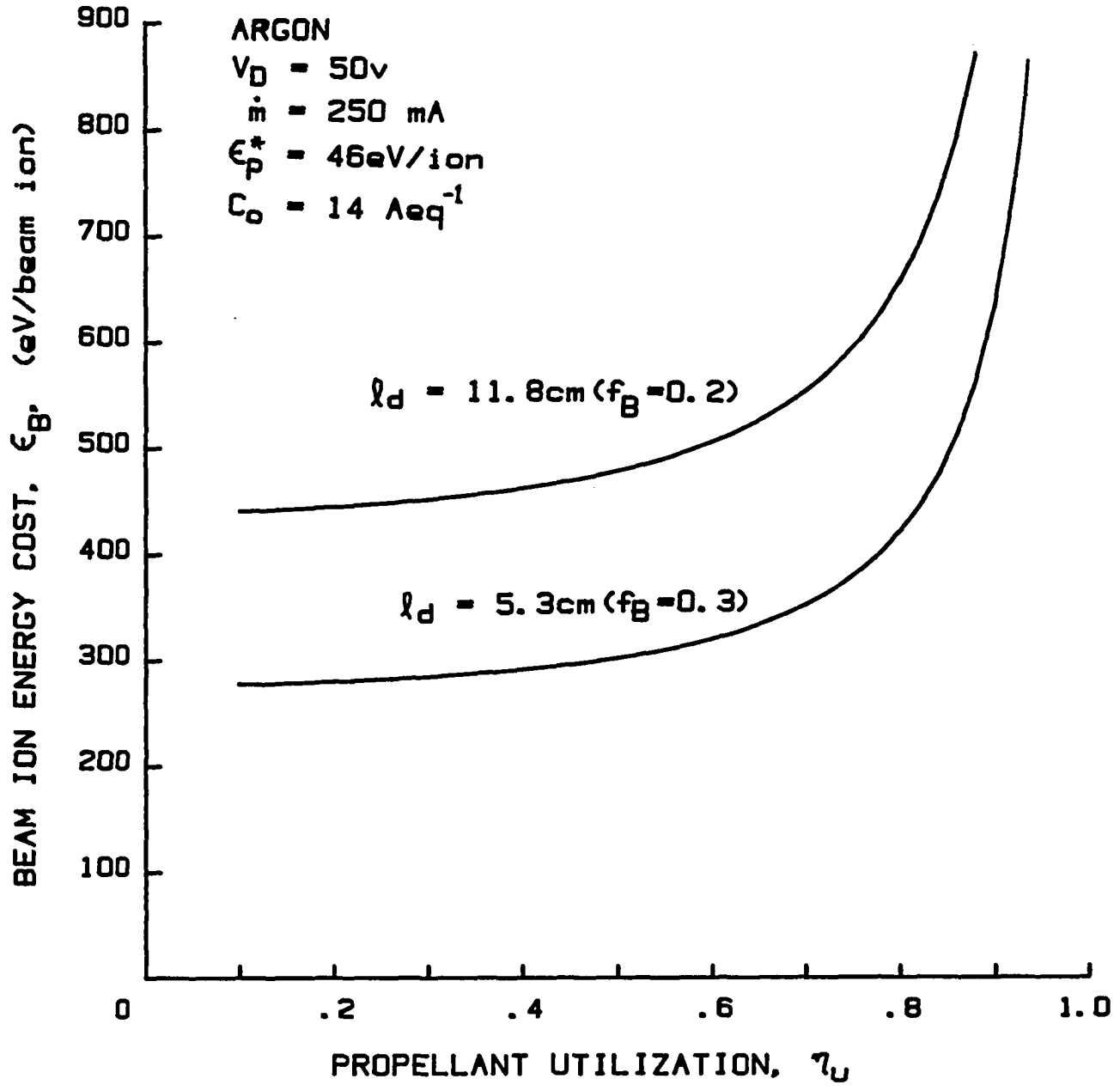

Fig. 16 Effect of Discharge Chamber Length on Performance

experiments described herein the relationships have been investigated by varying such parameters as cathode diameter, anode position and discharge chamber length, but variations in these parameters are viewed most logically in terms of the critical magnetic field lines that they define. If one initiates the logic path at the grids where the beam diameter is defined rather than with an arbitrarily positioned cathode where the experimental investigation began, the logical sequence of guidelines is the following one.

- The anode should be positioned in the magnetic field so the virtual anode field line intersects the outermost ring of holes in the screen grid. This condition helps to assure a maximum extracted ion fraction and a flat ion beam profile.

- The filament cathode diameter (d_c) should be selected so the associated virtual cathode field line is separated from the virtual anode field line by an amount that will assure this latter field line behaves as the optimum virtual anode that yields low plasma ion energy costs. While the criterion that determines the separation between the virtual anode and cathode field lines has not been quantified it is believed to be related to the line integral of the magnetic field intensity along a line orthogonal to the field lines.[6] It is known that the plasma ion energy decreases as the separation distance between these field lines is increased up to the point where the discharge extinguishes. It is believed that the plasma ion energy cost decreases as the separation between the virtual anode and cathode field lines is increased because of improved primary electron containment.

Two additional discharge chamber parameters that were varied in these tests and had less significant effects on performance were the following:

• Reducing the discharge chamber length (ℓ_d) from 1.5 times its diameter to 0.7 times its diameter induced a monotonic increase in the extracted ion fraction. Mechanical interference problems prevented further reductions in length so it could not be determined if this trend continued to shorter chamber lengths.

• Increasing the distance between the ring cusp and the screen grid (ℓ_r) from 3.7 cm to 4.5 cm induced an increase in the extracted ion fraction. Increasing this distance would be expected to change the magnetic field shape and intensity in the vicinity of the grids. It is believed that increasing this distance tends to reduce the magnetic field strength near the grids and thereby improve the uniformity of both the magnetic field and the plasma density at the grids. It should be noted at this point that the problems of magnetic field shaping and radial plasma uniformity near the grids are much more severe in the 8 cm dia. ion source used in this study than they would be in larger ones (e.g. 15 or 30 cm dia. thrusters).

In order to test the proceeding design guidelines they were applied to define a discharge chamber geometry for the 8 cm dia. ring cusp thruster that would be expected to yield good performance curves. A typical example of a resulting performance curve (measured at a flow rate of 165 mA eq.) is shown in Fig. 17. This performance curve is considered to be exceptionally good for a small, 8 cm dia. ion source being operated on argon.

Finally it is noted that while the anode diameter could be selected to have any value that would enable it to be located on the virtual anode field line, it is probably preferable for it to have a value equal to the diameter of the virtual anode field line in the region where it is parallel to the thruster axis. At this condition the performance and discharge stability were observed to be

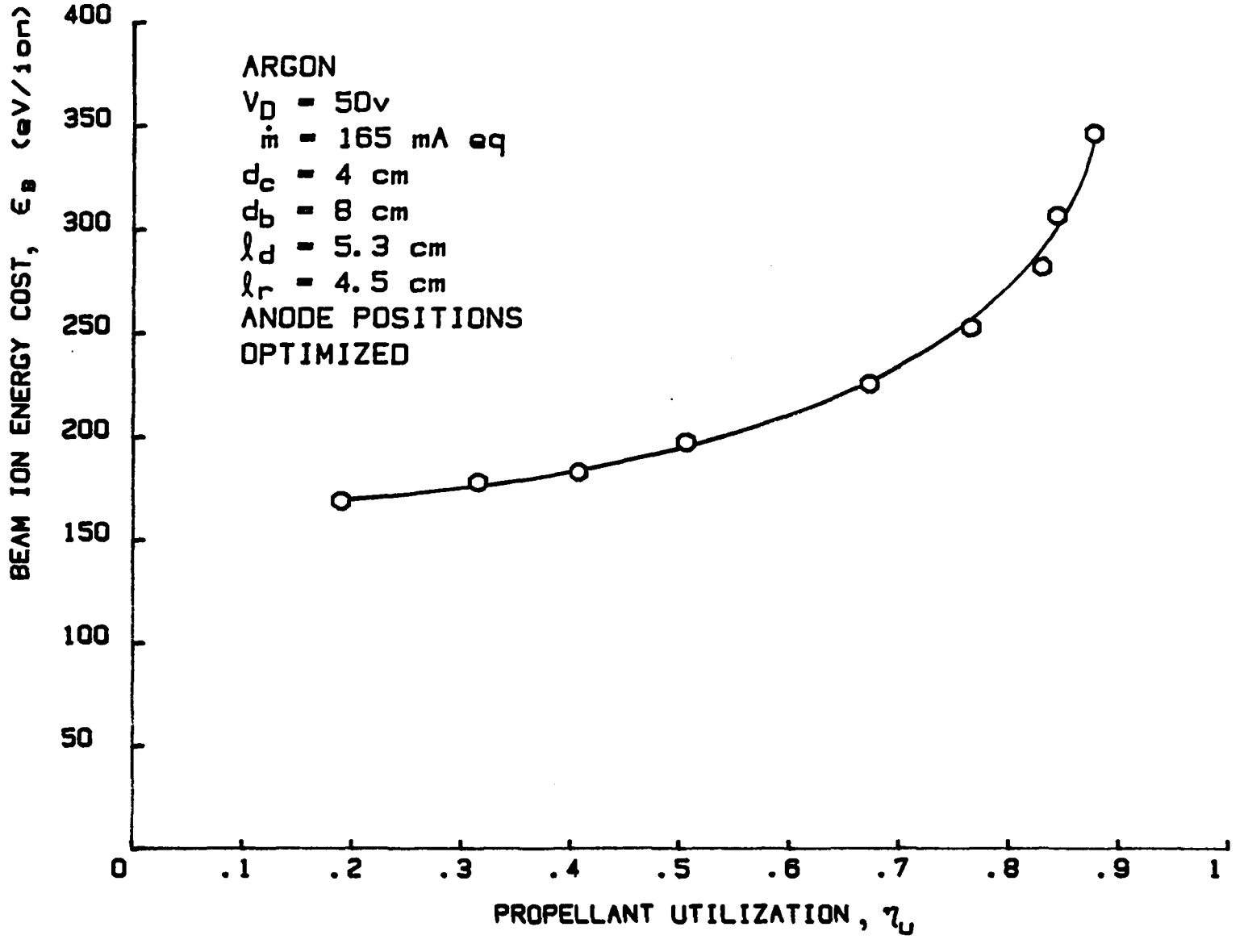

Fig. 17 Optimized Performance Curve for 8 cm dia. Ring Cusp Thruster

relatively insensitive to the axial location of the anode.

Conclusions

The efficiency of an 8 cm dia. chamber having one centerline and one ring magnetic field cusp is improved substantially by moving the electron collection surface (anode) from the magnetic cusp surface to a location downstream of the ring cusp. In its preferred position the anode establishes contact with a circle on the surface of revolution of the optimum virtual anode magnetic field line. With the anode at this position the discharge is close to the point of extinction but plasma ion energy costs are minimized because primary electron losses to the anode are low. No change in the fraction of ions extracted into the beam is observed when the anode is moved from the magnetic cusp surface to the optimum virtual anode field line. These observations lead one to conclude that Sovey[3] could have achieved even better performance in his 30 cm dia. ring cusp discharge chamber if he had located his anodes away from the magnet surfaces rather than on them.

Changing the diameter of a circular cathode surface supplying primary electrons to the discharge also influences discharge chamber performance but it does so primarily because it influences the position of the optimum virtual anode. When the cathode is positioned so the optimum virtual anode field lines intersect the outermost ring of holes in the screen grid the preferred condition of a high extracted ion fraction will be achieved. The extracted ion fraction can also be increased by decreasing the discharge chamber length. With the anode located so it is in contact with a circle on the surface of revolution of the optimum virtual anode field line, no change in the plasma ion energy cost is observed as the chamber length is changed. A slight increase in the plasma ion energy costs accompanies increases in cathode diameter. The best overall

operating condition is observed when the cathode and anode positions and the magnetic field configuration are selected so the discharge operates stably near the discharge extinction point and the optimum virtual anode field line intersects the outer ring of holes in the grid system.

ELECTRODYNAMIC TETHER PLASMA CONTACTOR RESEARCH

Thomas Laupa

Hollow cathode plasma sources have been proposed as devices that could establish a low impedance connection between a space vehicle and the space plasma surrounding it.[11] Preliminary work described here has been conducted to determine how cathode operating parameters affect this connection, and how the plasma surrounding the cathode behaves as substantial current densities, similar to those that are expected in electrodynamic tether applications, are forced through the connection.

An electrodynamic tethered satellite system (TSS) includes two space vehicles connected by a long, conductive tether. When it is oriented properly, the tether cuts through the earth's magnetic field lines as the vehicle moves in its orbit. As a result, a voltage difference is induced between the two ends of the tether. In order to take advantage of this voltage difference for direct current power generation purposes, a return path for current that could flow from one end of this tether to the other through an electrical load must be provided. The schematic of Fig. 18 shows a scheme proposed to provide this return path.[12] As this figure suggests the voltage drops around the circuit are due to the tether, the load, the space plasma and the two plasma contactors (one collecting electrons and one emitting them). For efficient operation the load impedance should be large compared to the sum of the impedances of the other elements of the circuit. The tether impedance can be controlled readily by adjusting the tether conductor diameter. Both theoretical and experimental data have suggested that the conductivity of the ambient space plasma is sufficiently high so that an excessively high voltage drop would not be expected to develop across it when the system is operated at optimal current levels. On the other

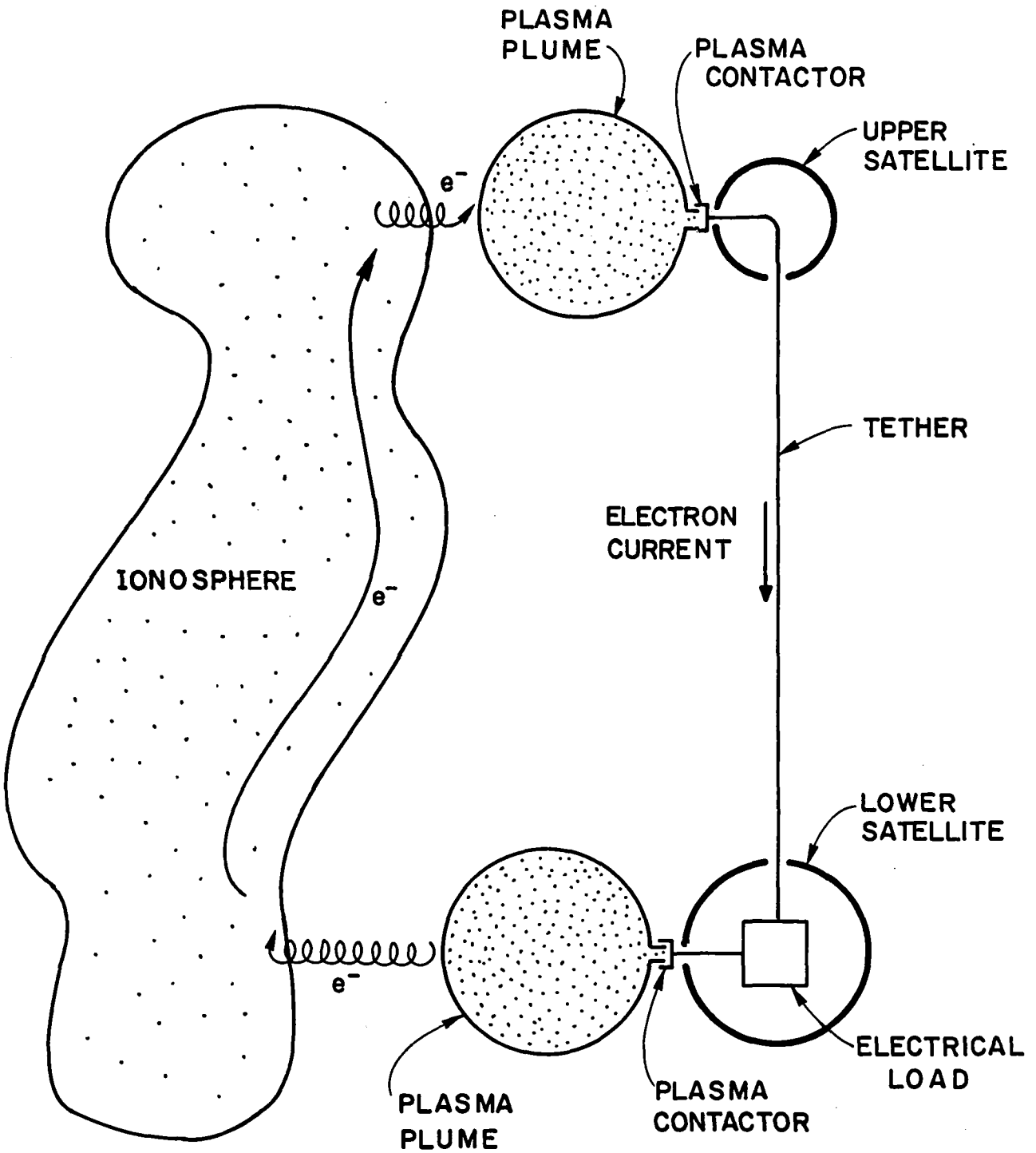

Fig. 18 Electrodynamic Tether Circuit

hand, the plasma contactors could be a source of substantial impedance if they cannot be made to operate properly. As the sketch of Fig. 18 suggests these plasma contactors, when operating properly, would generate a high density plasma plume with a sufficiently large surface area so that it could conduct the tether current at current densities typical of the ambient space plasma. Further, the requirement for low plasma contactor impedances necessitates current conduction by electrons as the figure suggests and a suitable plasma contactor must therefore be able to operate in the two modes shown (electron emission and electron collection).

The objective of the work described here has been to understand the plasma contacting process and to evaluate the suitability of the hollow cathode[13] as a plasma contactor in general. A further objective has been to examine the suitability of a hollow cathode for the TSS-1 mission.[14]

Apparatus

The nature of the coupling between the plasma from a hollow cathode and a low density plasma representative of a space plasma has been studied in a 1.2 m dia. by 5.3 m long tank shown schematically in Fig. 19. A 7 mm diameter cathode with a 0.7 mm dia. orifice was mounted at one end of the chamber. The cathode acts as the contactor and also provides the background 'space plasma' through which the currents are conducted. Downstream of the cathode, a tungsten filament is mounted on the support rod shown in Fig. 19. This filament can be moved axially over a distance from zero to 1.0 m downstream of the cathode and radially from the cathode centerline to a radius of 25 cm. In most of the testing the filament was kept on the cathode centerline where it was believed the perturbing effect of the tank walls would be minimized. When heated to thermionic

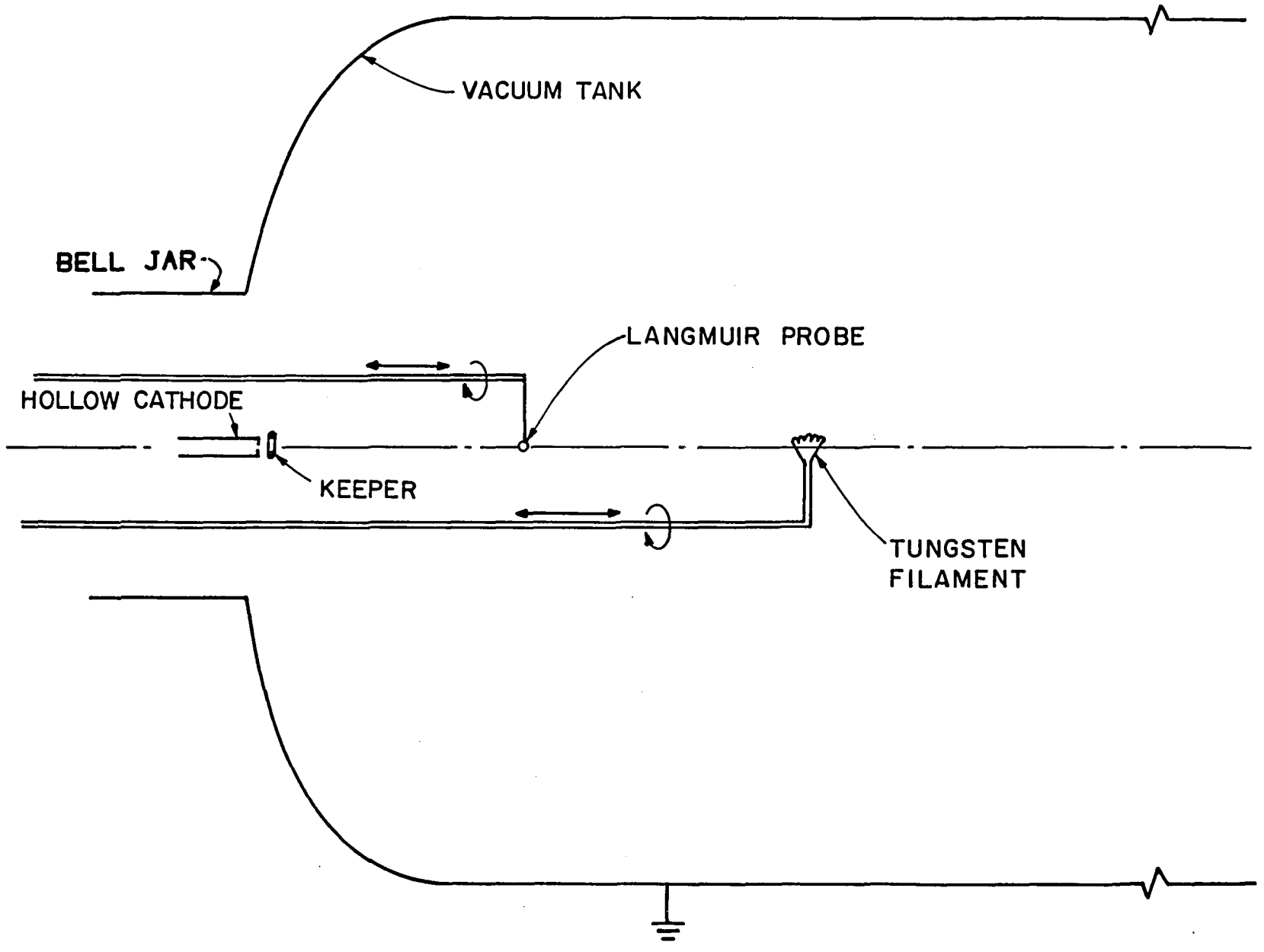

Fig. 19 Test Configuration for Plasma Contactor Research

emission temperatures, the filament provides low temperature electrons that are intended to model the low energy electrons that would be collected from the space plasma when the cathode was being operated in the electron collection mode. When the hollow cathode is being operated in the other (electron emission) mode the filament is not needed. In this case the cathode is simply biased negative of the tank walls so that electrons generated in the hollow cathode discharge are repelled from the hollow cathode and drawn to the walls.

Langmuir and emissive probes, which can be used to measure plasma properties, are mounted on a second support rod shown schematically in Fig. 19. These probes can also be moved axially and radially from the cathode centerline to measure plasma properties in the region downstream of the cathode. Details of the Langmuir probe and its associated circuitry as well as the analysis technique used to interpret probe traces obtained in the study are included in Appendix A of this report. The emissive probe was a 2 mm long piece of 0.076 mm diameter tungsten wire that was heated to thermionic temperatures using a battery power supply. The filament and the batteries connected to it were isolated electrically so they tended to float near the plasma potential at the probe location. This potential was measured using a high impedance (10 Megohm) voltmeter. Except for the fact that a voltmeter was used here in place of an electrometer, the emissive probe apparatus used was the same as that described in Ref. 15.

The electrical schematic of the apparatus used in initial tests is shown in Fig. 20a. The alternating current heater and filament supplies were used respectively to heat the hollow cathode and tungsten filament. The keeper supply provided the discharge power needed to operate the hollow cathode. The emission supply biased the filament with respect to the cathode to induce elec-

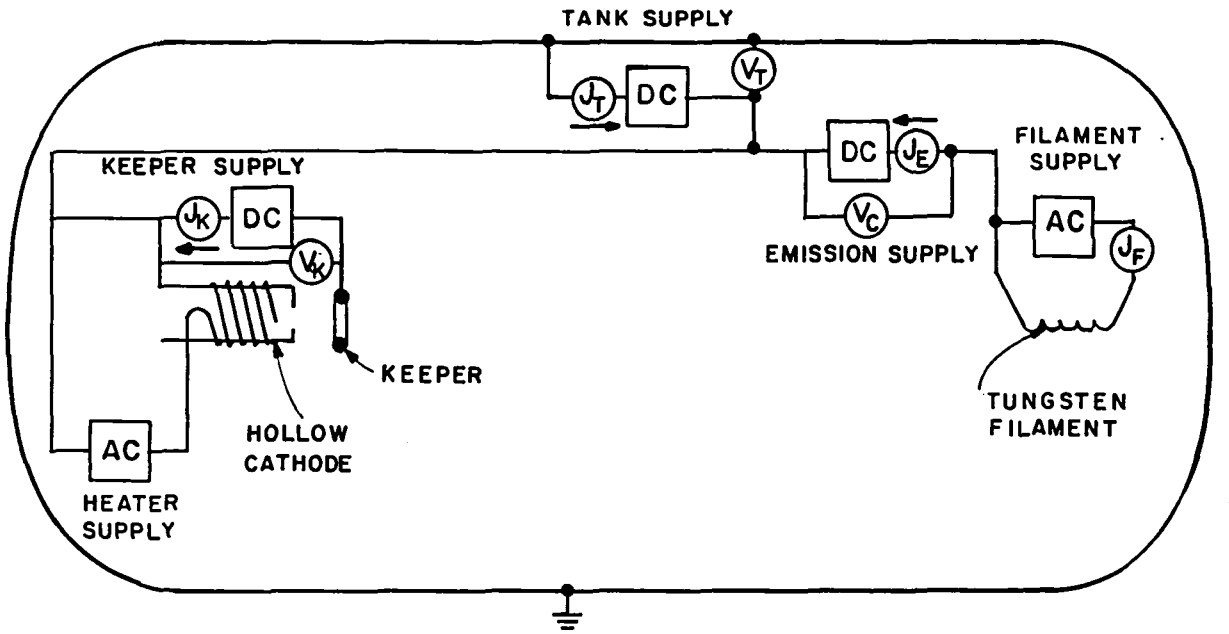

a. INITIAL CONFIGURATION

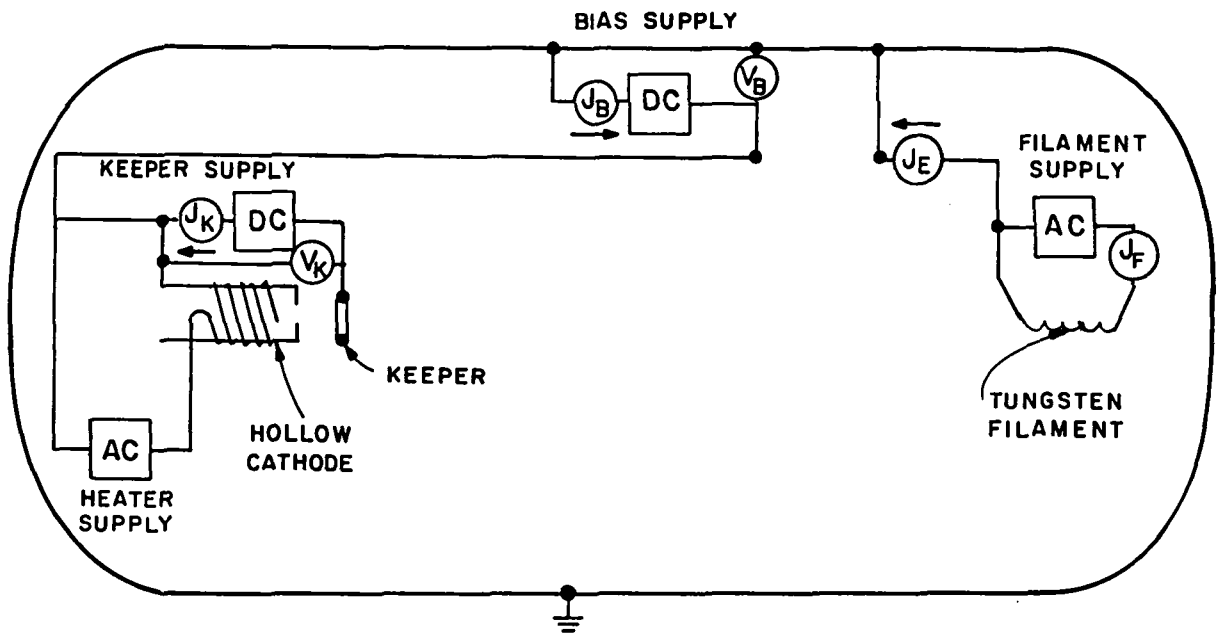

b. MODIFIED CONFIGURATION

Fig. 20 Electrical Schematic for Plasma Contactor Experiment

tron collection by the hollow cathode. In these initial tests the tank supply was used to bias the hollow cathode/filament system relative to the tank so the perturbing effect of the tank could be minimized. Subsequently, it was determined that the perturbing effects of the tank were small when the electron emitting filament and the tank were kept at the same potential so they were connected electrically in the modified electrical configuration of Fig. 20b. In this configuration the bias supply was used to adjust the hollow cathode potential either positive or negative of the tank and filament, so it would either collect or emit electrons. In these tests where the hollow cathode's electron collection and emission characteristics were measured the tank and filament were both at a potential that was representative of the space plasma. It should be noted that the tungsten filament heater supply could be turned off so the filament would not emit electrons, the hollow cathode could then be biased positive of the tank and the ion emission from the hollow cathode discharge to the tank could be measured on the bias supply ammeter (J_B). Throughout this report electron currents will be designated positive when they flow in the direction indicated by the arrows above the ammeters in Fig. 20.

One can argue that the apparatus of Fig. 19 does not model the plasma contactor collecting electrons in space adequately because it supplies electrons from a small region rather than from a surface that surrounds the cathode. In order to explore the importance of this effect a second set of experiments was conducted using two filaments to supply the electrons rather than one. The test apparatus shown in Fig. 21 indicates how the apparatus was arranged to facilitate axial and radial movement of the filaments. The electrical arrangement of Fig. 20b was altered for these tests by adding a second filament supply and ammeter so each filament could be both operated and monitored independently.

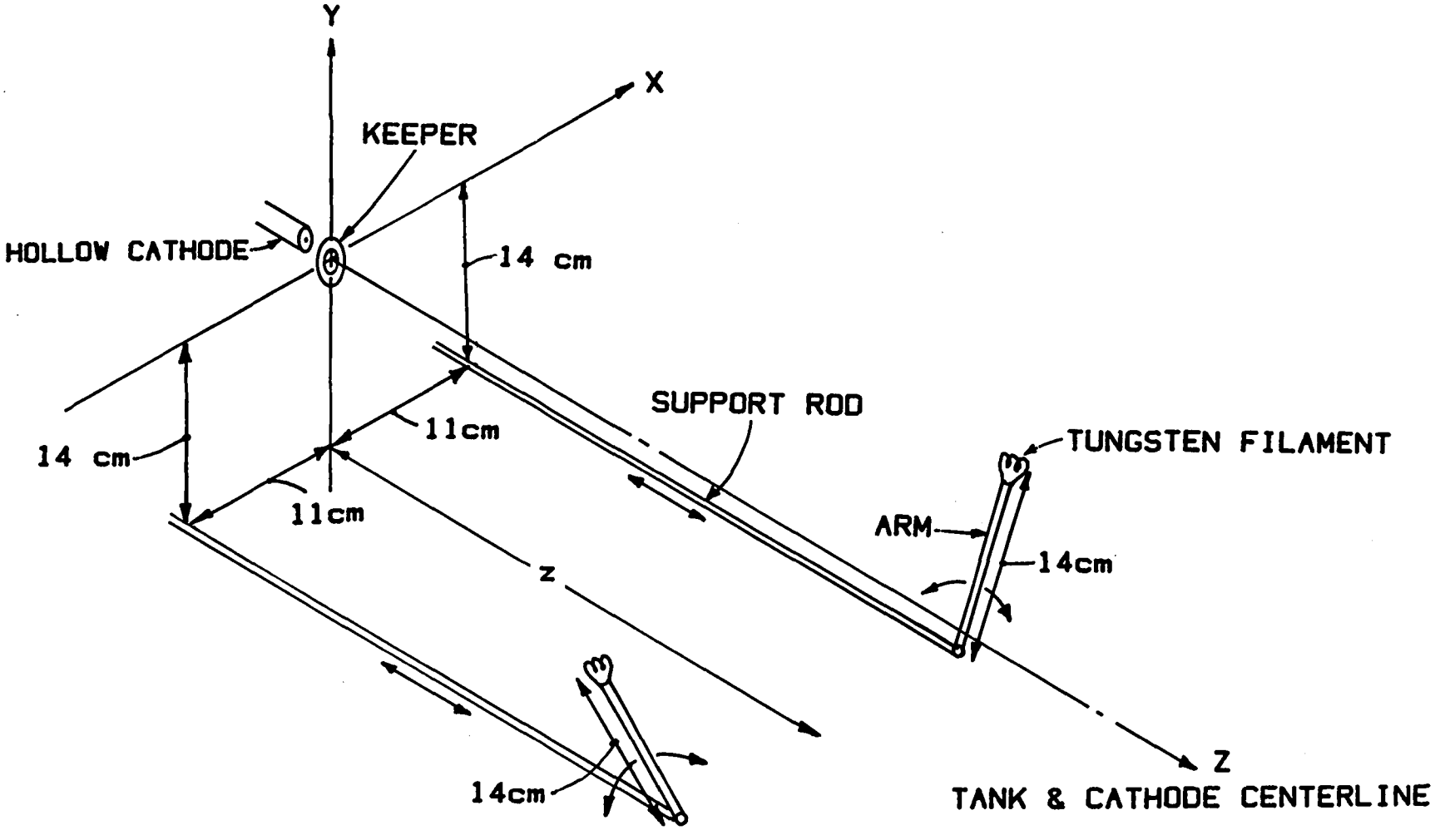

Fig. 21 Dual Filament Test Configuration

Procedure

In order to conduct a test the filament was positioned at the desired location and hollow cathode operation was initiated at a prescribed xenon flow rate and keeper current. After the discharge had stabilized the hollow cathode was biased sufficiently positive of the tank using the tank supply (Fig. 20a) or bias supply (Fig. 20b) so the total ion current emitted from the hollow cathode discharge would be drawn to the tank. This current was measured using the tank or bias current meter (J_T or J_B). Next the hollow cathode was biased negative of the tank and the electron current drawn to the tank (J_T or J_B) was measured as a function of tank-to-cathode potential difference (V_T or V_B). The filament was then heated*, the hollow cathode was biased positive of the tank and filament and the sum of the electron current collected and ion current emitted by the hollow cathode ($J_T + J_E$ for Fig. 20a or J_B for Fig. 20b) was measured as a function of bias voltage. The electron emission current (J_E) was also measured to determine the current supplied by the filament in the modified configuration (Fig. 20b). After collection of these data the cathode keeper current or the filament position could be varied and the procedure could be repeated. For the dual filament tests the procedure was similar except for the fact that emission currents from each of the filaments were measured.

In the process of conducting these tests the Langmuir and emissive probes were used to measure plasma properties in the region between the hollow cathode

---

* In preliminary tests a filament current (J_F) of 7 A flowing through the 0.25 mm dia. tungsten filament was found to be sufficient to assure filament electron emission in excess of that which could be drawn to the cathode under the most demanding conditions, so the filament current was maintained at 7 A. In other words this current assures electron emission from the filament is limited by the sheath at the filament and not by thermionic emission considerations.

and the filament. Typically this was done at several tank/filament bias conditions. In an early test the plasma downstream of a hollow cathode operating at 0.3A keeper current was Langmuir probed. It was determined that the plasma density dropped to a value near $10^6 cm^{-3}$ about 0.9m downstream of the cathode on its centerline. Many tests were conducted with the filament at this location because this density is close to the value observed in space at shuttle orbit altitudes.

Results

During the initial series of test conducted with one filament the effect of biasing the hot filament negative of the hollow cathode to effect electron collection by the hollow cathode and then biasing the tank to minimize its perturbing effect was examined. This was accomplished using the electrical configuration of Fig. 20a. In one test the electron collection current drawn by the hollow cathode was measured as a function of hollow cathode/filament bias voltage with the tank voltage adjusted to assure zero net current to the tank ($J_T = 0$). In a second test the same measurements were made while adjusting the tank potential to maintain it the same as the filament potential. These curves were essentially identical so it was decided to connect one side of the filament to the tank and eliminate the emission power supply shown in Fig. 20a thereby simplifying the test procedure and data collection. Unless noted otherwise the results that follow will have been obtained using this test configuration (i.e. the one of Fig. 20b).

When an operating hollow cathode is biased relative to the tank and a non-emitting (cold) filament, it produces electrons and ions at rates that cause it to exhibit a voltage/current characteristic curve like the one represented by the circular symbols and solid line in Fig. 22. This curve shows that biasing

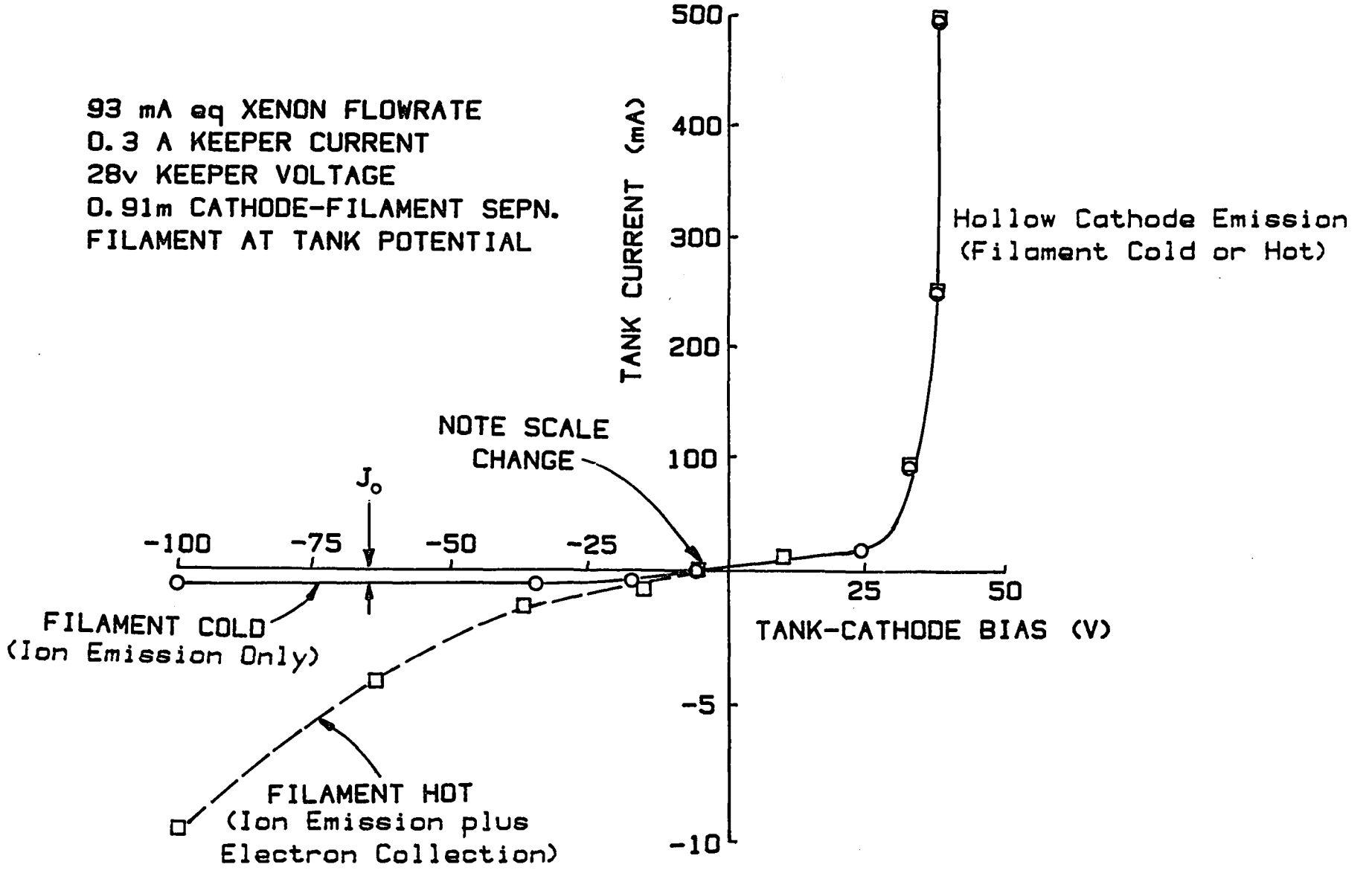

Fig. 22 Typical Hollow Cathode Characteristic

the hollow cathode negative of the tank (i.e.positive tank-cathode bias) causes an increasingly large electron current to be drawn from the hollow cathode to the tank/filament. As the cathode is biased sufficently negative so the tank/filament becomes more positive than the keeper (this occurs at 28 v for the data of Fig. 22) the electron current emitted by the hollow cathode is observed to rise rapidly. While the current is shown rising to 500 mA in Fig. 22 the cathode would actually emit electron currents greater than three amperes at essentially the same tank-to-cathode voltage difference. It is reasonable to assume that the observed rapid increase in electron current occurs as the tank potential rises above the keeper voltage because the plasma between the cathode and keeper would be expected to have a potential near keeper potential. While the electron emission capability of a hollow cathode is not unlimited, the results of Fig. 22 show it can emit substantial electron current at a modest bias potential and this demonstrates its effectiveness as an electron emitter. This electron emission capability of hollow cathodes has been demonstrated in space on numerous occasions, but it was probably shown most effectively on the SERT II Experiment.[16,17]

As the hollow cathode is biased positive of the tank and cold filament (i.e. in the third quadrant of Fig. 22) electrons from the hollow cathode plasma begin to be reflected from the tank and ions produced there begin to be collected by the tank. Currents flowing under this condition are considerably smaller than the electron currents emitted by a negatively biased cathode as a comparison of the scales above and below zero on the vertical axis of Fig. 22 suggest. When the cathode is 30 V or more positive of the tank (i.e. less than -30 v tank-cathode bias) essentially all electrons being produced by the hollow cathode are repelled and all of the ions being produced are collected by the tank. The ion current collected by the tank is observed to remain constant (saturated) at

J_o = 0.6 mA for the hollow cathode operating conditions of Fig. 22 as the tank-cathode bias was decreased further from -30 to -100.

When the test just described was repeated with the filament heated to thermionic emission temperatures the hollow cathode electron emission region of the curve (first quadrant) remained unchanged from that observed with the cold filament just as one would expect. When the cathode was biased positive so it would emit ions, however, the curve shape changed as electrons from the hot filament were drawn to the hollow cathode thus adding to the ion current being emitted by the hollow cathode. Still, the currents that flow when the filament is hot and the cathode is biased to collect electrons are small (<10 mA) compared to the currents in the first quadrant of Fig. 22 (>500 mA). The reason for this can be understood by considering the phenomena that might limit the electron current flowing from the filament to the hollow cathode. The filament emission could be limited by thermionic phenomena, but the filament was known to be sufficiently hot so that this was not limiting. The plasma between the filament and cathode could have been a poor conductor because electron motion was limited by either collisions or magnetic field effects. Calculations suggested, however, that the electron-atom momentum transfer mean free path was long (>25 m) compared to cathode-filament separation (0.9 m) and the magnetic field strength in the region was low (< 0.5 gauss). These numbers suggest that neither of these phenomena are limiting the current so it seems likely that one or more sheaths are developing between the filament and cathode to limit the electron current.

It should be mentioned that the hollow cathode could be biased 150 V positive relative to a heated filament when there was no hollow cathode discharge and any electron current that could be drawn from the filament was less than the ammeter threshold (i.e. <0.1 mA). This suggests that the cold ions produced in

the hollow cathode discharge are required to facilitate the flow of even minimal currents. When these ions are presented they make it possible for a plasma bridge to form between the filament and hollow cathode so that sheath impedances can be reduced to the point where measurable electron current conduction can occur.

A comparison of the magnitudes of the currents in the 1st quadrant of Fig. 22 (hollow cathode electron emission) and the 4th quadrant (hollow cathode electron collection) shows that the impedance associated with electron collection is by far the greater. As a result the remainder of this report will focus on the electron collection process.

Since double sheath theory has suggested that the magnitude of counterflowing ion and electron currents (J_i and J_e respectively) should be limited by the relationship[18]

$$\frac{J_e}{J_i} \leq C \sqrt{\frac{m_i}{m_e}} \tag{6}$$

where m_i and m_e are the ion and electron masses and C is a geometry dependent parameter, it is appropriate to examine the data in terms of this current ratio. If the electrons drawn from the filament to the hollow cathode do not have ionizing collions then the ion current drawn from the hollow cathode plasma would remain constant at J_o. It is argued that the ion saturation current (J_o) would under this condition represent the total production current and that this current would flow from the hollow cathode discharge to the filament or tank whenever the cathode was more than several volts positive of the filament/tank. Hence for the data of Fig. 22 the electron-to-ion current ratio flowing would

simply be the ratio of the total electron current collected from the hot filament to the ion saturation current (J_o) at a given bias condition. This ratio of total electron current to ion production current will be plotted against the keeper-to-tank voltage difference. The keeper-to-tank voltage difference has been chosen as the independent variable because the plasma in the immediate vicinity of the hollow cathode is generally at or near keeper potential. Thus, the keeper-to-tank voltage difference approximates the potential bias between the cathode plasma and the tank wall or filament that induces the ion and electron currents to flow. For the data of Fig. 22 the keeper-to-tank voltage difference (28 V minus the tank-cathode bias) is plotted against the electron-to-ion production current ratio in Fig. 23. This figure shows curves for three values of cathode to filament separation distance (0.3, 0.61, and 0.91 meters). Since the slopes of the curves in Fig. 23 increase with the voltage difference, either the presence of a space-charge-limited sheath or an increase in the ion production rate J_o with voltage difference is suggested. The fact that the curves are nearly coincident as the separation distance is changed suggests that any sheath that might be forming is doing so over a limited portion of the interelectrode region (eg. at the filament or at the hollow cathode).

To investigate the possible sheath formation suggested by the data of Fig. 23 further, Langmuir and emissive probe measurements were taken at several points between the hollow cathode and the filament at four tank/ filament-to-keeper bias conditions. The plasma potential profiles which were obtained from these probe measurements are shown in Fig. 24. All potentials shown are referenced to cathode potential and since plasma potential at the hollow cathode would be expected to be close to the 28 V keeper potential the driving potential differences would be the difference between the tank/filament potential and the keeper potential. Thus the curves of Fig. 24 correspond to cases where the

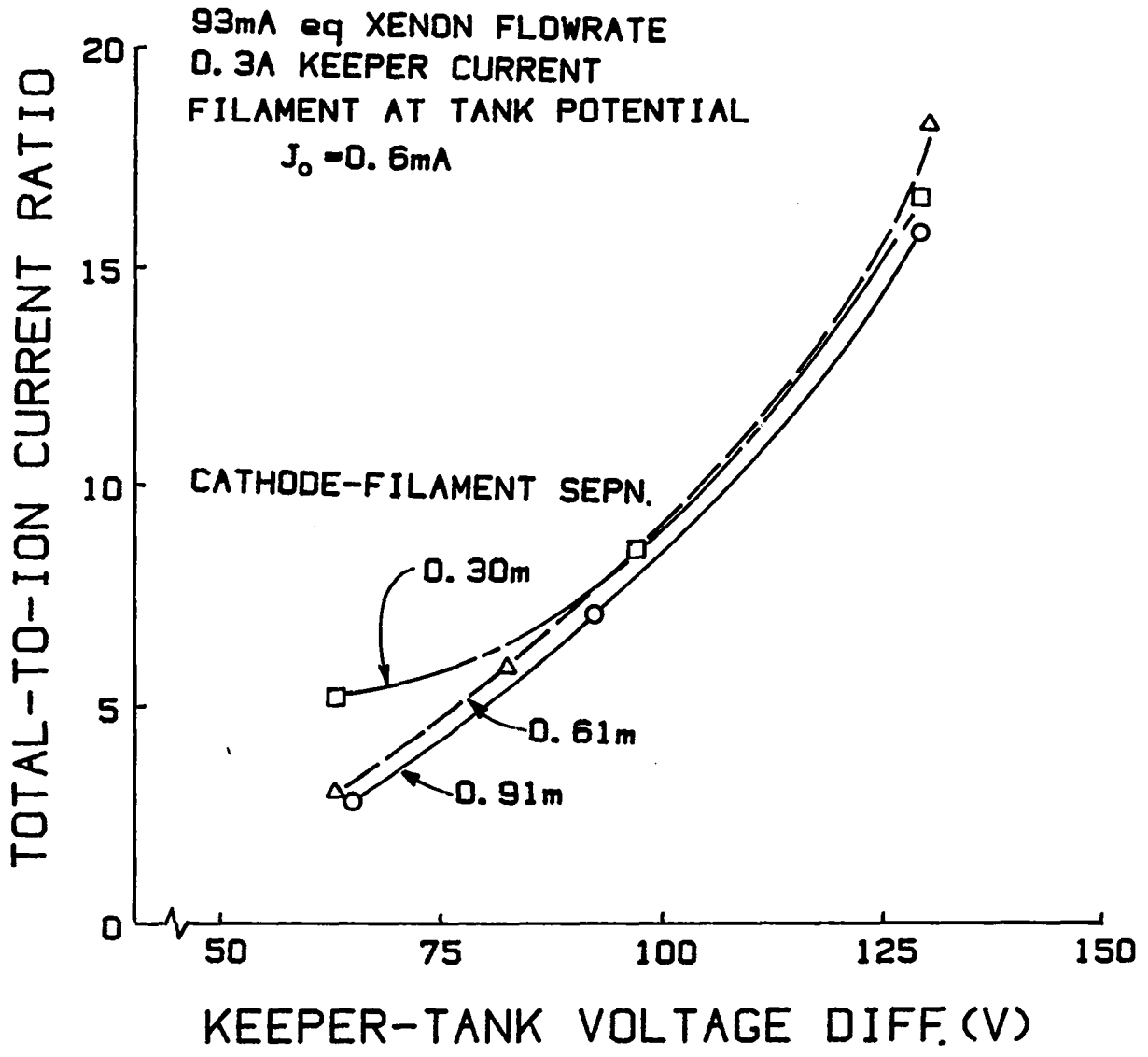

Fig. 23 Effect of Cathode - Filament Separation Distance on the Electron Collection Capability of the Hollow Cathode

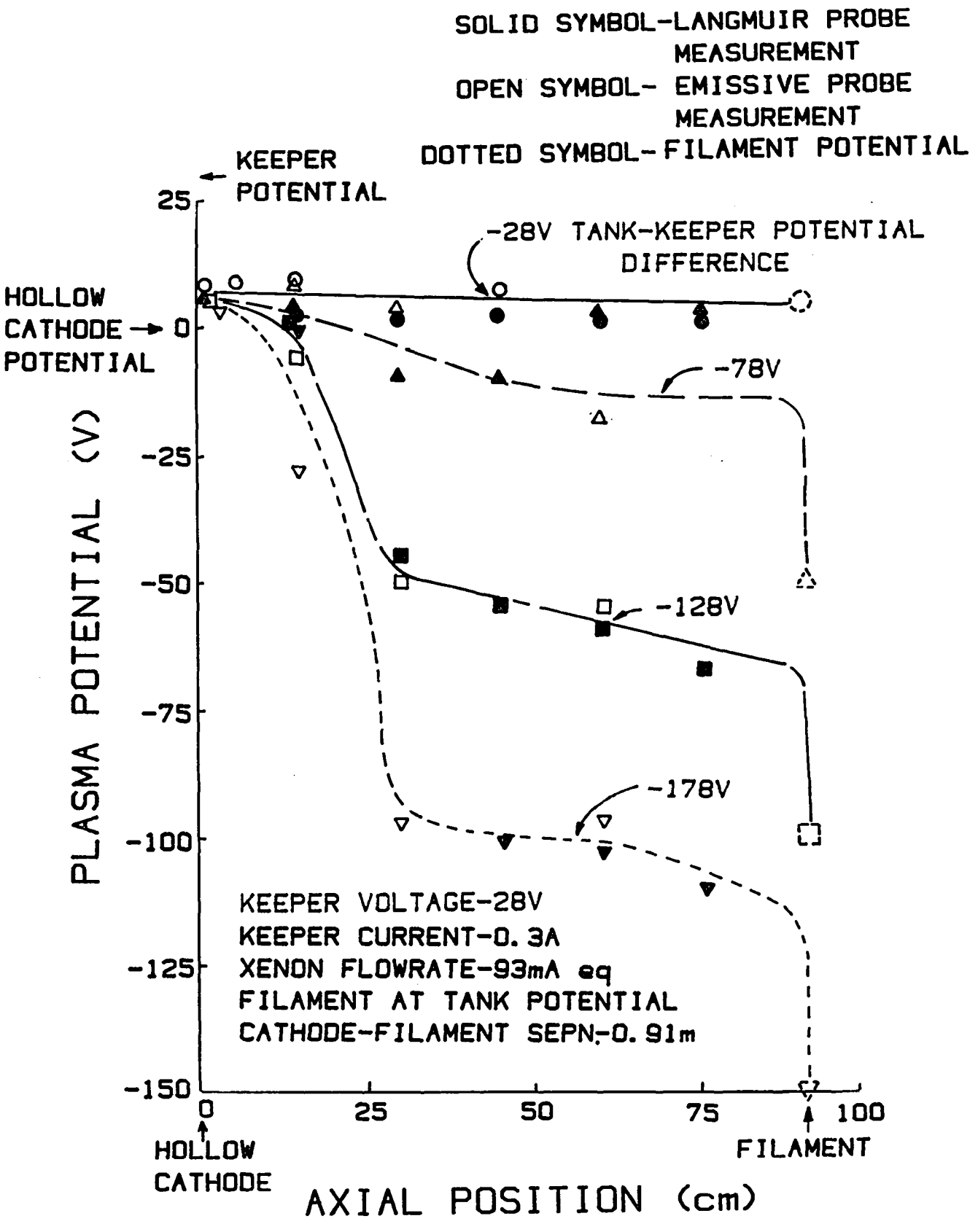

Fig. 24 Plasma Potential Profiles Between an Electron Collecting Hollow Cathode and a Filament

tank/ filament potential was 28, 78, 128 and 178 V below hollow cathode plasma potential.

The data presented in Fig. 24 show two or possibly three regions where large potential drops, suggestive of sheaths, have developed. One sheath, located within the first few cm downstream of the keeper, seems to be present on all four plots. A second sheath extending to a point about 30 cm downstream and a third at the filament are apparent only when the filament is biased negative of the cathode. Due to mechanical limitations, potential measurements could be taken no closer than 1.5 cm downstream of the keeper. The first sheath seems to exist within this region, so the measurements do not show any detail of its structure. The second sheath observed between 1.5 and 30 cm is assumed to coincide with the extent of the high density plume generated by the cathode. The detailed structure of the third sheath (at the filament) is also not apparent from the data.

The data of Fig. 24 were obtained using both Langmuir and emissive probes because of the uncertainty associated with interpretation of the Langmuir probe traces. Most of the Langmuir and emissive probe data of Fig. 24 do seem to agree within several volts, but the collection of additional data is planned to increase the confidence of these results.

Langmuir probe measurements also provide the electron density at the locations where probe traces are obtained. For the operating conditions associated with the circular data points and the solid line of Fig. 24 the density measurements shown in Fig. 25 were obtained. This plot shows that the Maxwellian electron density, which is usually within a few percent of the total electron density, drops rapidly from near $10^{9}cm^{-3}$ at the cathode to $10^{6}cm^{-3}$ near the filament. When the cathode was biased 50, 100 and 150 V positive of tank/filament

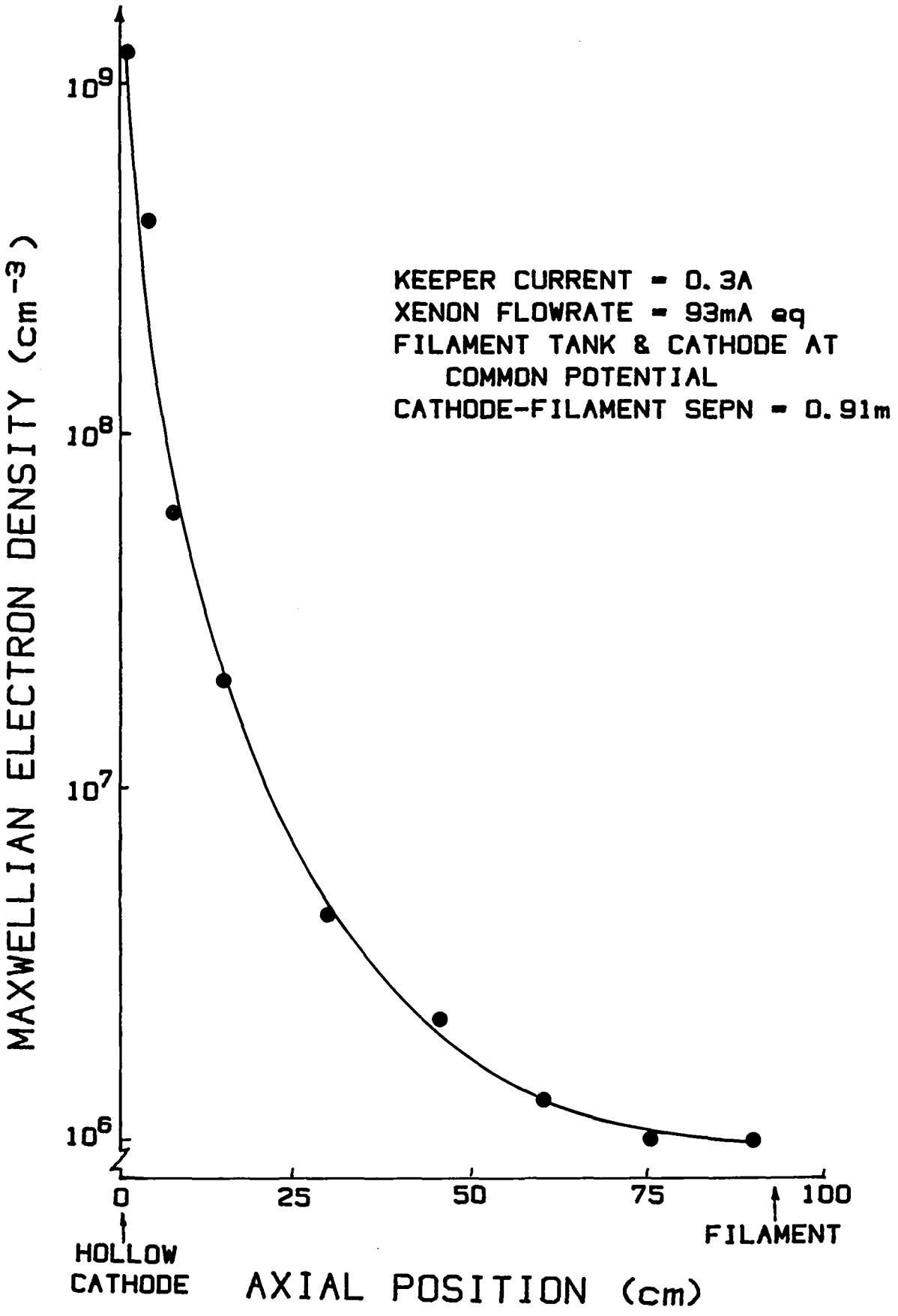

Fig. 25 Plasma Density Profile for Xenon Hollow Cathode

potential the densities decreased somewhat but were still of the same magnitude as those shown for the zero bias case in Fig. 25. These data also show that the electron density has decreased to a magnitude in the mid $10^6 cm^{-3}$ range at the location of the sheath edge (30 cm) observed in the plasma potential data of Fig. 24. There is, however, no change in the nature of the plasma density plot apparent at this point in the data of Fig. 25.

Because the hollow cathode ion production rate has a dominant effect on the capacity of the plasma between the hollow cathode and filament to conduct currents, the effect of varying the ion production rate was examined. This was accomplished by changing the keeper current (J_K) to vary the hollow cathode discharge power. Typical data obtained when the keeper current was changed from 0.3 through 0.9A are shown in Fig. 26. Increasing the keeper current from 0.3 to 0.6 to 0.9A caused the ion production current (J_o) to increase in almost direct proportion (0.6 to 1.3 to 2.1mA) as the labels on Fig. 25 indicate. The data on this figure show that the total-to-ion ratio does decrease somewhat as ion production increases. If the model inherent in Eq. 6 were correct and there were no ion production due to filament electron/neutral background gas collisions these curves would be expected to be more nearly coincident. It is felt that the actual behavior departs slightly from the ideal behavior because of increased tank wall/plasma plume interaction that occurs when the plasma becomes more dense and therefore expands due to increased ion production. In general, however, it is argued that the data of Fig. 26 continue to support the double sheath model inherent in Eq. 6. This in turn implies that a good measure of a plasma contactors's ability to collect electrons correlates with its ability to produce low energy ions. It is noted that production of ion/electron pairs by electrons drawn from the filament should have caused the curves of Fig. 26 to rise as keeper current was increased. The fact that this did not occur in the

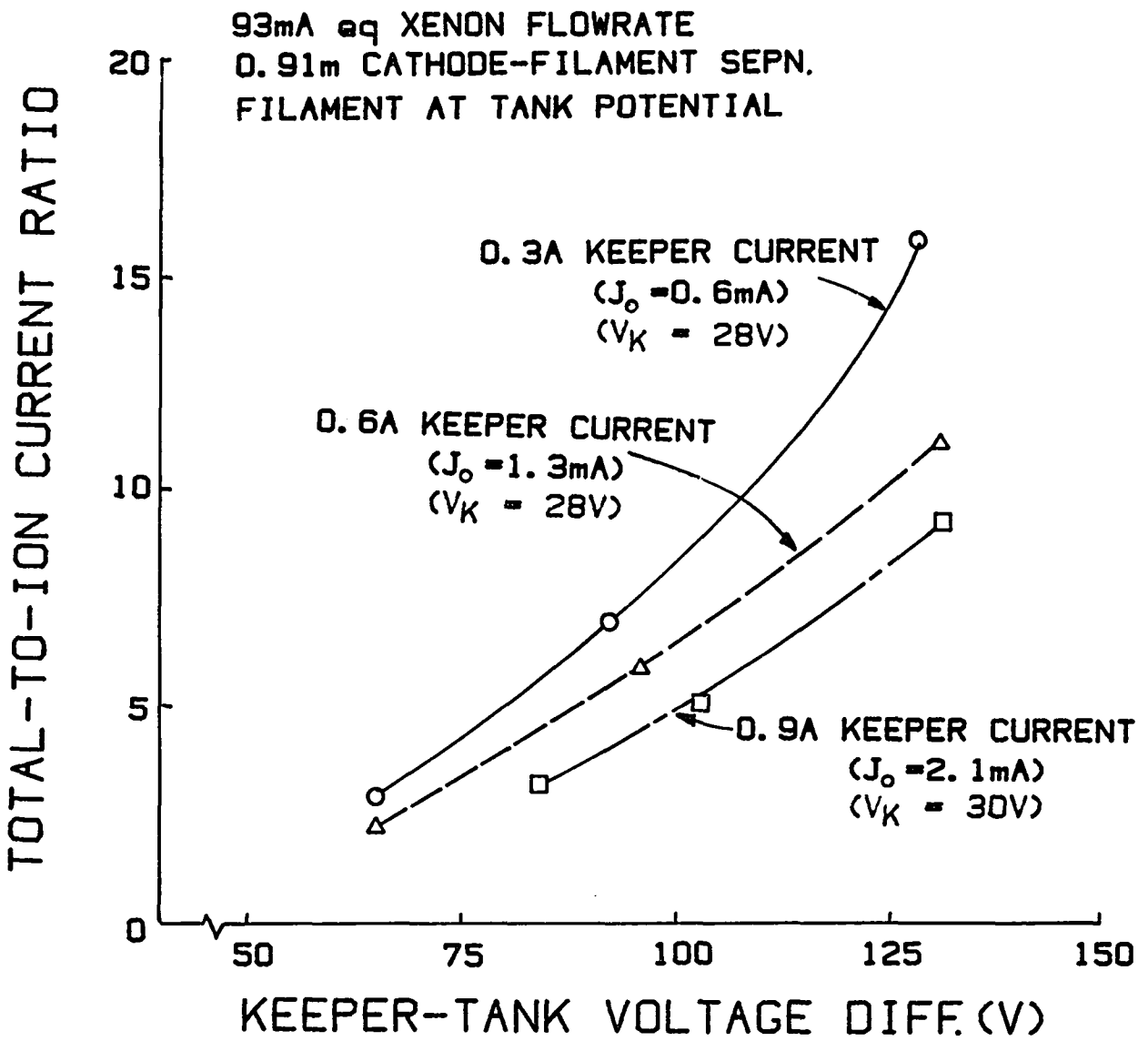

Fig. 26 Effect of Keeper Current on the Electron Collection Capability of the Hollow Cathode

data supports the postulate that very little filament electron induced ionization is occurring at the pressures where these experiments were conducted (< 6 X 10^{-6} Torr).

Dual Filament Experiments

It was expected that biasing two rather than one filament would provide twice the electron current to the hollow cathode. To test this hypothesis, an experiment was conducted in which the filaments configured as shown in Fig. 21 were positioned equidistant from the cathode (at x = ± 0.11m, y = 0, z = 0.91m) First one filament was heated separately and the electron current drawn from this heated filament to the hollow cathode was measured as a function of keeper-to-filament bias. The test was then repeated for the other filament. Next both filaments were heated and the current drawn from both of them was measured as a function of keeper-to-filament bias. The results obtained from this experiment are shown in Fig. 27. They indicate that the current drawn when both filaments were hot was less than the sum of the currents drawn in the individual filament tests (70% of the sum). This result suggests once again that the ions play a crucial role in determining the overall behavior of the system. It is postulated that the operation of a single filament causes the ions to be attracted preferentially toward that filament while the plume splits and becomes therefore more diffuse when both filaments are heated.

To explore this phenomenon further the filaments shown in Fig.21 were moved closer to the cathode (z = 31 cm). The left-hand side of Fig. 28 depicts the test configurations used for the experiment in the form of a view (along the Z axis) of the cathode and filaments. These diagrams show the position of the hot filaments (*) relative to the cathode (0). For example, in the upper diagram, the filaments are 31 cm downstream of the cathode, at the same elevation as the

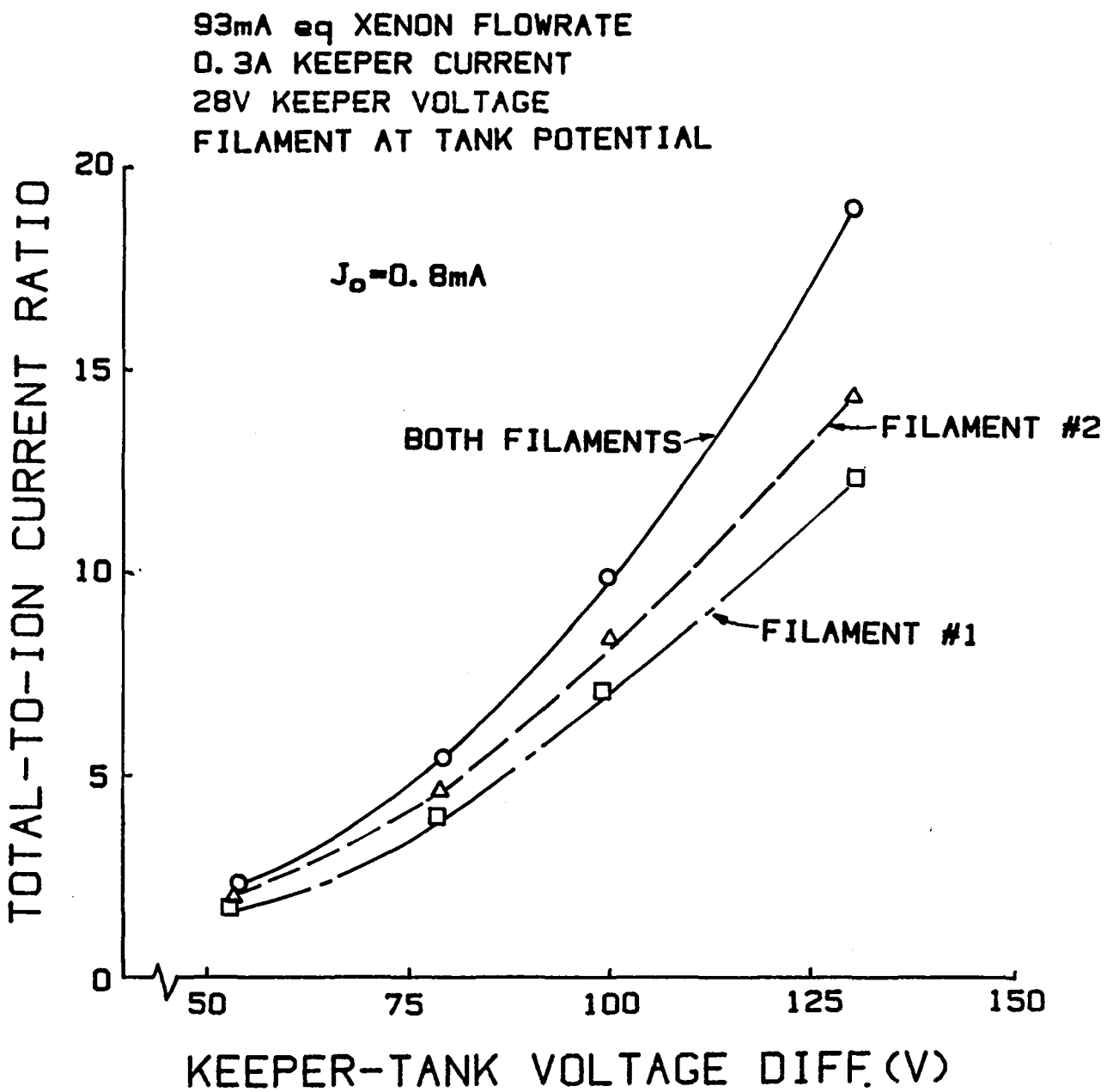

Fig. 27 Effect of Diffusing the Emission on the Electron Collection Capability of the Hollow Cathode

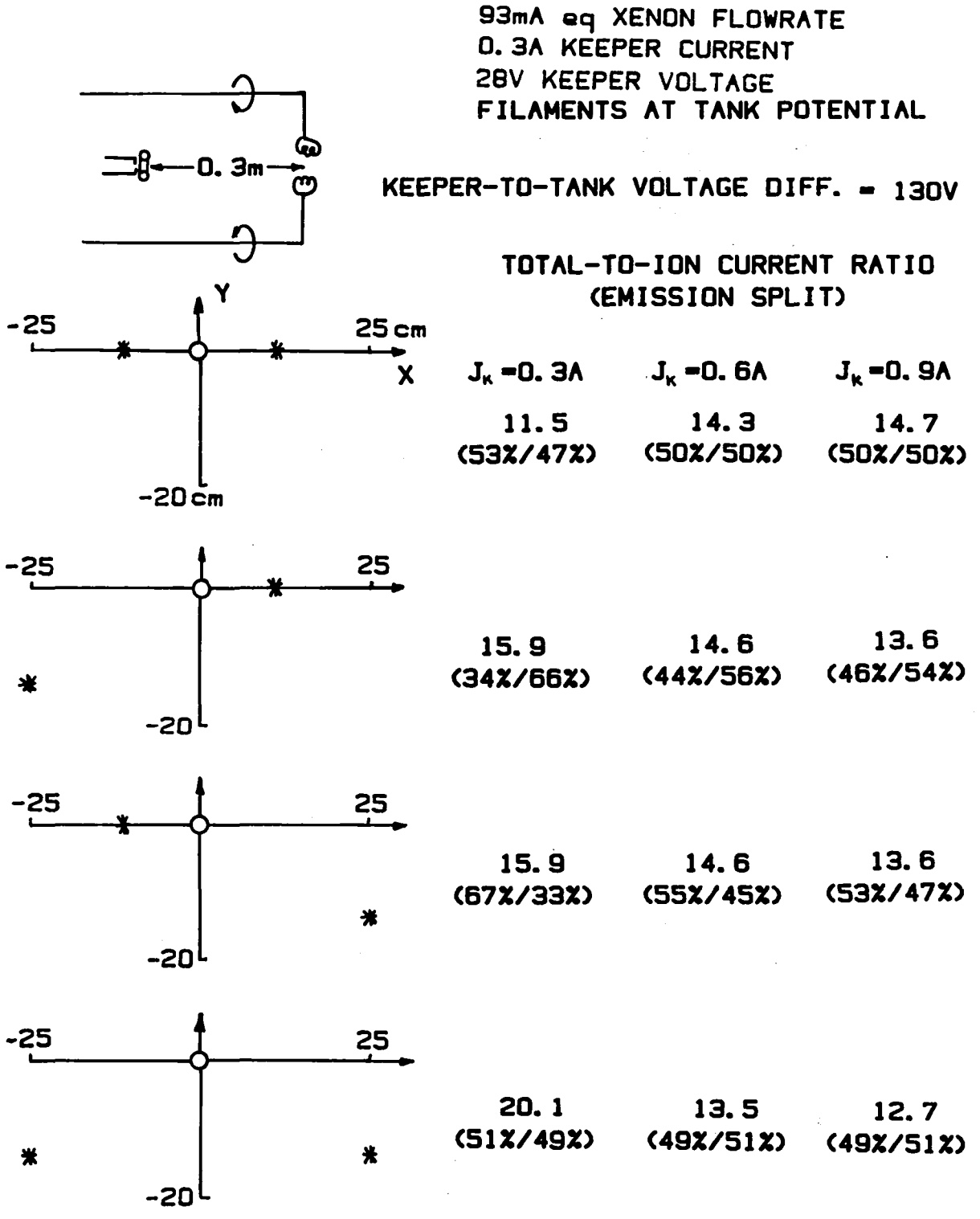

Fig. 28 The Effect of Filament Location on the Electron Collection Capability of a Hollow Cathode

cathode and 11.5 cm on either side of the cathode centerline. To the right of each sketch in Fig. 28, the corresponding ratios of total electron current collected by the cathode when its keeper was biased 130 V above the filament potential to the ion production current (J_o) at three different keeper currents (J_K) are given. Under each current ratio (in parentheses) is the fraction of this total current that was drawn from each of the two filaments. In conducting this test the filaments, biased negative relative to cathode, were first positioned equidistant from the cathode (upper sketch). Next, one filament was moved further away from the cathode centerline by rotating the filament support rod through a 90^o angle. This procedure was next repeated with the other filament. Finally both filaments were moved to their more distant position from the cathode centerline.

At a 0.3A keeper current Fig. 28 shows the collected electron current was 11.5 times the ion production current and roughly half of the collected current came from each filament when both filaments were closest to the cathode (upper sketch). When the left filament was moved further from the hollow cathode (14 cm below and 25 cm to the left of it) the electron current collected by the hollow cathode increased to 15.9 times the ion production current and the bulk of the filament emission current was drawn from the closer (right) filament. When the positions of the filaments were reversed (sketch 3) the distribution reversed, but the electron current collected by the hollow cathode remained the same. Moving both emitting filaments to the more distant positions (14 cm below and 25 cm abreast of the cathode) caused the electron current collected to <u>increase still further</u> and the distribution of emissions from the two filaments to equalize again. It is postulated that this strange behavior wherein the currents collected by the cathode increase as the filaments are moved further away again is related to ions produced in the cathode discharge being

repositioned to improve the plasma conductivity. It is also possible that the observed effects could be related to a situation where the filaments while being moved physically further from the hollow cathode were being moved onto geomagnetic field lines that passed closer to the cathode. Measurements of the earth's magnetic field revealed, however, that the movements suggested in Fig. 28 resulted in an increase in both the physical and orthomagnetic field distances. Additional testing is planned to investigate the effects of the local magnetic field on the coupling process. In these tests the magnetic field will be controlled from near null to values in excess of the geomagnetic value.

When the keeper current was increased above the 0.3A value pertaining to the data just discussed the trends changed and increasing the radial location of the filaments caused the electron current drawn to the hollow cathode at a given bias voltage to decrease. A 0.9 A for example for example the data of Fig. 28 show the electron current collected by the hollow cathode assembly decreases monotonically as the filaments are moved further away, and the distribution of the current drawn from the two filaments remains more evenly split. This trend suggests that the odd behavior only occurs at low discharge powers where the ion production rate is low. Thus it is presumed that the phenomena being observed are related to a redistribution of the plasma that is controlled by the ions being produced in the cathode discharge.

Finally, it is noted that increasing the distance between an emitting filament and a hollow cathode biased to collect electrons from the filament would be expected to increase the ion production current J_o if filament electron induced ionization were significant. Because this contribution to J_o was neglected in computing the ratios given in Fig. 28, including it, if it could be done, would tend to make the trend more reasonable for the 0.3 A keeper current data.

Quantitatively, however, the 30% increase in filament-to-cathode distance would not be expected to induce the 75% increase in total-to-ion current ratio observed between the top and bottom configurations in Fig. 28. In addition, doubling and tripling the filament-to-cathode distance for the case of single filament on the cathode centerline (Fig. 23) resulted in essentially no change in the total-to-ion production current ratio. This suggests that filament electron ionization while it would tend to produce a trend in the proper direction to explain the trend in the data for the J_K = 0.3 A case of Fig. 28 can not be supported quantitatively by measured results. Finally it is noted that the calculated mean free path for ionization of xenon by filament electrons is greater than 60 m at prevailing pressures so in the ~1 m distances involved very little ionization would be expected by these electrons.

Tank Wall Perturbation Study

One additional experiment was conducted which relates to the perturbing effect of the tank walls on the electron collection capability of the hollow cathode. In order to minimize the effects of the tank wall one would prefer to have them as far from the plasma as possible and to have them at a potential that would cause neither ions nor electrons to behave differently than they would in a space test environment. It had been determined early in the testing that having the filament and the tank walls at the same potential introduced a mininal effect on the filament/hollow cathode coupling process when the hollow cathode was centered in the 1.2 m dia. tank. It remained to determine if changing the distance from the plasma plume to the tank walls would change the perturbing effect of the walls. The effect of increasing the distance to the walls from the test facility diameter (1.2 m) could not be examined so the effect of reducing this diameter was investigated. This was accomplished by pulling the

hollow cathode/filament test set up back from the 1.2 m dia. tank until it was completely enclosed within the 0.4 m dia. bell jar shown in Fig. 19. With the filament cold, it was determined that the ion production current (J_o) was the same in the tank as it was in the bell jar. Similarly the electron emission portion of the hollow cathode characteristic curve (Fig. 21) was unaffected by the diameter of the test enclosure. When the electron collection characteristics were measured in the two enclosures the data shown in Fig. 29 were obtained. These data suggest that the performance is similar for both cases at the low keeper power condition where the test was conducted. The 0.4 m dia. bell jar may facilitate the slightly higher electron collection currents either because of magnetic field effects or because the pressure is slightly higher in the bell jar than it is in the tank.

Conclusions

The basic xenon hollow cathode used in this study has been shown to emit electron currents in excess of 3 A when it is biased so its keeper voltage is a few volts negative (<10 V) of a collection surface about a meter away. It is believed, therefore, that it will function well as a low impedance electron source on the end of the electrodynamic tether which emits electrons. The electron collection capabilities of the basic hollow cathode appear from preliminary tests to be less certain. In both the electron emission and collection modes of operation, the availability of cold ions is the key to the realization of a low impedance but in the electron collection mode it appears to be more important. In the tests reported here these cold ions were produced in the hollow cathode discharge. Preliminary tests conducted with a heated filament as an electron source show that hollow cathode electron collection currents are about twenty times this hollow cathode ion production rate at driving potential differences

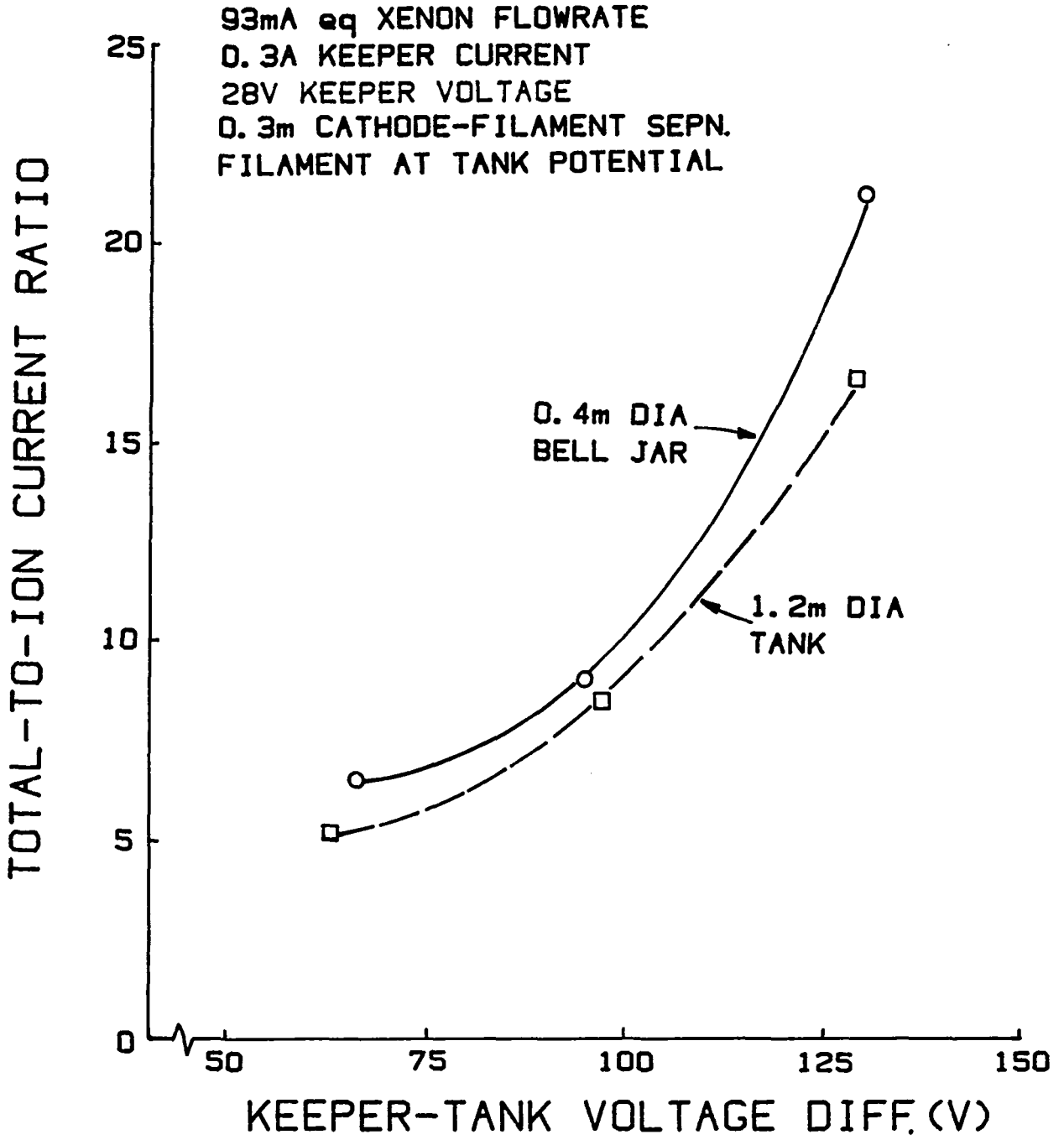

Fig. 29 Effect of Confining Wall Proximity on the Electron Collection Capability of a Hollow Cathode

of about 100 V. The magnitude of this ratio of electron current collected to ion production rate in the hollow cathode discharge increases as the number of filaments being used is increased. The placement of these filaments also has an effect on this ratio. The plasma that exists between a hollow cathode collecting electrons and an emitting filament exhibits substantial voltage drops that suggest the existance of sheaths at the emitting filament and at an interface that may be at the edge of a high density hollow cathode plume. For the tests reported here this interface appeared to occur 25 cm from the cathode where the electron density was of the order of $10^{7}cm^{-3}$. There was also some evidence of a third sheath located within about a centimeter of the hollow cathode.

It is noted that these tests were conducted in a low pressure environment ($<10^{-5}$ Torr) where calculations suggest ionization by electrons drawn from the filament was unimportant. Increasing this pressure could result in a substantial increase in this ionization mechanism and as a result the cold ion density would increase. This would faciliate lower impedance operation of the plasma contactor. The results show that the presence of cold ions is required for low impedance plasma contactor operation, but the source of these ions appears to be less important.

HIGH PRESSURE HOLLOW CATHODE RESEARCH

Craig Luebben

Arc jet thrusters operate at values of specific impulse that are near optimum for many near-earth missions of current interest. These thrusters use a solid thoriated tungsten cathode that has been observed to melt because heating is concentrated at the small spot on its tip where electron emission occurs. Thus, it is questionable whether these conventional cathodes are suitable for a long term space application. The hollow cathode developed to supply electrons for ion thrusters, on the other hand, emits electrons from the relatively large surface area on the cylindrical inner surface of the cathode insert, and when operating properly it does not overheat. The hollow cathodes developed for ion thruster applications operate at interelectrode pressures of about 10^{-3} Torr while arc jet thrusters operate at pressures up to 1000 Torr so the use of ion thruster hollow cathodes in this application is not straightforward. This study has been undertaken to determine if an ion thruster hollow cathode or some modification of this device might operate satisfactorily in the high pressure regime of the arc jet.

Apparatus and Procedure

The test apparatus used in this study is shown schematically in Fig. 30. It is similar to the apparatus used in last year's work[19] to study xenon and nitrogen discharges except that the cylindrical anode was changed from stainless steel to tantalum. This change was required because it was found that the stainless steel anode tended to vaporize at interelectrode pressures above about 10 Torr. The standard test configuration included a 5.5 mm id, tantalum, open-ended hollow cathode and a 5 cm diameter anode. The apparatus was installed in a 30 cm diameter by 45 cm high vacuum chamber.

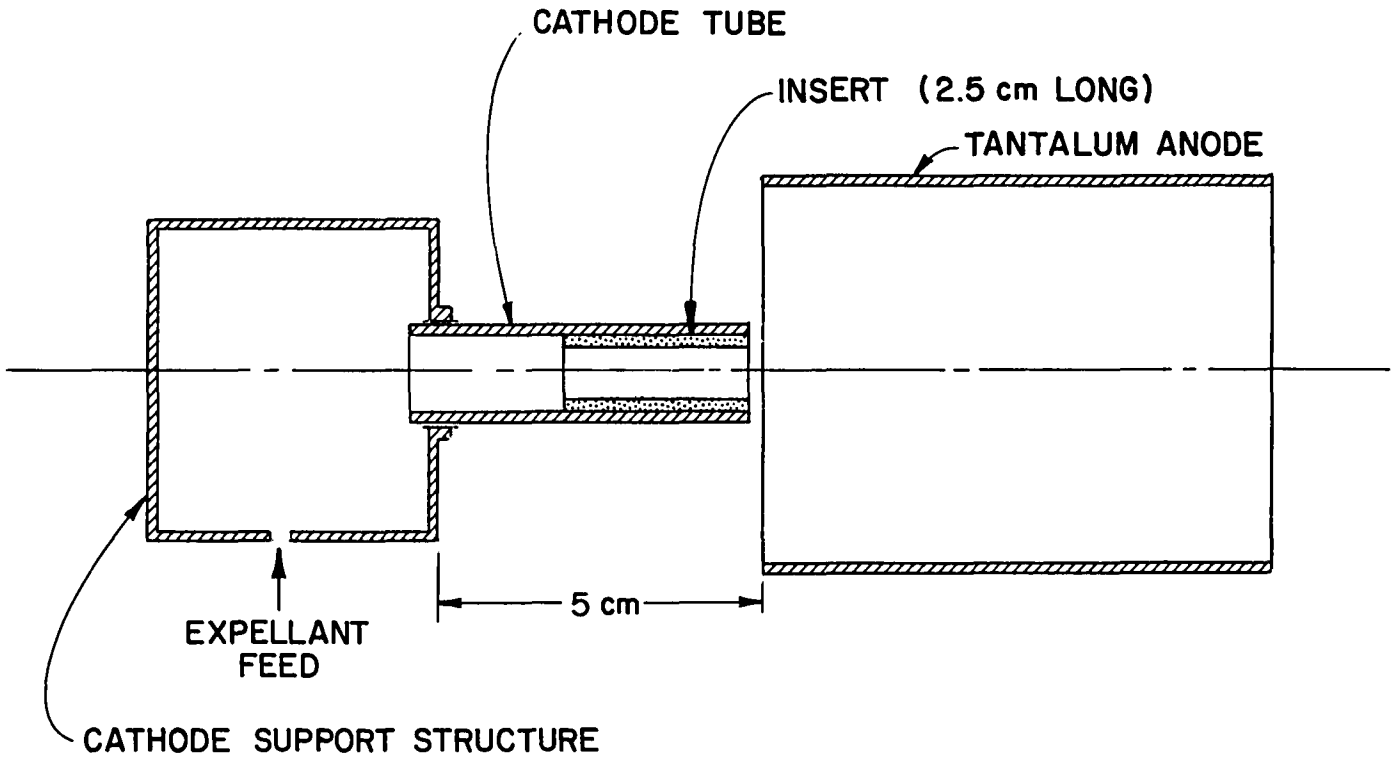

Fig. 30 Hollow Cathode Test Configuration

Since a major objective of this hollow cathode research effort was the achievement of cathode operation at high interelectrode pressures the basic approach used was to vary interelectrode pressure from the low range where the cathodes worked properly to the high range where problems developed. The problems encountered included an excessively high anode voltage required to sustain operation at a given discharge current, and the development of intense electron emission from a small spot usually on the exterior of the cathode. As problems were identified a variety of experimental parameters were varied in an effort to eliminate the problems or at least extend the operating pressure range. These parameters are listed in Table I, along with the changes associated with each parameter. Some of these parameters require some discussion. For example in the normal flow condition associated with hollow cathode operation flow passes from the cathode tube interior into the interelectrode region (i.e., toward the anode). It was also possible to turn off this flow and feed expellant directly into the bell jar (backfill) to increase the interelectrode pressure. When this was done it was designated "no flow" operation. It was also possible to evacuate the cathode interior during operation in the manner suggested in Fig. 31. This produced a reverse flow situation in the cathode tube in which expellant being fed into the bell jar was drawn through the tube in a direction opposite to electron flow.

Figures 30 and 31 both show open-ended cathode tubes. As Table I indicates, however, many tests were conducted with orifice plates installed. The orifice plates used were made of the same material as the cathode tube. Table indicates data were collected at discharge currents in the range from 1 A to 5 A. It would have been desirable to conduct tests at discharge currents up to 10 A where arc jets of interest operate, but the available power supply was limited to currents and voltages of 5 A and 180 V. During preliminary tests the ballast

Table I

Parameters Varied in Hollow Cathode Study

Parameter	Changes Introduced
Expellant	• Nitrogen • Ammonia
Expellant Flow Condition through Hollow Cathode	• Normal Flow (up to 72 sccm) • No Flow • Reverse Flow
Cathode Orifice Configuration	• No Orifice Plate (open-ended Tube) • 1.5 mm dia • 0.89 mm dia • 0.46 mm dia
Cathode Insert	• R-500 Treated Tantalum Foil • Untreated Tantalum Foil • Barium Aluminate Impregnated, Sintered Tungsten • Lanthanum Hexaboride
Discharge (Anode) Current	• 1 A to 5 A
Anode Configuration	• 5 cm dia Tantalum Cylinder • 1.7 cm dia Tantalum Cylinder
Cathode Tube Configuration	• 5.5 mm i.d. Tantalum Tube • 6.1 mm i.d. Quartz Tube • 4.3 mm i.d. Alumina Tube

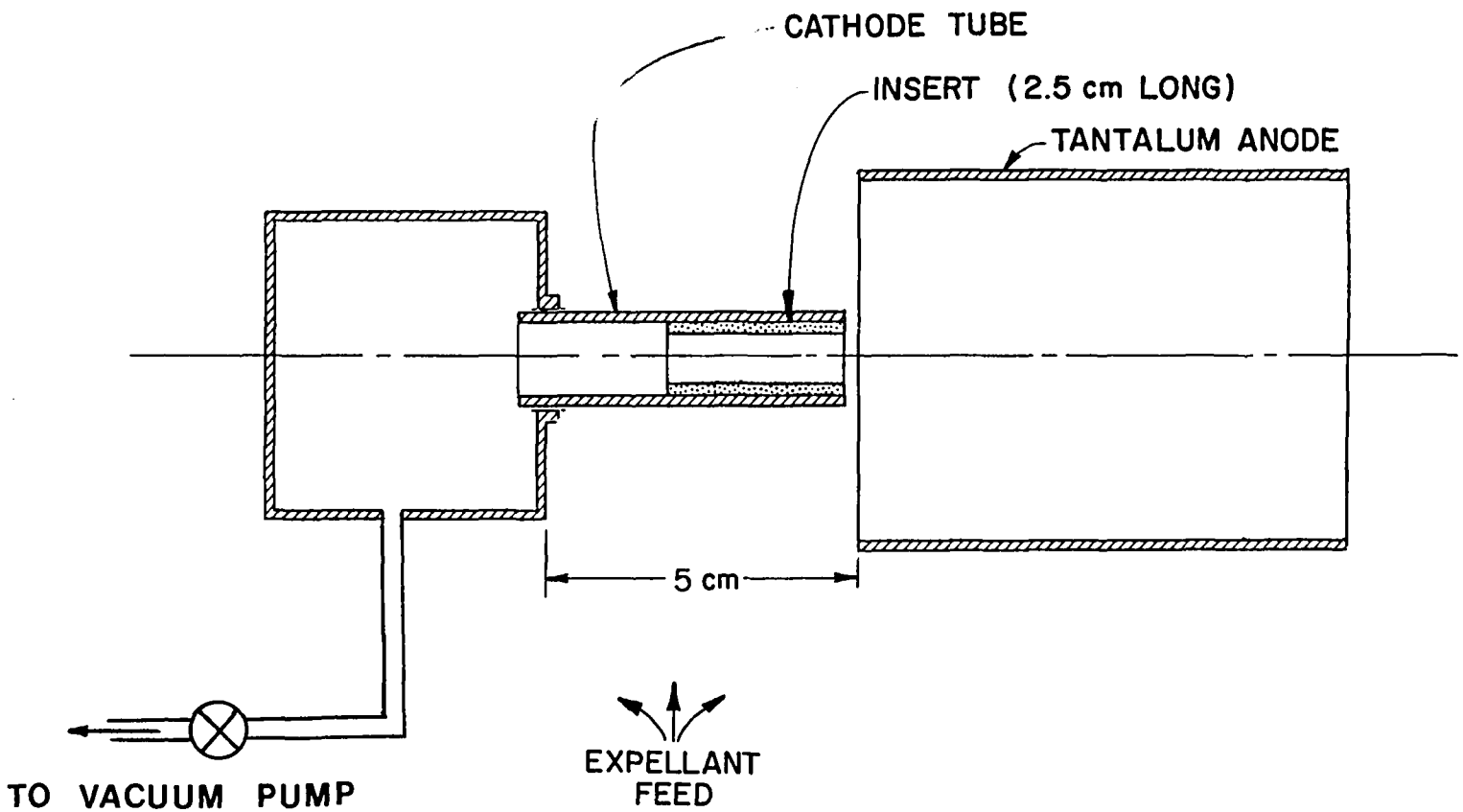

Fig. 31 Evacuated Cathode Test Configuration

resistor (which is required to limit and control the current) and the power supply were observed to overheat when they were operated at high pressures and currents greater than 4 A. Hence, a 4 A discharge current was selected for the bulk of the testing, and the anode (or discharge) voltage was limited at 180 V as mentioned above.

The plasma potential in the interelectrode region was measured using an emissive probe that could be moved both axially and radially throughout this region. This probe, which provided a direct readout of plasma potential, should be accurate to within a few volts. This accuracy is considered adequate because the primary concern in these tests is the relative magnitudes of the cathode fall, the bulk plasma voltage drop, and the anode fall. Figure 32 shows the effect of varying the heating (filament) current through an emissive probe at a location where it should indicate a plasma potential near the anode voltage. The probe begins to indicate properly as the filament current rises above 1.28 A where the inflection point is observed in the curve. At this point the probe should float at a potential that is nearly equal to the plasma potential. For this work the probe has been operated at a filament current that is about 10% greater than the inflection point current. This criterion, which has been suggested by Aston[21], is based on his comparisons of emissive and Langmuir probe data. Thus, probe currents from 1.35 to 1.40 A were used during testing.

The plasma potentials at three axial positions downstream of the cathode were measured at various interelectrode pressures. Figure 33 shows the probing locations relative to the cathode and anode used in the tests. Equipotential maps that were obtained from extensive axial and radial potential measurements in preliminary experiments conducted at low pressures (< 1 Torr) indicate that the plasma potential 4 cm axially downstream from the cathode (point 3) is essentially the same as the plasma potential near the anode surface. Hence, the

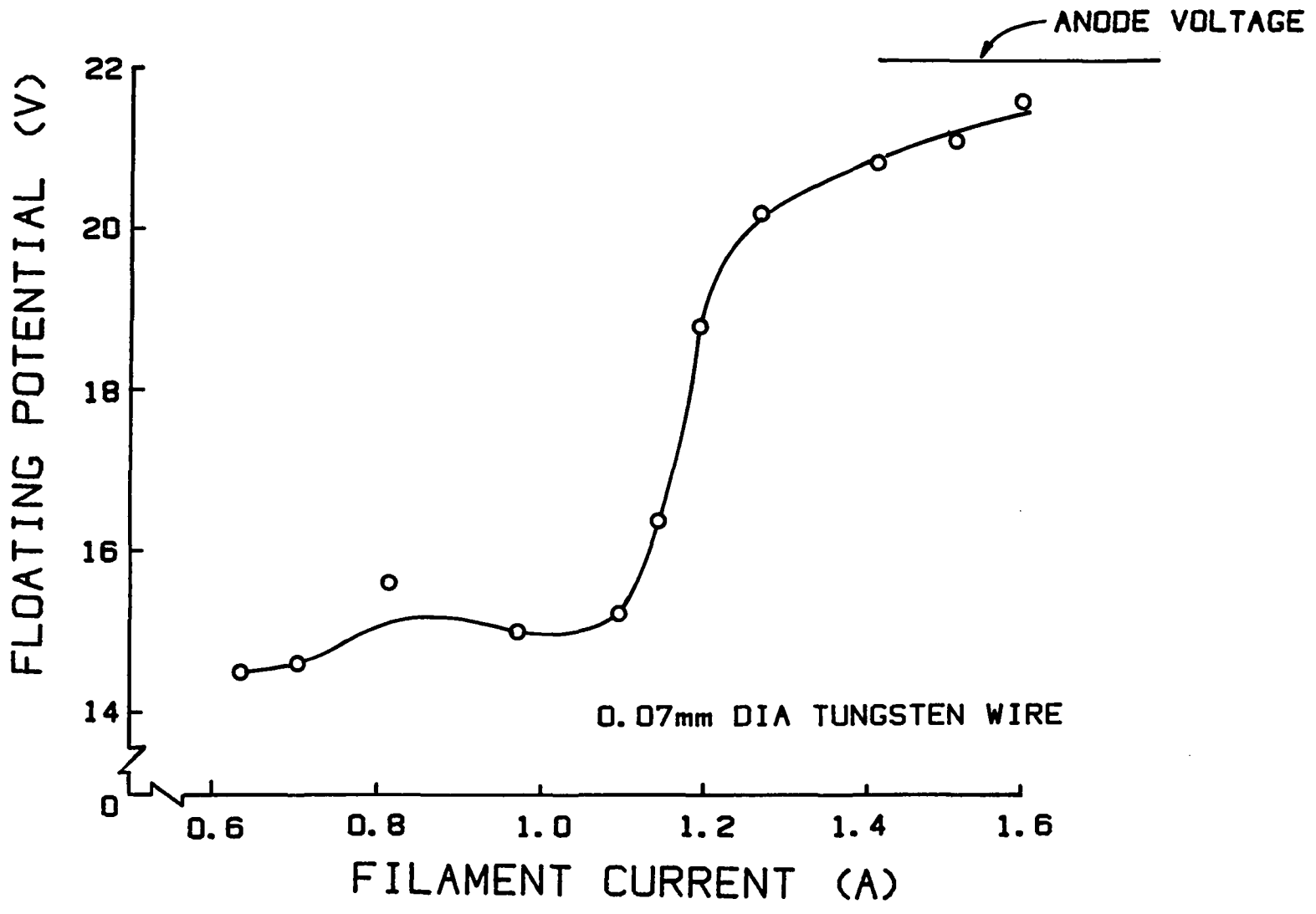

Fig. 32 Emissive Probe Characteristic

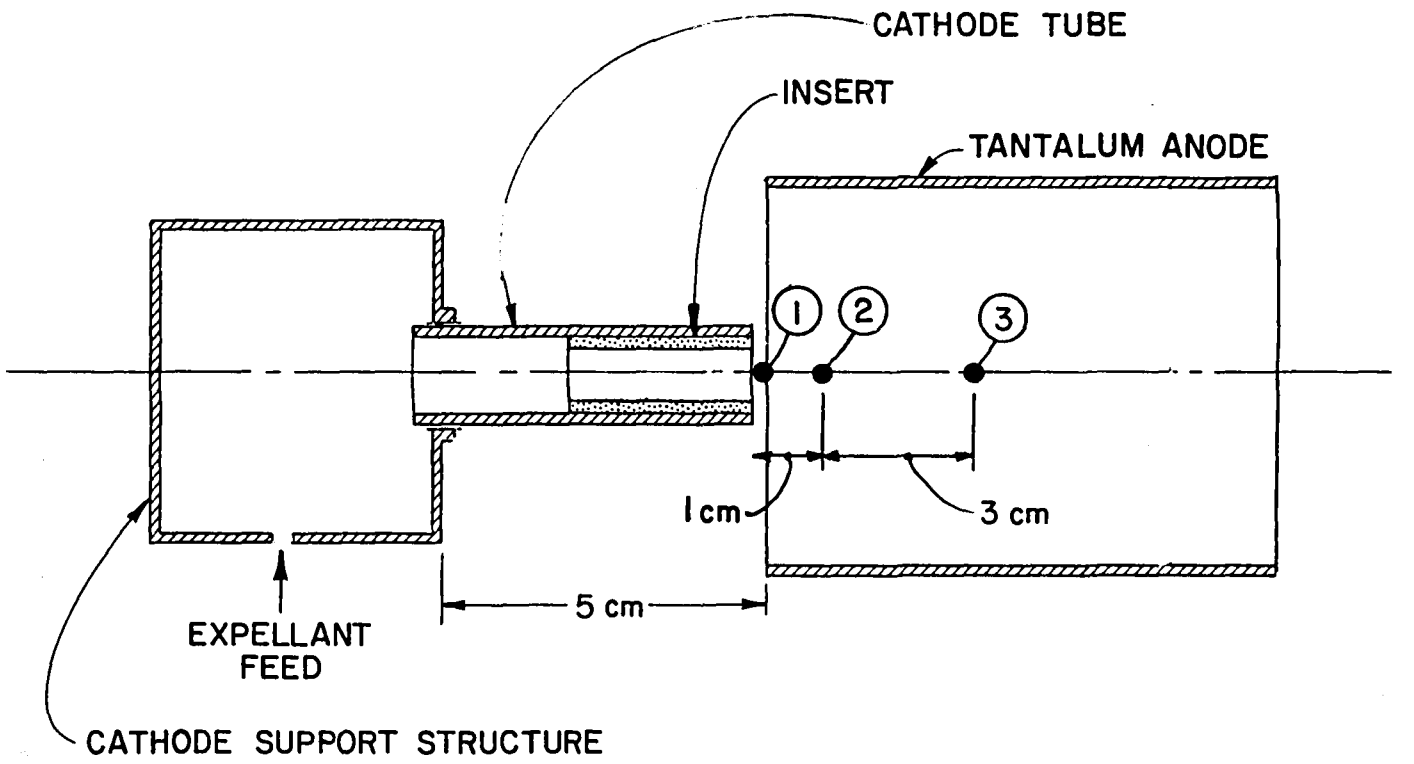

Fig. 33 Probing Location Diagram

difference between the anode voltage and the plasma potential at point 3, for a given pressure, is taken to be the anode fall. Since the cathode voltage is the reference voltage (zero), the cathode fall is merely the plasma potential measured at the cathode exit (point 1). It is noted that the probe can be overheated in the vicinity of the cathode, particularly at higher pressures, so the probing must be performed rapidly to avoid melting the probe.

The test procedure involved establishing an expellant flow rate of around 35-70 sccm through the cathode while maintaining the bell jar pressure at about 0.20 Torr. A potential of several hundred volts was applied to the anode using a startup power supply and usually a floating "tickler" electrode was then touched to the cathode orifice plate to initiate the discharge. This tickler was simply an isolated length (3 cm long) of 0.5 mm dia tantalum wire attached to an insulator that could be touched to the cathode tip. When contact occurred it appeared that a tiny discharge occurred at the point of contact that could initiate the full discharge. Once the discharge started the anode potential was reduced drastically and control could be transferred to an operating power supply capable of sustaining the 4 A discharge current. The discharge was allowed to run at 4 A for several minutes to insure stable operation. The bell jar was then isolated from the vacuum pump and backfilled with gas to increase the interelectrode pressure, which was measured using either a thermocouple vacuum gauge or a mechanical bellows gauge. At each interelectrode pressure of interest the anode voltage was measured while the discharge was observed visually. During some tests photographs of the discharge were taken and/or emissive probes were used to measure interelectrode plasma potential profiles.

Results

A test was conducted to show that the anode voltage is independent of the expellant flow rate, but is a function of interelectrode pressure. Ammonia expellant was used with an R-500 treated tantalum foil insert, a 5 cm dia anode and a tantalum tube cathode with a 0.89 mm dia orifice for the test, but the observed independence from cathode flow was observed with other configurations as well. In this test the anode voltage was recorded over a range of pressures from 0.20 Torr to 10 Torr using six different flow rates from 18 to 72 sccm. The independence of anode voltage from changes in cathode flow rate is shown by the data of Fig. 34. These data indicate that the cathode flow rate only influences anode voltage indirectly, i.e., to the extent that it influences interelectrode pressure. Similar results were also obtained in other tests at pressures above 10 Torr. Thus, the flow rate through the cathode was not controlled precisely during the tests to be described and a value will not be given in the test results. In the normal flow configuration the flow rate typically used, however, was between 35 and 50 sccm for ammonia, and between 50 and 70 sccm for nitrogen.

Typical results showing the effect of discharge current on the anode voltage versus interelectrode pressure characteristics are shown in Fig. 35 for an open-ended tantalum cathode with an R-500 treated tantalum foil insert and nitrogen expellant. The plasma exhibits a negative resistance characteristic, i.e., a decrease in discharge current requires an increase in anode voltage to sustain the discharge at a given interelectrode pressure. This condition exists because the resistance of the plasma to the flow of electrons is proportional to the ratio of electron collision frequency to electron density. With increasing current, the electron density increases faster than the collision frequency, so the resistance decreases, allowing the anode voltage to also decrease. The data

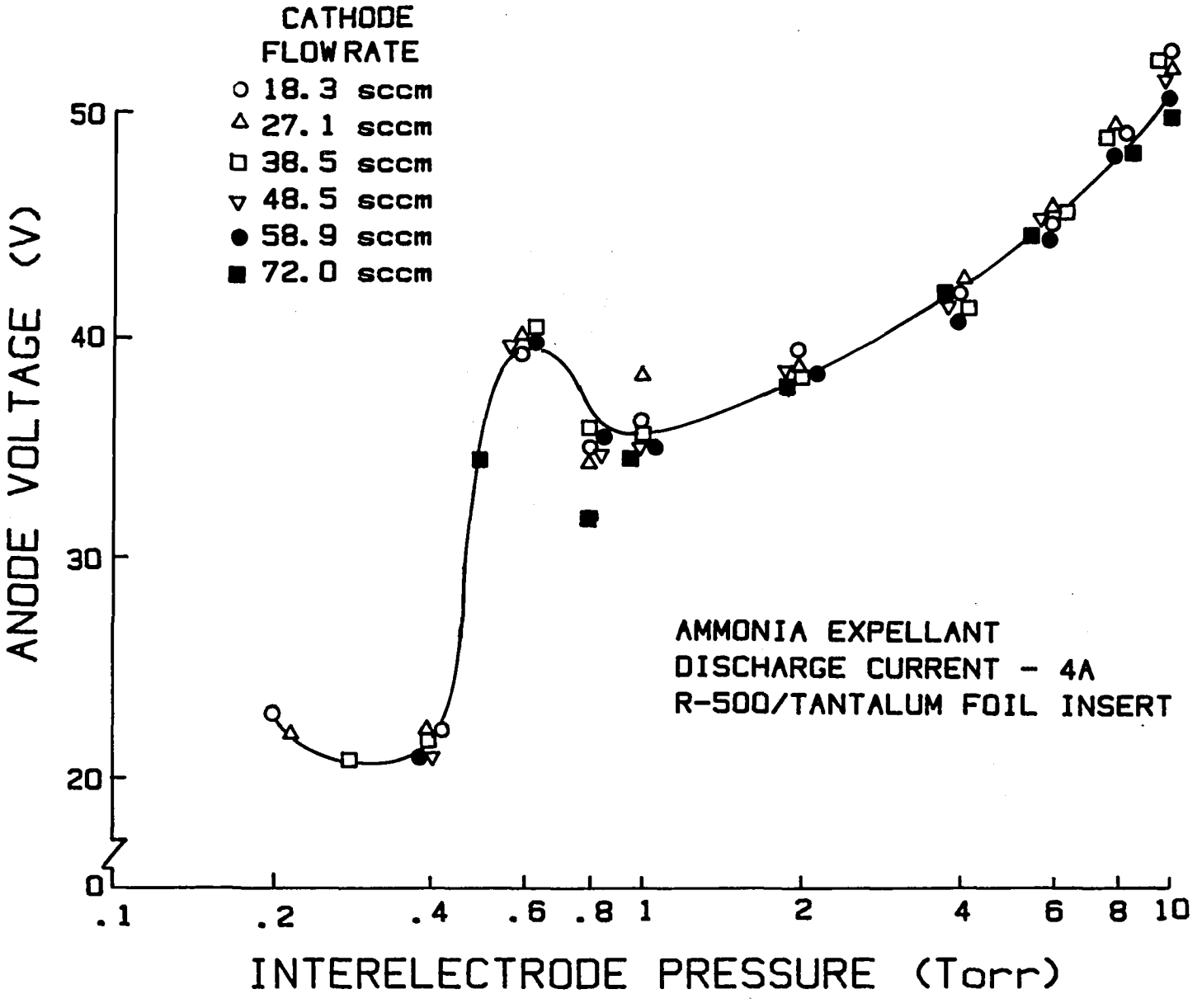

Fig. 34 Effect of Cathode Flowrate on Pressure/Voltage Characteristic (typical)

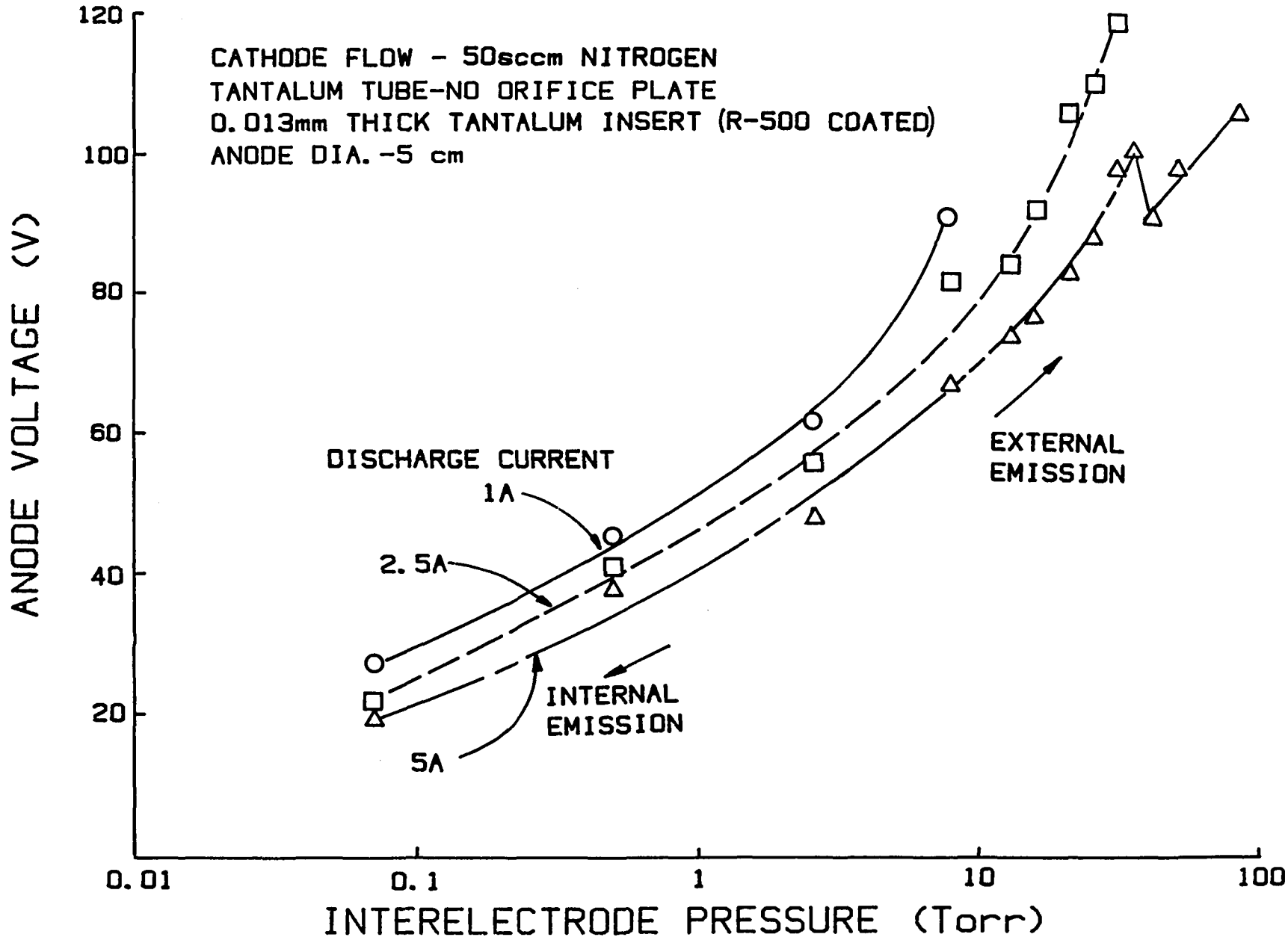

Fig. 35 Pressure/Voltage Characteristic of Nitrogen

of Fig. 35 show that a five-fold increase in current results in only a 20 to 30% decrease in anode voltage for a given pressure at the current levels shown.

As interelectrode pressure was increased the electron emission underwent a transition. At low pressures the emission was from the low work function insert surface inside the hollow cathode tube. After this transition the emission site was on the exterior surface of the cathode tube. Arrows below the curves on Fig. 35 show the regions where the emission was definitely internal (on the low work functon insert surface) and where it was definitely external (i.e., coming from the cathode tube). The transition between these two emission sites, which had been sudden and readily apparent when an orificed cathode tube was used,[19] was not so apparent when the tube was open-ended. As the data of Fig. 35 suggest this transition tended to occur gradually over the pressure range of 1 to 10 Torr when the open-ended cathode tube was used.

The nature of this transition can be understood by recognizing that a normal, internal hollow cathode discharge was observed only at low pressures (< 1 Torr). Pressure increases caused the primary electron mean free path to decrease, and thus the size of the electron emission region on the insert decreased. The length of the ion production region has been predicted to equal one or two primary electron mean free paths.[13] As the interelectrode pressure was increased through the range from 1 to 10 Torr for an open-ended hollow cathode the following phenomena were observed to occur: the emission length of the insert shrunk until the discharge appeared to come only from a thin, circular line at the downstream edge of the insert; next the discharge came from a bright emission spot which moved increasingly away from the insert onto the edge of the tantalum cathode tube, finally becoming an emission spot on the exterior surface of the cathode tube. This emission spot is undesirable because it does not provide uniform heating of the plasma, and, as with the conventional

cathodes, it will probably result in overheating and melting of the cathode. At the higher pressures when the emission site is off of the insert it is presumed that the work function at the point of emission is higher than it would be on the insert. It is possible, however, that barium from the insert migrates onto the tube thus reducing the work function below the value for pure tantalum. The likelihood of substantial barium mitration is certainly greater for the open tube cathode configuration than it would be for the orificed configuration.

Anode Voltage vs. Interelectrode Pressure for Various Inserts

Figures 36 through 39 compare curves showing the effect of interelectrode pressure on anode voltage for ammonia and nitrogen expellants with barium aluminate impregnated, sintered tungsten, lanthanum hexaboride, bare tantalum foil and R-500 treated tantalum foil inserts. Figure 36 shows data obtained with the tungsten insert impregnated with barium aluminate. At higher pressures the anode voltage required to sustain the 4 A discharge current is significantly greater when using ammonia expellant than when using nitrogen expellant. However, the discharge appears more stable and plasma heating appears more uniform when ammonia expellant is being used. Further, ammonia is attractive for space missions because it can be stored easily and it could be generated from crew wastes in space. With ammonia a power supply voltage limit was reached at about 40 Torr, whereas for nitrogen the discharge extinguished at about 80 Torr before the power supply voltage limit was reached. The nitrogen discharge appeared to be sustainable at pressures above 80 Torr for discharge currents over 4 A.

The data obtained using the lanthanum hexaboride insert, shown in Fig. 37 are similar to those obtained with the sinitered tungsten insert. At the lower interelectrode pressures the anode voltage is about 50% higher with the LaB_6 insert, but the voltage-pressure curves become increasingly coincident at higher

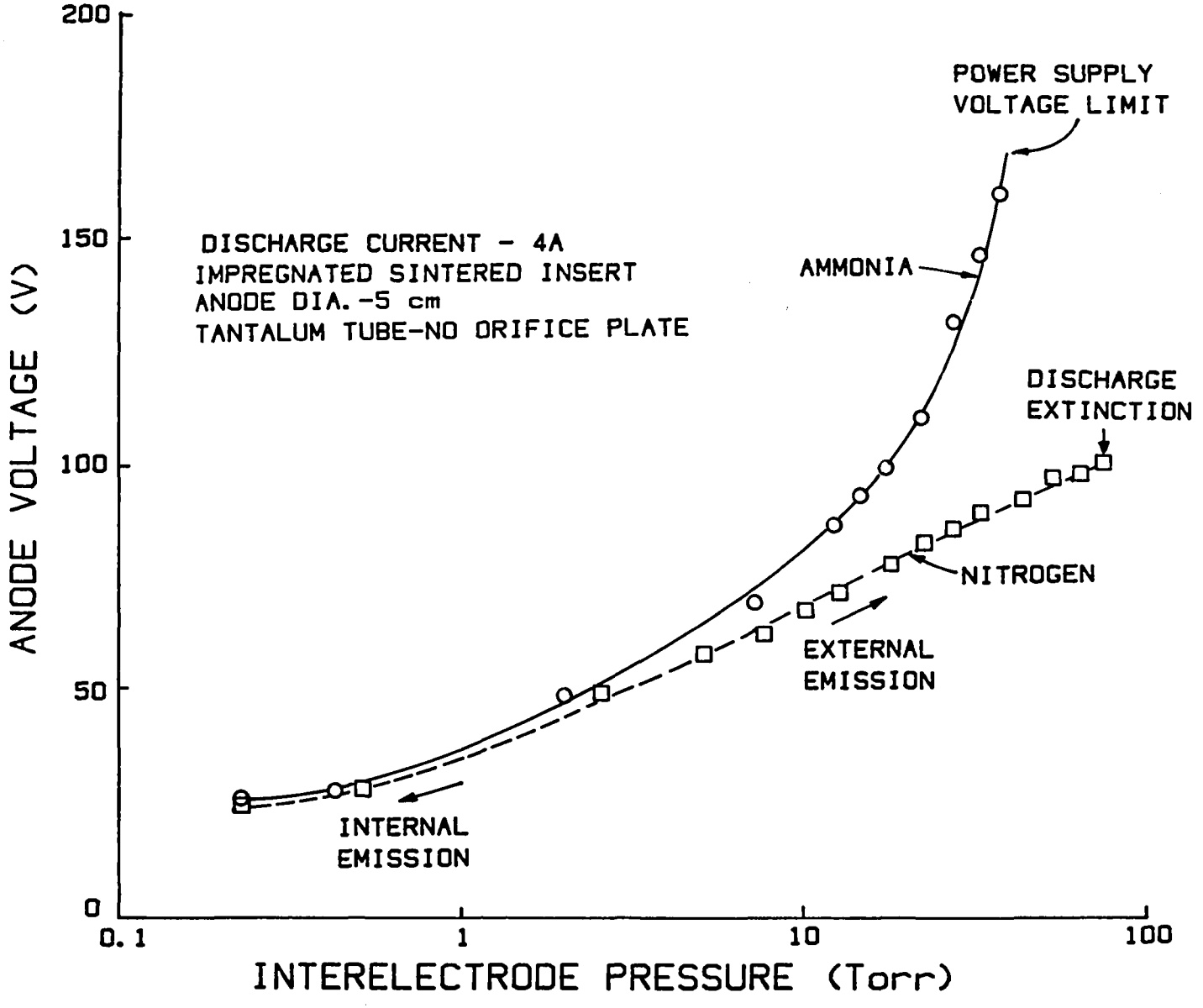

Fig. 36 Comparison of Nitrogen and Ammonia Characteristics - Sintered Tungsten Insert

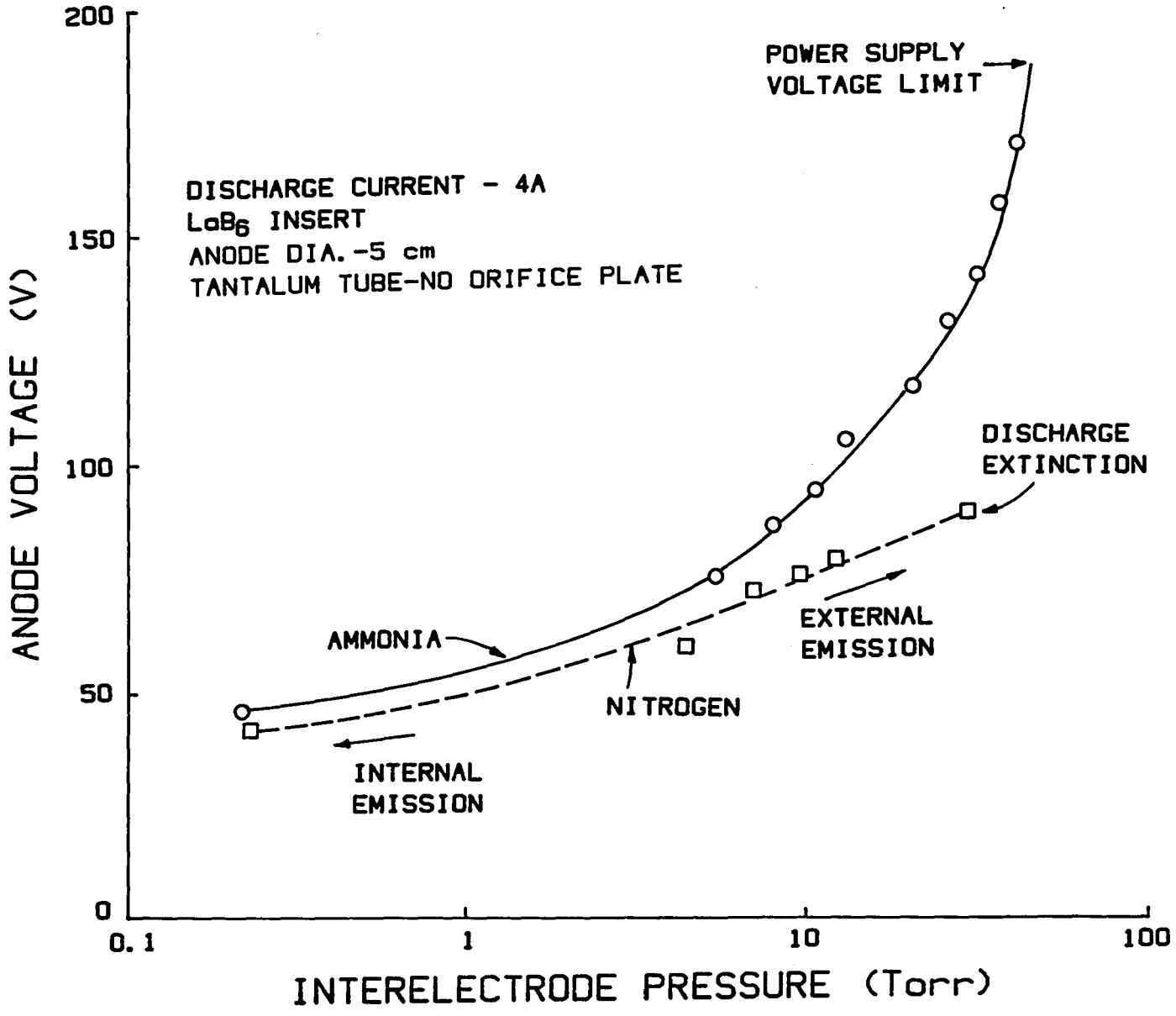

Fig. 37 Comparison of Nitrogen and Ammonia Characteristics - Lanthanum Hexaboride Insert

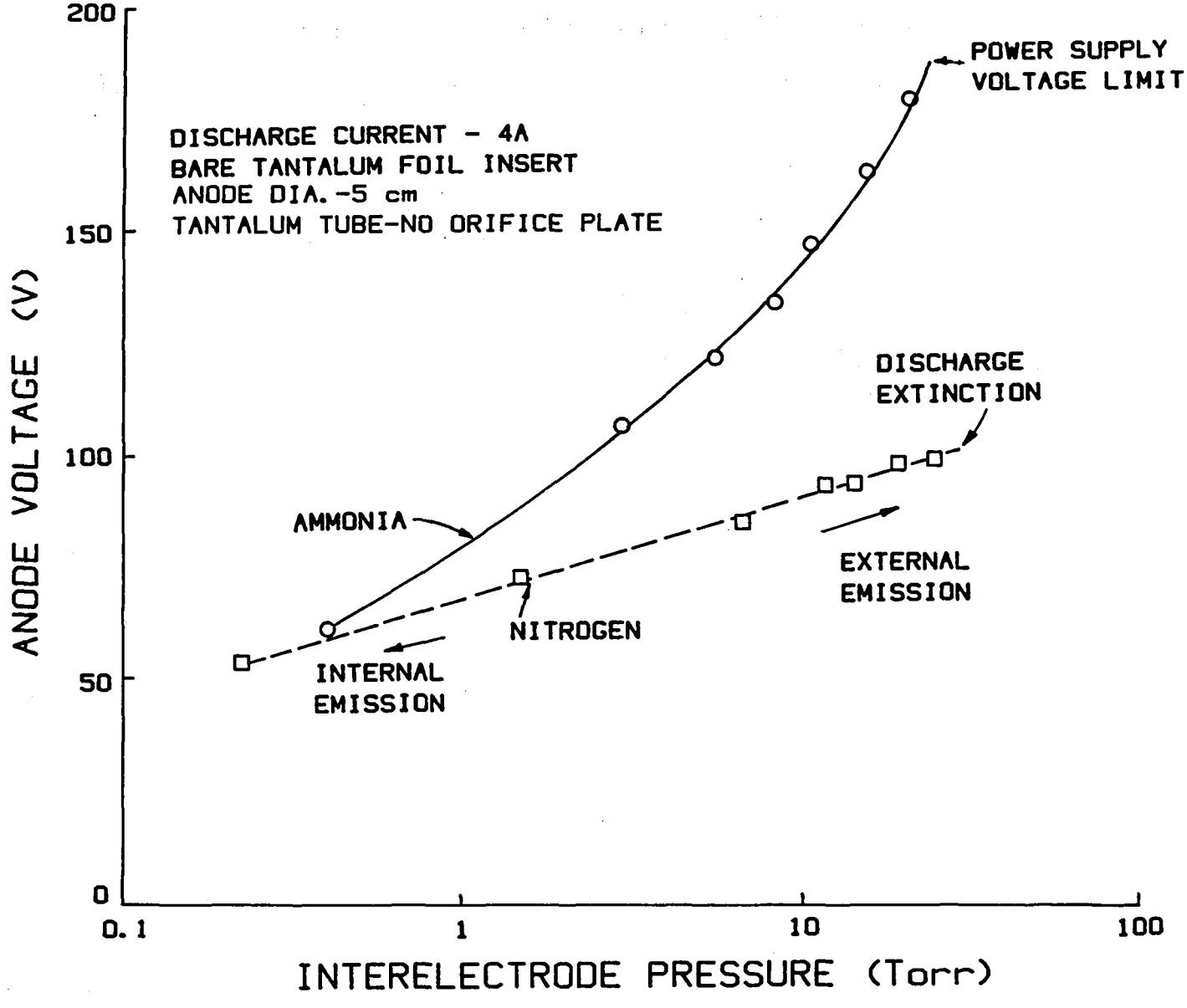

Fig. 38 Comparison of Nitrogen and Ammonia Characteristics - Bare Foil Insert

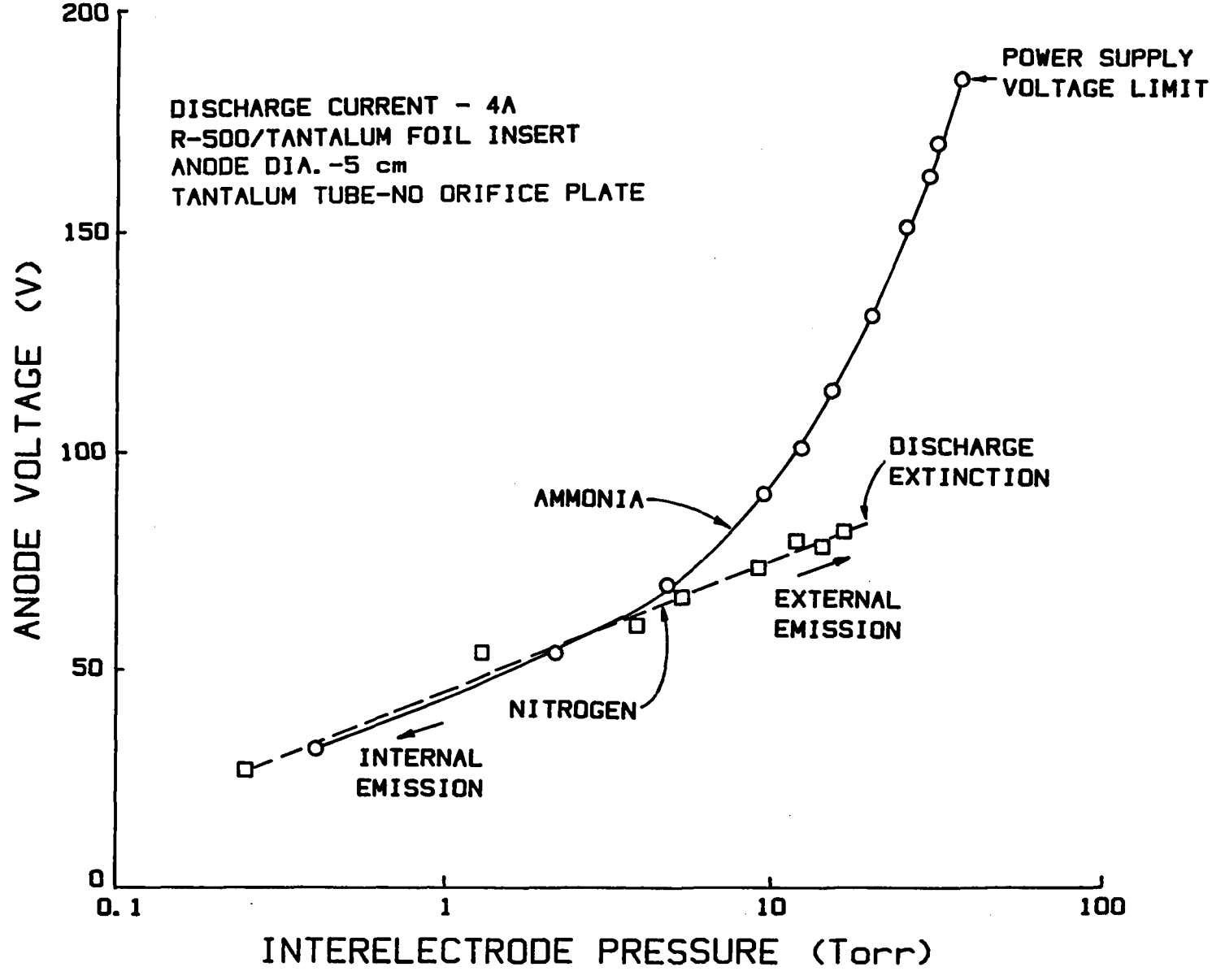

Fig. 39 Comparison of Nitrogen and Ammonia Characteristics - R-500 Foil Insert

pressures. The power supply voltage limit was reached at 45 Torr with ammonia expellant, and the discharge extinction point was reached at 30 Torr with nitrogen.

With an untreated tantalum foil insert the anode voltage required to sustain the 4 A discharge was roughly twice that required with the impregnated tungsten insert, as shown by the data in Fig. 38. At 22 Torr the power supply voltage limit was reached using ammonia, whereas the discharge extinguished at pressures around 40 Torr with nitrogen expellant. When the tantalum foil was treated with R-500, the anode voltage versus pressure characteristics, shown in Fig. 39, were nearly equivalent to those exhibited by the sintered tungsten insert. This indicates that the addition of a low work function material to the insert is important if the voltage that must be applied to the anode to maintain the discharge current is to be relatively low.

Plasma Potential Profiles

An emissive probe was used to determine the plasma potential as functions of pressure and axial position downstream from the end of the cathode at some operating conditions. Figure 40 is a typical plot of the plasma potential at different locations as a function of pressure. From bottom to top, respectively, the curves indicate the plasma potential at locations 1, 2, and 3 designated in Fig. 33 and the anode voltage. Thus at a given pressure the vertical distance between the x axis and the curve corresponding to location 1 represents the cathode fall; the vertical distance between the curves corresponding to locations 1 and 3 represent the bulk plasma voltage drop; and the vertical distance between the curves corresponding to location 3 and the anode voltage represents the anode fall. Although variations with pressure do exist, the plasma potential at the cathode exit seems to hover around 10 volts, while the

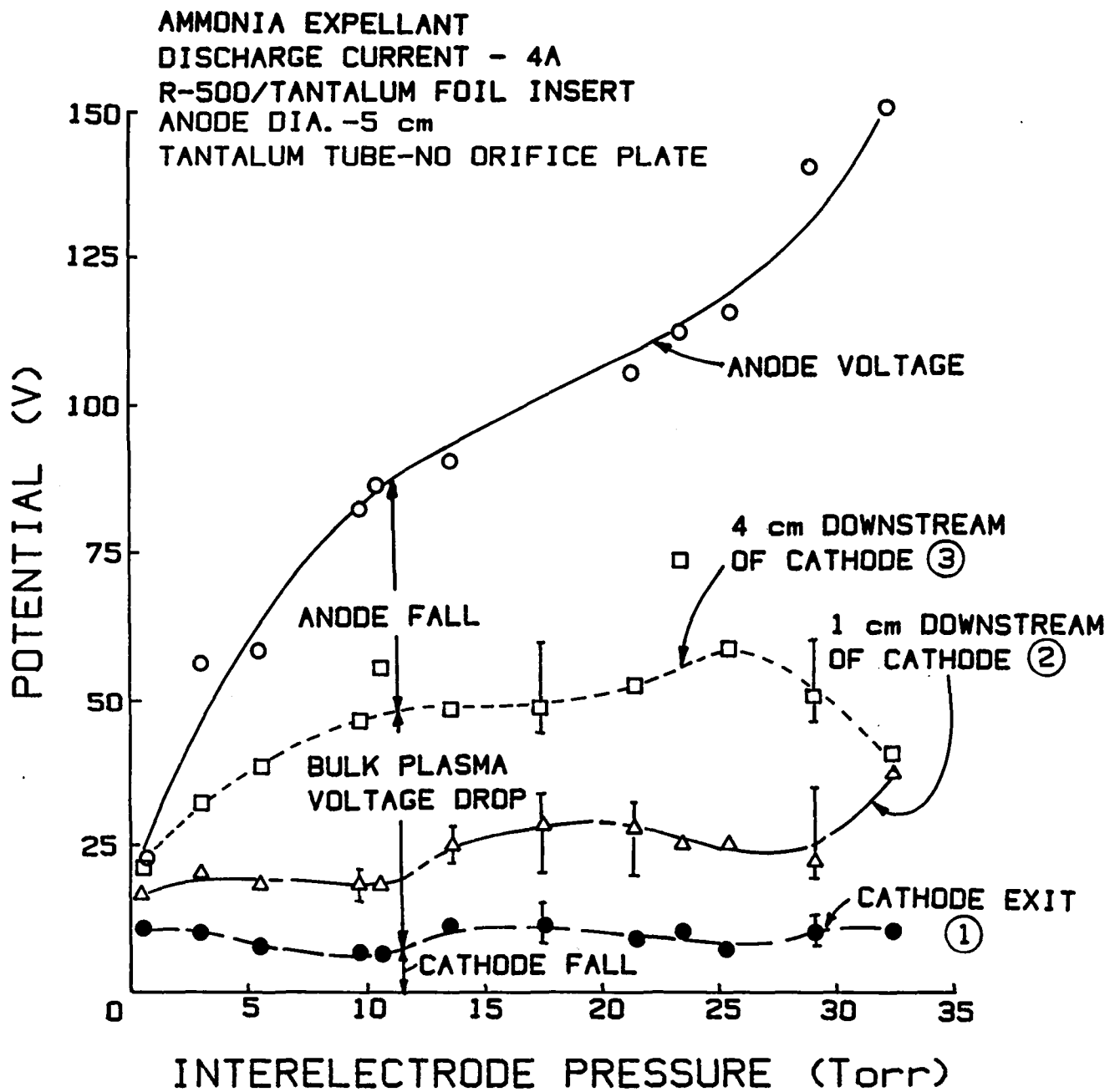

Fig. 40 Effect of Interelectrode Pressure on Potential Drops

anode voltage increases steadily with pressure. Hence, the anode fall increases with pressure at the operating conditions indicated, while the cathode fall appears to remain roughly constant. At pressures above 25 Torr the data suggest the plasma potential at location 3 begins to decrease with increasing pressure. This is somewhat misleading because equipotential maps show the plasma potential at locatiion 3 is not representative of the potential near the anode surface at pressures above about 25 Torr. Figure 41 presents the same data as Fig. 40, but shows the plasma potential as a function of position at different pressures. Figure 41 shows that, as pressure increases, an increasing portion of the cathode-to-anode voltage drop occurs near the anode. It would be most desirable to have the anode and cathode falls remain small so the bulk plasma voltage drop would be large and so uniform heating of expellant in the region between the cathode and the anode would occur.

At the higher pressures (> 10 Torr) the intensiy of the glow of the hot emissive probe filament was observed to be greatly diminished. This could be a result of increased convective heat transfer from the filament, and/or optical scattering of the photons by the expellant after emission. The measurement of plasma potentials at higher pressures was difficult because plasma potential tended to fluctuate with a period of the order at a few seconds and an amplitude of several volts (a few percent of the ~140 v anode potential). These fluctuations seem to result from a natural convection flow pattern that develops in the hot fluid above the cathode and anode at higher pressures. From visual observation it appears that the heated gas near the cathode rises and travels to the edge of the anode above the cathode, where it mixes with cooler gas and is recyled back to the cathode. In addition, the probe seemed to cause perturbations in the plasma at higher pressures, which may result in a plasma potential value that deviates from the true value.

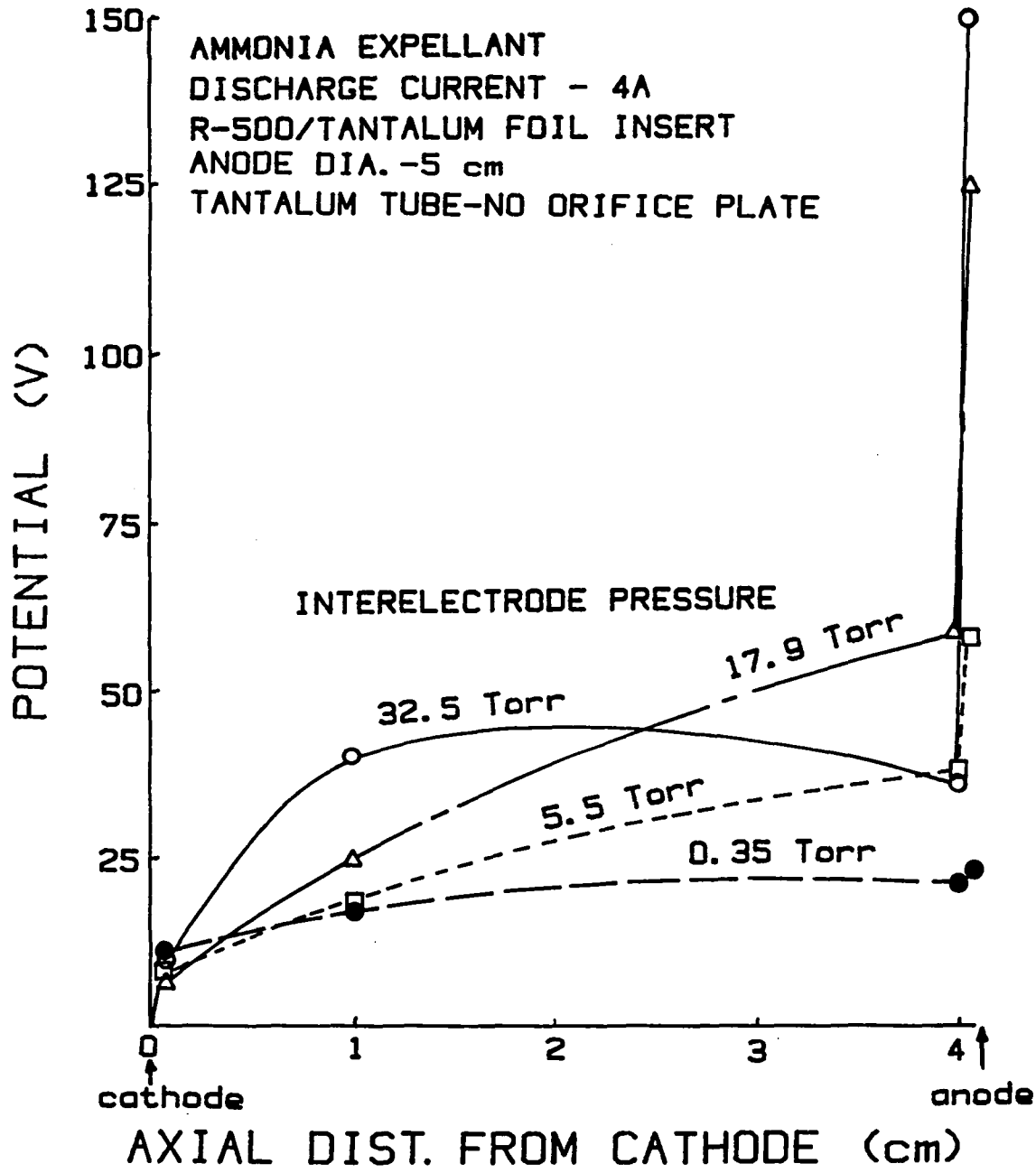

Fig. 41 Potential Profiles in Ammonia Discharges

In all the above tests a stable, uniform glow discharge was observed at low pressures with ammonia expellant, as shown in Fig. 42a. At these conditions the cathode fall and the bulk plasma voltage drop are nearly equal and the anode fall is negligible (refer to Fig. 40). As the interelectrode pressure was increased to about 0.5 Torr, a blister-shaped luminous sheath appeared on the inner surface of the anode at the edge nearest the cathode, as shown in Fig. 42b. Further increases in pressure caused the blister sheaths to multiply in number while decreasing in size. It is noted that it is atomic de-excitation that makes the blister sheaths visible. The excitation reaction that preceeds de-excitation is probably caused by electrons that have been accelerated through a significant potential difference near the regions where de-excitation is occurring. This in turn suggests a significant voltage rise and hence strong electric field exists at the blister sheaths.

Figure 42c shows the blister sheath formation at a pressure of 0.7 Torr where the cathode fall and the bulk plasma voltage drop are still nearly equal in magnitude, while the anode fall is quite small. At a pressure of 2.8 Torr there appear to be three rows of blister sheaths as seen in Fig. 42d. Moving downstream from the cathode the number of blister sheaths per row decreases. Also, each blister sheath appears to line up adjacent to a gap between the blister sheaths in the next row. At this pressure the magnitude of the bulk plasma drop is roughly equal to twice the cathode fall and the anode fall is becoming larger than the cathode fall. As the pressure increased further the blister sheaths seemed to merge together, forming sheath lines as shown in Fig. 42e. At a pressure of 8.0 Torr the magnitude of the anode fall is slightly less than that of the bulk plasma voltage drop, and the cathode fall is relatively small. At 13.1 Torr a continuous sheath plane formed around the interior of the anode, as illustrated in Fig. 42f. Here the anode fall is roughly equal to the bulk

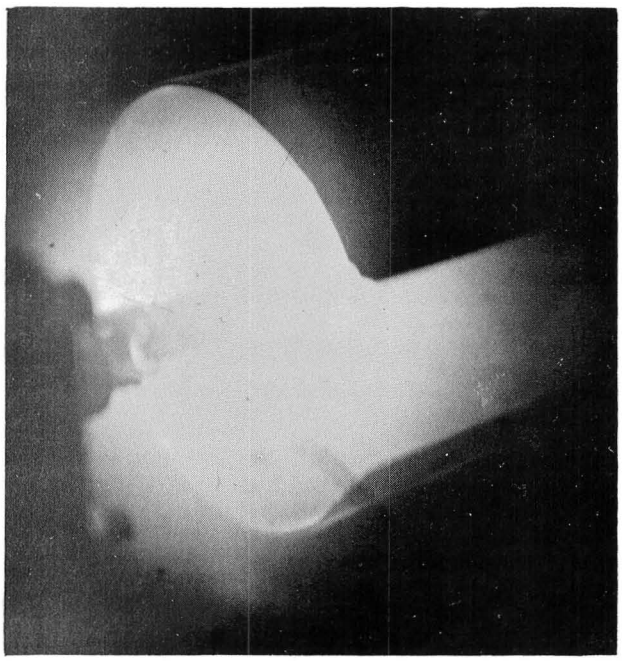

a) 0.25 Torr

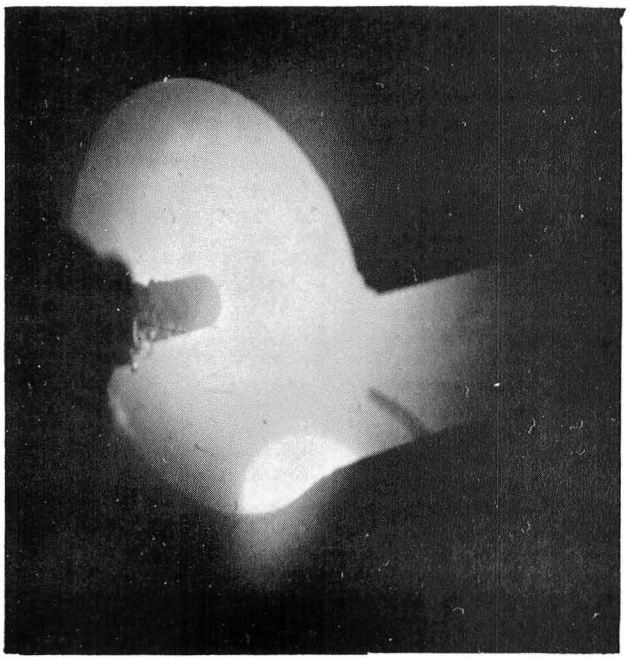

b) 0.5 Torr

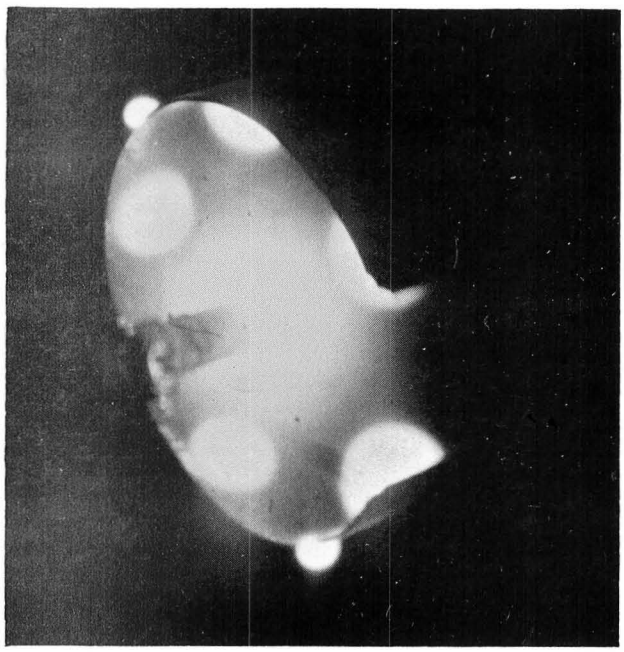

c) 0.7 Torr

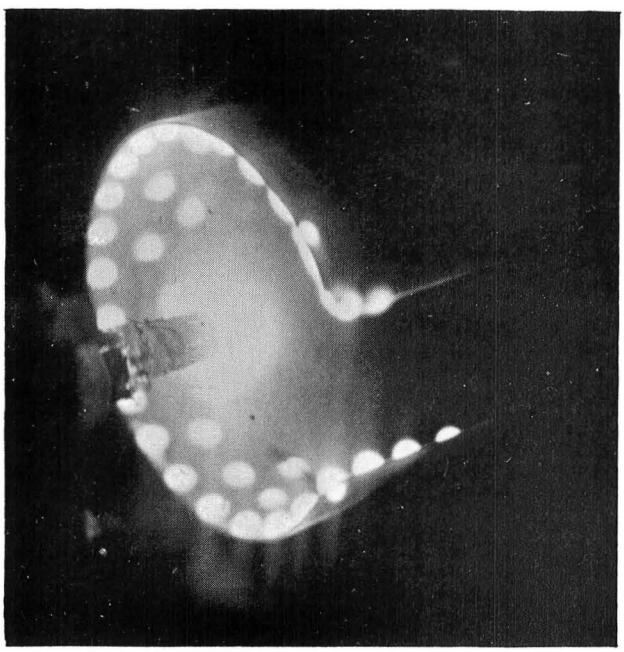

d) 2.8 Torr

Fig. 42 Effect of Interelectrode Pressure on the Appearance of an Ammonia Hollow Cathode Discharge

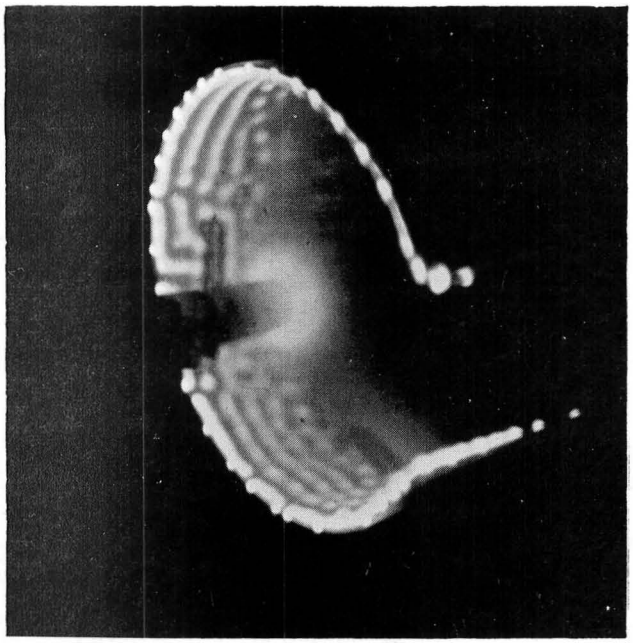

e) 8 Torr

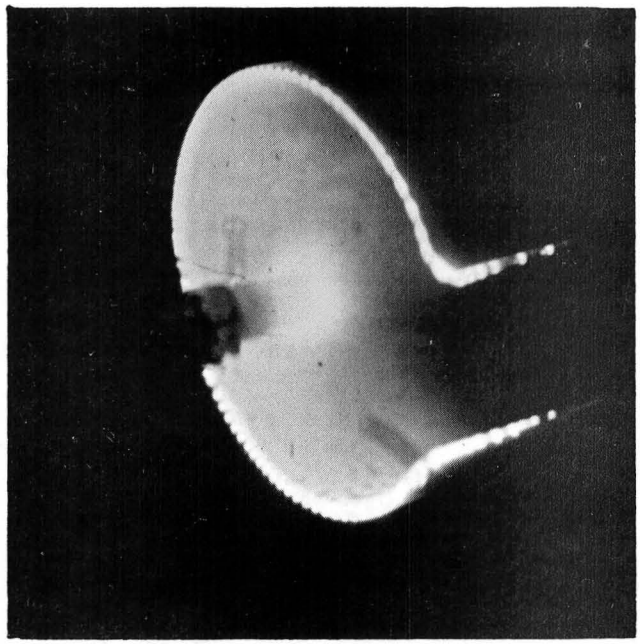

f) 13.1 Torr

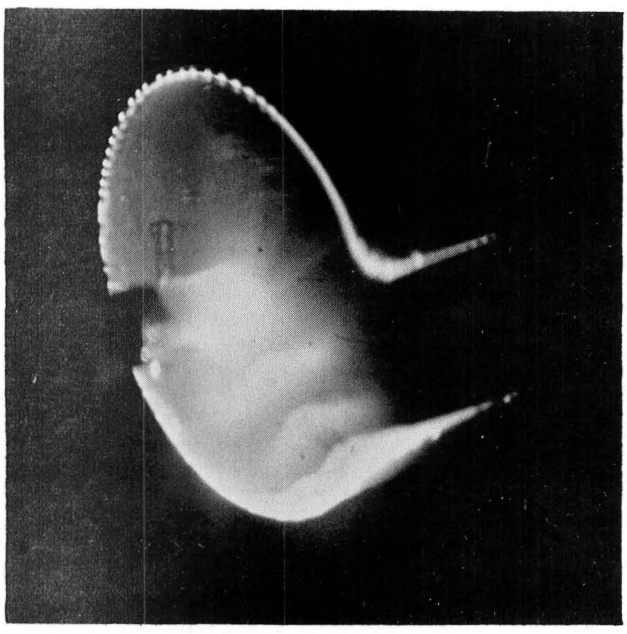

g) 15.7 Torr

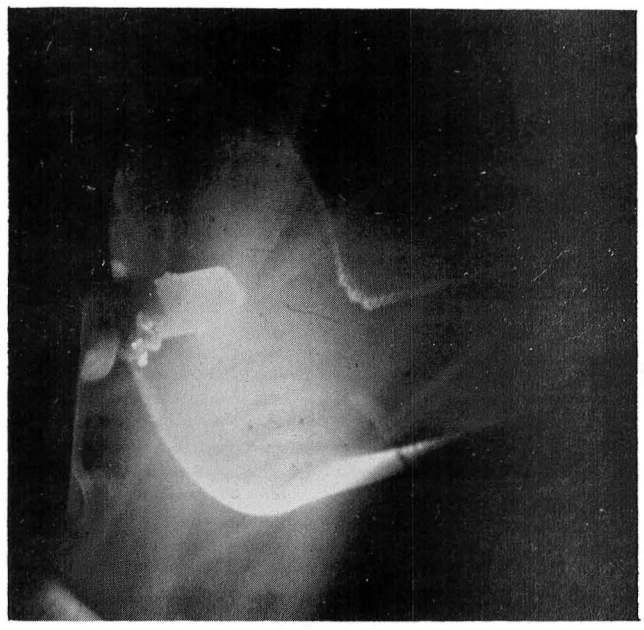

h) 39 Torr

Fig. 42 (cont.) Effect of Interelectrode Pressure on the Appearance of an Ammonia Hollow Cathode Discharge

plasma voltage drop, while the cathode fall is still quite small. Further increases in pressure caused the formation of several layers of sheath planes as shown in Fig. 42g for a pressure of 15.7 Torr. The number of sheath planes increased with pressure and the planes appeared to be equally spaced on the lower surface of the anode. Several planes are shown at a pressure of 39 Torr in Fig. 42h. As the pressure approached 40 Torr an increasingly luminous discharge was observed until the power supply voltage limit was reached. At these higher pressures the cathode fall is still relatively small, while the anode fall is very large compared to the bulk plasma voltage drop.

Assuming the ion density to be proportional to the pressure, the Debye length can be shown theoretically to vary as the square root of the reciprocal of the pressure, for a given electron temperature. The diameter of the blister sheaths, as measured from the photographs, also appears to follow this relationship. This suggests that the blister sheath diameter may be related to the Debye length, although complete verification would require values of the neutral and plasma densities and the electron temperature, which were not measured in these tests. It should be noted that the blister sheath phenomena was observed only with ammonia expellant. The sequence of photographs in Fig. 42 also show the luminous region at the hollow cathode changing as pressure was increased. At the lowest pressure of 0.25 Torr (Fig. 42a) this cathode plume was quite large and uniform, but as the pressure increased, its diameter decreased and then it became asymmetric at pressures above about 10 Torr. As pointed out previously (Ref. 19 and pg. 81) electron emission occurs from a spot on the cathode tube rather than from the insert at these higher pressures.

Evacuated, Conducting Cathode Studies

The major obstacle to proper hollow cathode operation in the arc jet regime appears to be the formation of the intense emission spot on the cathode tube that is observed at higher pressures. Because the size of the insert emission region decreases with increasing pressure, it was postulated that evacuating the hollow cathode would cause the emission region size to increase thus inhibiting the formation of a tiny emission spot. Hence, a vacuum line was connected to the cathode, and the expellant was fed directly into the bell jar using the test configuration illustrated in Fig. 31. Initial tests showed, however, that the emission spot moved to the outside of the metallic cathode tube or orifice plate edge at high interelectrode pressures whether or not a vacuum was drawn on the cathode. Further this behavior was observed on both open-ended and orificed hollow cathodes. This appears to occur because the resistance to current flow from the outside of the tube to the anode is less than that from the insert to the anode. Evacuating an open-ended, tantalum hollow cathode also had little effect on the anode voltage versus pressure plot as Fig. 43 shows. The movement of the emission spot from inside to outside the cathode associated with the data of Fig. 43 occurred quite gradually. At a pressure of about 20 Torr, however, the transition to external spot emission from the cathode tube was consistently observed to have occurred. Above about 40 Torr the power supply voltage limit was reached and the effects of further increases in interelectrode pressure could not be examined.

Anode voltage versus pressure charcteristics for a tantalum orificed cathode having a 0.89 mm diameter orifice are shown in Fig. 44. In this case the discharge again appeared to behave the same whether or not the cathode was evacuated. With an orifice present the transition from internal insert emission to external spot emission was observed visually to occur quite abruptly,

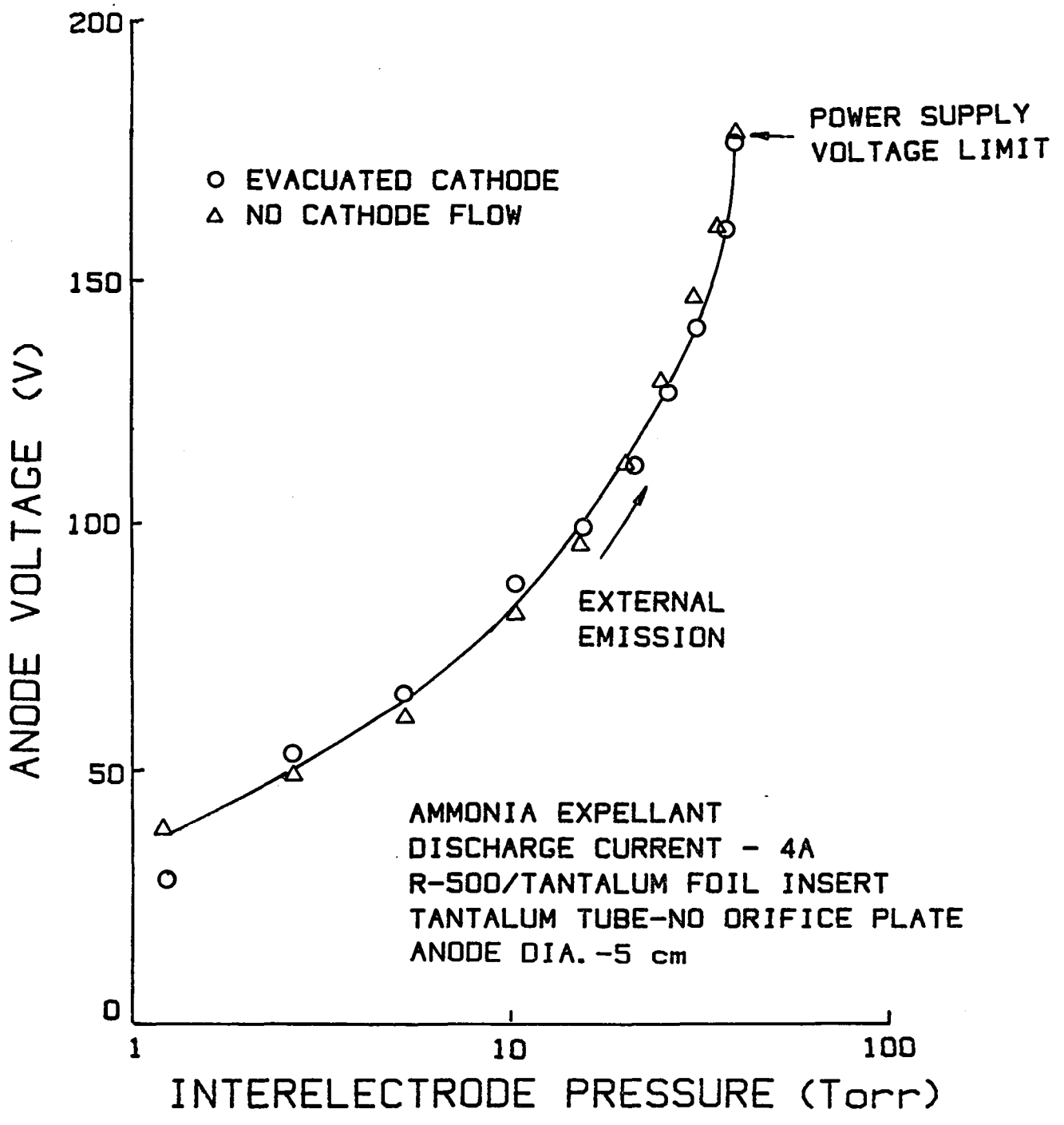

Fig. 43 Effect of Evacuation for Open-ended Cathode

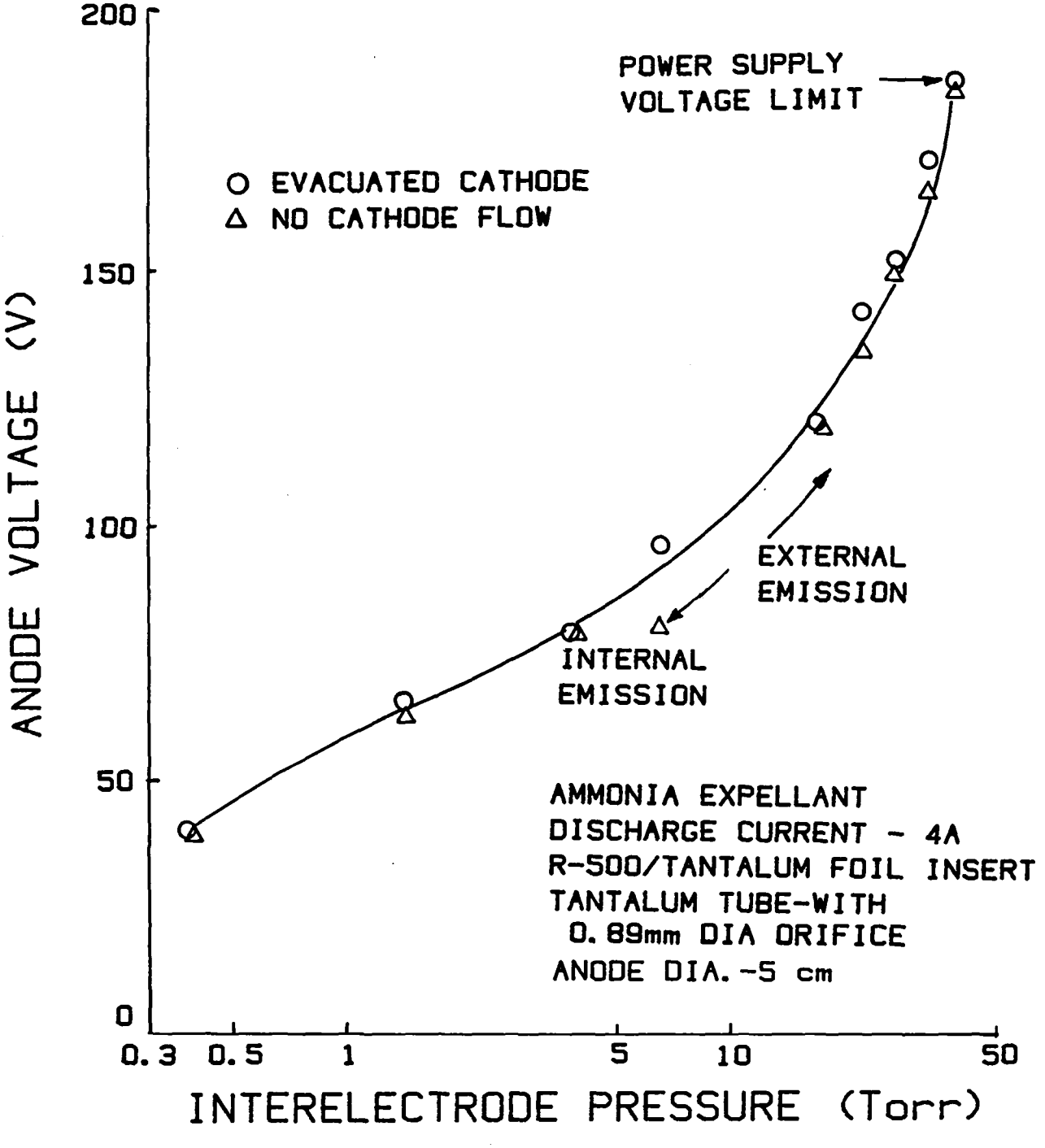

Fig. 44 Effect of Evacuation for Orificed Hollow Cathode

however, at around 12 Torr. The anode voltage at a given pressure was found to be ten to twenty volts higher for an orificed cathode than for an open-ended one. This voltage drop is small and it may not be significant, but it suggests that the orifice plate increase the insert-to-anode electrical resistance and this may in turn explain why the transition to external spot emission occurs at a somewhat lower pressure with an orificed cathode than with an open-ended one. A few tests were also run using a smaller (0.46 mm) diameter orifice on the cathode. Unfortunately, the voltmeter was damaged during these tests and no voltage versus pressure data were recorded. It was observed, however, that the transition from internal to external cathode discharge occurred at around 10 Torr with and without a vacuum being drawn on this cathode.

Evacuated, Non-conducting Cathode Studies

In an effort to prevent the transition to external electron emission from the cathode tube a non-conducting cathode tube containing an R-500 coated tantalum foil insert was substituted for the metallic cathode tube. The insert was connected electrically to the discharge power supply so emission was forced to come from the insert. Initial tests of the non-conducting cathode tube used an open-ended quartz tube; because this tube was transparent the red-hot emission region on the insert could be seen during operation. As interelectrode and internal cathode pressure were increased, the emission region was observed to decrease in size. When a vacuum was drawn on the cathode operating at a high pressure, the length of the emission region on the insert was observed to increase. At still higher interelectrode pressures, however, the evacuation was insufficient to mainain a low pressure inside the tube and the emission spot remained on the end of the insert. Unfortunately, the discharge at higher interelectrode pressures caused the quartz cathode to melt partially.

In order to prevent tube melting the quartz tube was replaced with an open-ended alumina tube that could withstand higher temperatures. Figure 45 shows the voltage versus pressure characteristics of this hollow cathode. The 5 cm anode data of Fig. 45, when compared with similar data for the tantalum tube cathode (Fig. 43), show the change to the alumina tube causes the anode voltage level to increase slightly (~10 volts). Also shown in Fig. 45 are data collected with a 1.7 cm dia. anode in place of the 5 cm one which has been used in all of the previously described experiments. The switch to the smaller anode was investigated in an effort to realize lower voltage drops so the voltage limitation imposed on the testing by the discharge power supply could be avoided. The data of Fig. 45 suggest that this change had the desired effect: using the smaller anode the voltage required to sustain the 4 A discharge was only half of that for the 5 cm anode. Unfortunately, emissive probe data obtained with this anode (Fig. 46) indicate the bulk plasma voltage drop is still small compared to the cathode and anode falls, so the plasma heating efficiency would be expected to be poor. Also the anode and cathode appeared to be much hotter when the small anode was used. With the 1.7 cm dia. anode, the alumina cathode began to melt at pressures above 50 Torr, whereas the power supply voltage limit was reached at 40 Torr with the 5 cm anode. The smaller anode does therefore serve a useful purpose in conducting tests with the available 5 A, 180 V power supply.

In postulating that the plasma heating efficiency would be poor in a device that used a smaller diameter anode an assumption was made regarding the data of Fig. 46. Namely, it was assumed that the plasma potential 3 cm downstream of the cathode exit would be roughly equal to the potential near the anode. A complete plasma potential map has not been obtained to verify that the potential there is close to the potential at the edge of the anode sheath. This assumption may introduce a few volts error, but if one accepts this the bulk plasma

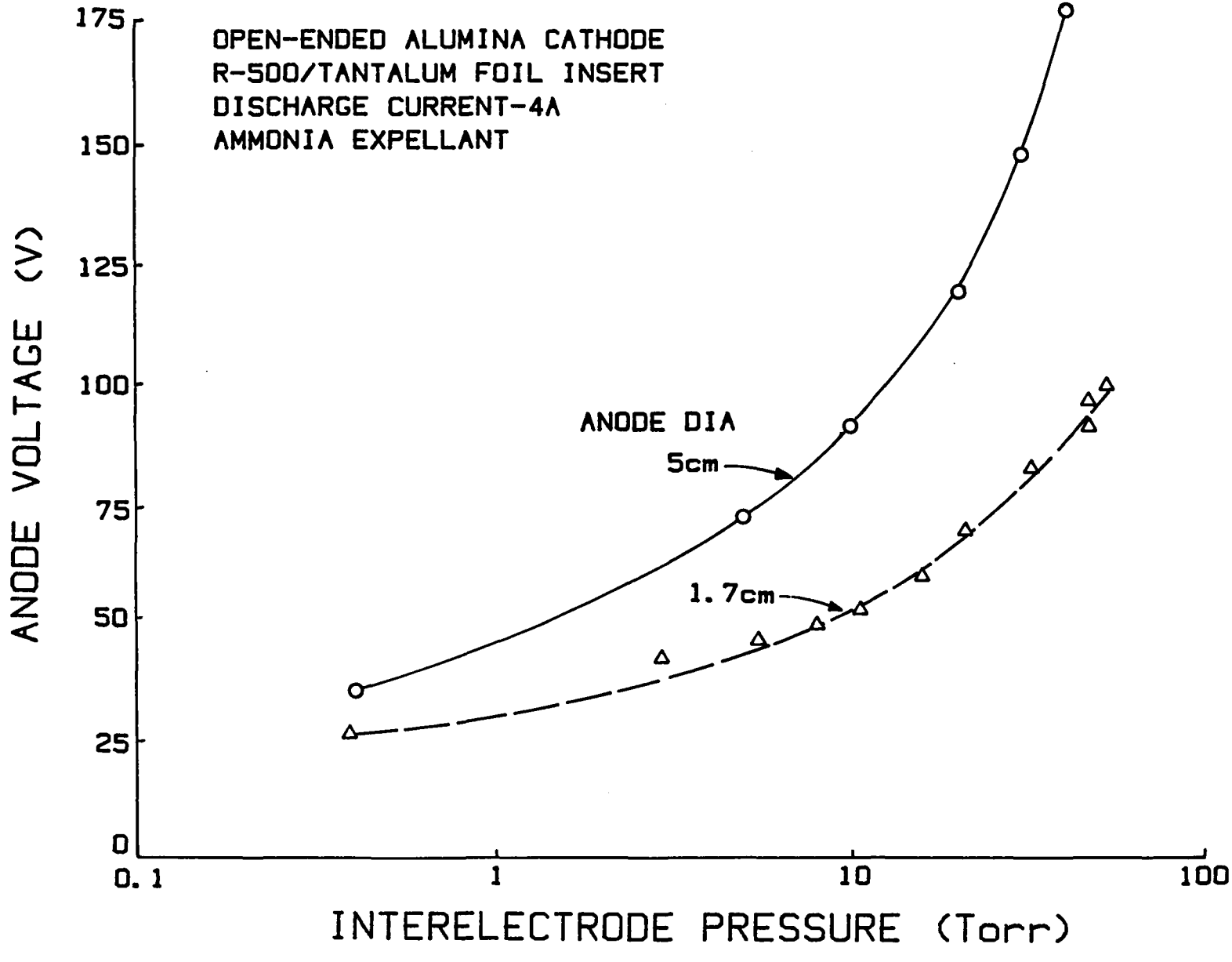

Fig. 45 Alumina Cathode Tube Voltage/Pressure Characteristics

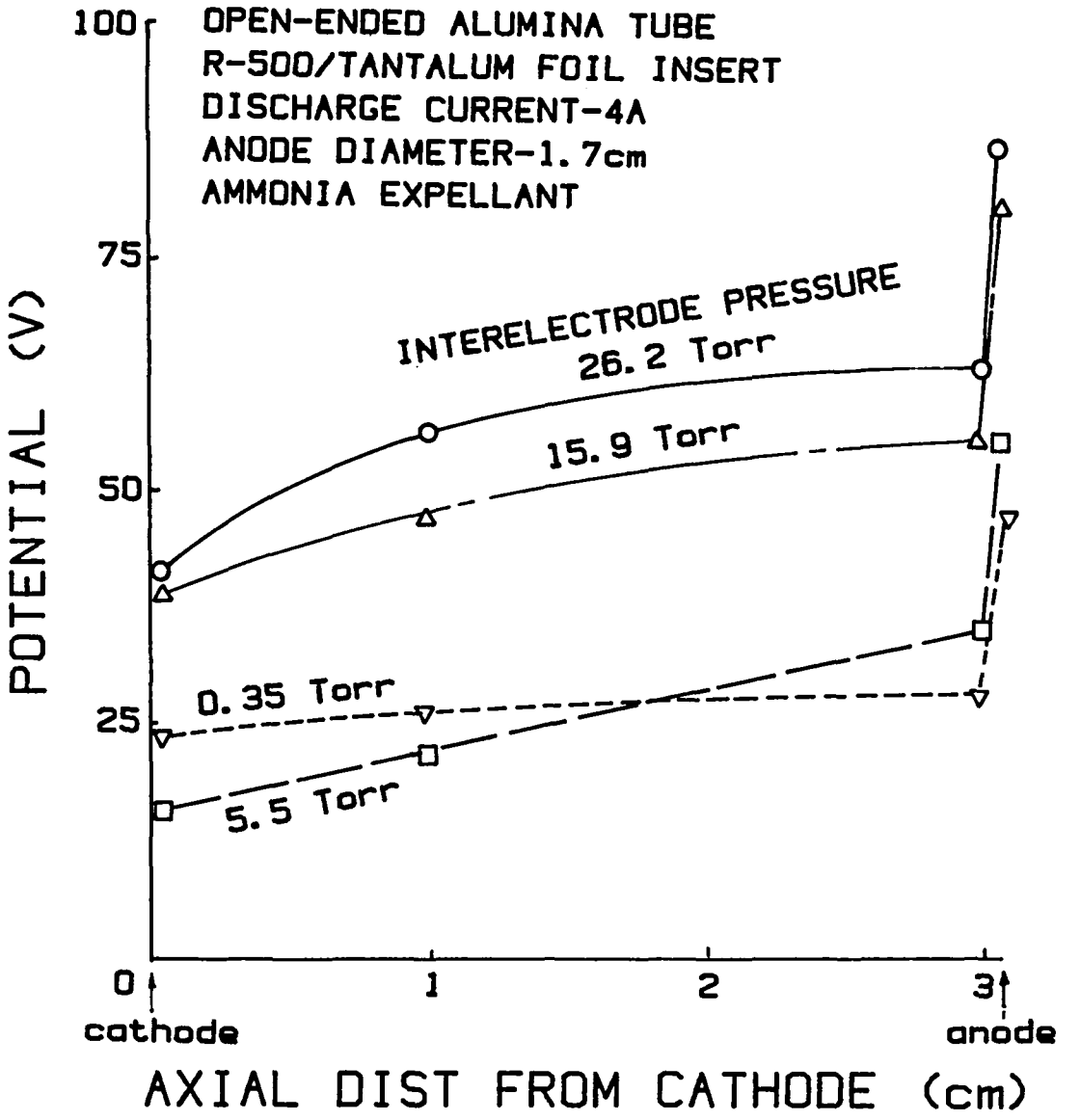

Fig. 46 Plasma Potential Profile for Alumina Hollow Cathode When Operating with a 1.7 cm Diameter Anode

voltage drop can be taken as the difference between the plasma potential 3 cm downstream and the plasma potential at the cathode exit. This leads to the conclusion that poor plasma heating efficiency is expected with the 1.7 cm anode.

In order to maintain a lower pressure in the emission region of the cathode an alumina orifice plate with 1.5 mm orifice diameter was cemented to an alumina cathode tube and tested with an R-500 treated tantalum foil insert. The anode voltage versus interelectrode pressure curve that was measured is shown in Fig. 47 to be about the same as the one for the open-ended tube. The red hot emission region of the insert appeared to stay relatively large (about 1 - 2 mm long) with the orifice plate installed when the cathode was being evacuated. On the other hand, isolating the cathode from the vacuum pump would cause the emission region to shrink to a line around the downstream edge of the insert. Unfortunately the alumina orifice began to melt at pressures above 30 Torr. This occurred because alumina has a low thermal conductivity and heat from the high pressure discharge could not be dissipated rapidly enough to keep the cathode temperature below the melting point of the alumina.

Conclusions

The following conclusions are drawn based on the work just described.

1. The anode voltage is independent of expellant flow rate through the cathode.

2. Over the range tested the discharge current has a relatively small effect on the anode voltage, and the plasma exhibits negative resistance behavior as discharge current is varied.

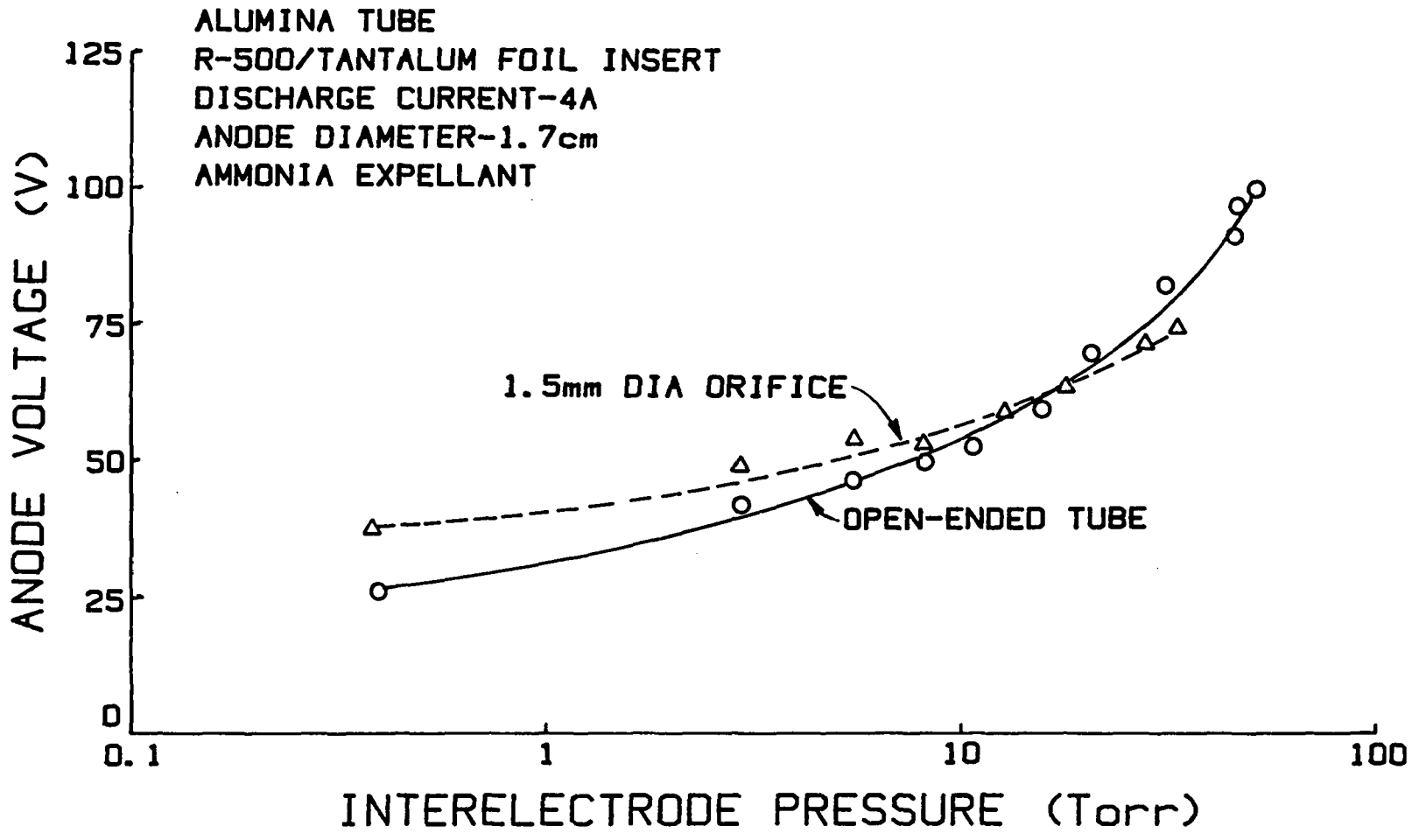

Fig. 47 Effect of an Orifice Plate on the Performance of an Alumina Hollow Cathode

3. Ammonia, which is an expellant of interest, yields a discharge that operates at higher anode voltages than nitrogen does, but the nitrogen discharge is more stable.

4. Inserts treated with a low work function material such as barium aluminate, lanthanum hexaboride, or R-500 can be operated successfully on ammonia. These materials would be expected to facilitate efficient arc jet operation (i.e., operation without excessive power consumption for cathode operation).

5. The anode fall, which is typically quite large for ammonia expellant at high pressures, appears to induce the formation of blister-shaped, luminous sheaths on the anode. The plasma heating efficiency could be improved if more of this voltage drop could be transferred from these sheaths to the bulk plasma.

6. A major obstacle to hollow cathode operation in the arc jet regime is the tendency for an external spot discharge to develop on the cathode tube at higher pressures. For this reason hollow cathodes made of metal or other electrical conductors do not appear to be suitable candidates for arc jet applications.

7. When cathode tubes are made of non-conducting materials like quartz or alumina the electron emission can be forced to come from an insert within the tube. If the tube has an orifice plate and it is evacuated, diffuse electron emission occurs and the insert need not overheat. At high power levels the quartz or alumina tubes or orifice plates may melt.

8. At higher interelectrode pressures plasma potentials are difficult to measure because induced convective flow and intense heat release which cause voltage fluctuations and emissive probe overheating. It is believed that this condition could be improved if forced convection were applied in the interelectrode region.

Recommendations

1. Tests should be conducted on boron nitride hollow cathodes.

2. Data should be collected on the interior cathode pressure as well as the interelectrode pressure during subsequent tests.

3. New cathode geometries including some which involve flow through the interelectrode region should be investigated.

4. The effect of anode size and geometry should be further investigated, in an effort to decrease the anode fall.

5. A power supply with a higher voltage range should be incorporated so the tests can be conducted at higher pressures.

6. The effect of pressure increases on the insert emission length should be more closely studied.

MERCURY DISCHARGE CHAMBER PERFORMANCE MODEL

The discharge chamber model proposed by Brophy[2] has been tested against experimental results obtained using inert gas propellants. It is also of interest to investigate the suitability of the model for other propellants such as mercury. The purpose of this paper is to develop the input data needed to apply the model to a mercury discharge chamber, to apply the model and then to compare its predictions to plasma property and performance measurements that have been made in the Hughes Research Laboratory Ring Cusp Thruster.[21] The model will also be used to estimate the effect of removing the J-series mercury thruster baffle on the performance of this thruster. It is noteworthy the model has not been verified experimentally for divergent field thrusters like the J-series thruster and many assumptions must be made to effect this analysis. The predictions of this analysis must therefore be considered very preliminary. Data describing this thruster will be drawn from Ref. 22.

Theoretical Development

In order to apply the discharge chamber model,[2] cross section data describing the electron-induced excitation of mercury from the ground state to any excited state (the so-called lumped excitation cross section data) are needed. The data used in this analysis, which were developed from Rockwood's results,[23] are shown in Fig. 48. An energy loss associated with lumped excitation is also needed and in this case the threshold energy associated with mercury's first excited state (U_{ex} = 4.5 eV) has been used in accordance with the suggestion of Dugan and Sovie.[24] Figure 48 also shows the ionization cross section data obtained from Rockwood[23] that will be needed for the analysis. The data of Fig. 48 have also been multiplied by electron velocity and integrated over the Maxwell Boltzmann distribution function to obtain excitation ($\langle\sigma_{ex}v_e\rangle$) and ionization ($\langle\sigma_{+}v_e\rangle$) rate factors that describe Maxwellian electron/mercury

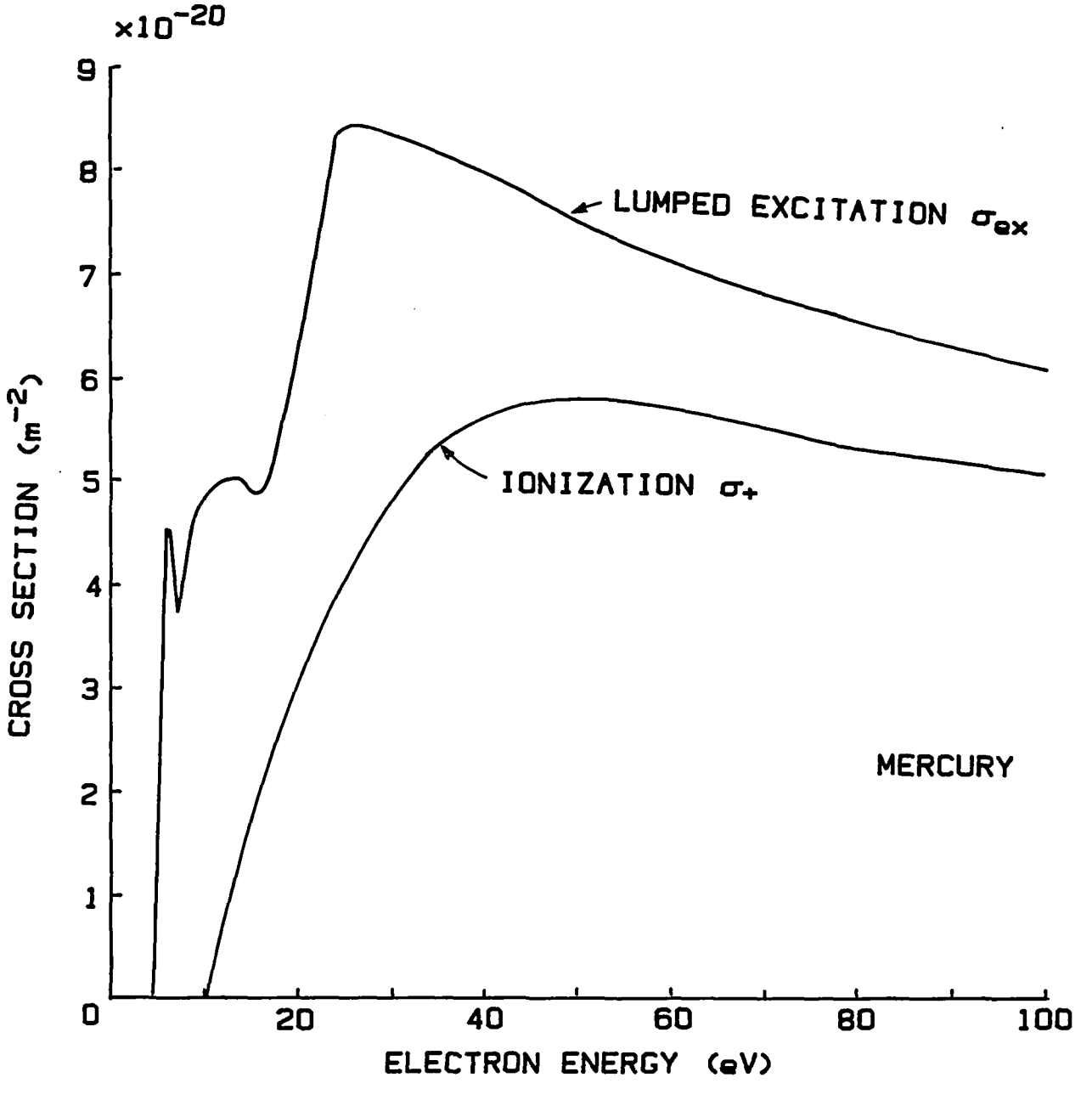

Fig. 48 Electron-Mercury Atom Cross Section Data

reactions. These rate factors are plotted against Maxwellian electron temperature in Fig. 49.

Using the data of Figs. 48 and 49 the baseline plasma ion energy cost for a mercury discharge may be obtained by solving the following equations[2] simultaneously:

$$\varepsilon_p^* = \frac{V_D\,(\sigma'_{ex} + \sigma'_+)/\sigma'_+}{1 + \dfrac{n_M \langle \sigma_+ v_e \rangle_M}{n_p\, \sigma'_+\, v_p}} \tag{7}$$

$$\varepsilon_p^* = \frac{U_+ + \varepsilon_M + \dfrac{\left[\dfrac{n_p}{n_M}\,\sigma'_{ex}\, v_p + \langle \sigma_{ex}\, v_e \rangle_M\right] U_{ex}}{\dfrac{n_p}{n_M}\,\sigma'_+\, v_p + \langle \sigma_+ v_e \rangle_M}}{1 - (V_c + \varepsilon_M)/V_D} \tag{8}$$

In these equations U_+, the ionization energy, is 10.44 eV for mercury, n_p/n_M is the primary-to-Maxwellian electron density ratio, v_p is the primary electron velocity, V_c is the potential at which electrons are supplied to the discharge from the cathode (i.e., the electron source potential), V_D is the discharge voltage, ε_M is the average energy lost to the anode by the Maxwellian electrons collected there, the prime indicates cross section evaluation at the primary electron energy (assumed to be equal to V_D-V_c) and the other quantities have been defined previously. It should be noted that the effect of keeper discharge power has been neglected in this analysis. It is assumed that none of this power goes into producing ions that find their way to the main discharge chamber and that this power is also small compared to the main discharge power. This assumption is consistent with Rawlin's observation that discharge chamber performance is not affected significantly by variations in keeper power.[25]

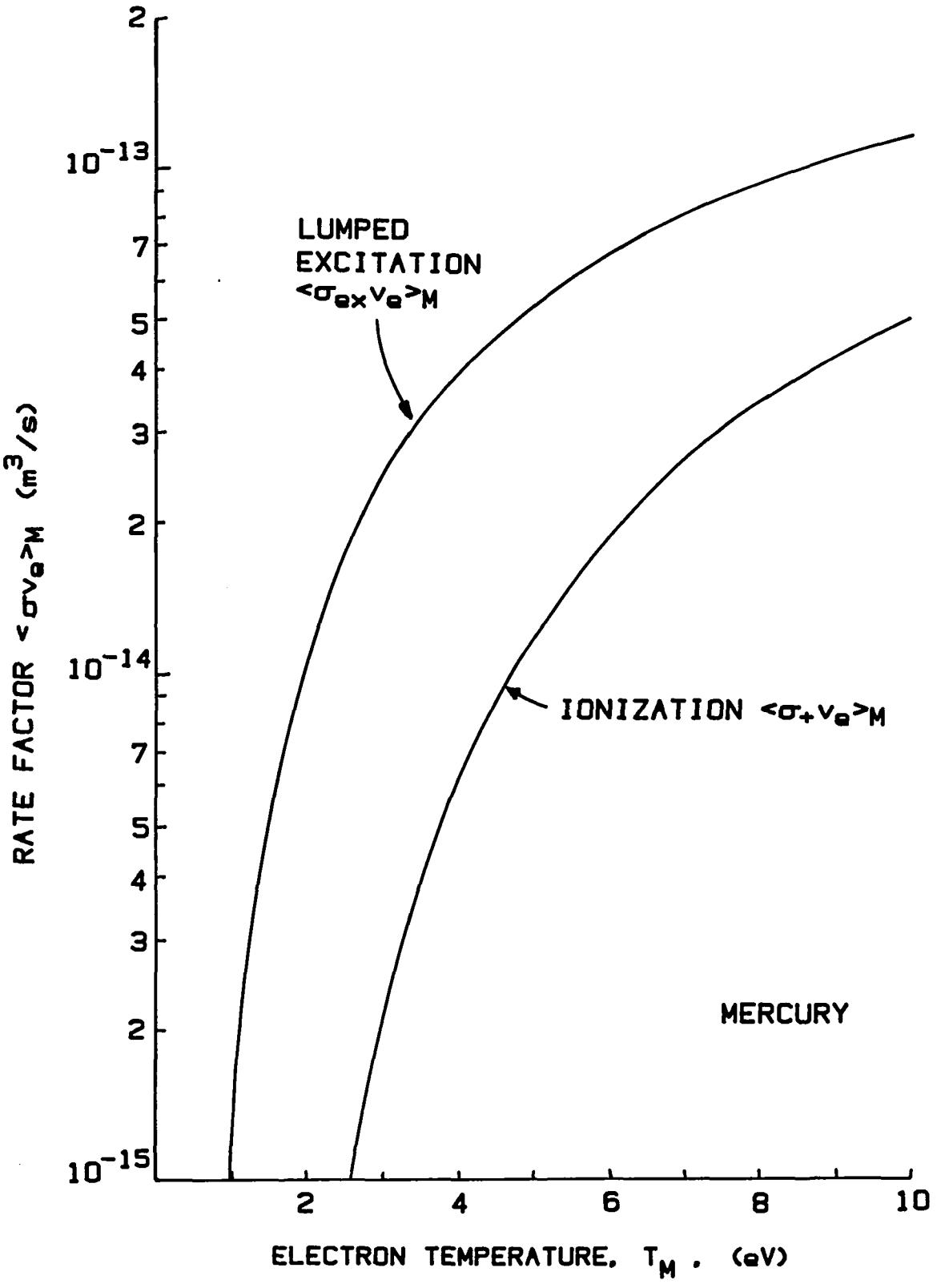

Fig. 49 Maxwellian Electron-Mercury Atom Rate Factor Data

An expression for the average energy lost by Maxwellian electrons going to the anode has been determined for argon and xenon[2] but such an expression has not been developed for mercury. For this analysis it has been postulated that this energy is equal to the Maxwellian electron temperature, i.e.,

$$\varepsilon_M = T_M. \tag{9}$$

This rather arbitrary selection is based on the observations that the plasma potential appears to be close to anode potential in the mercury thrusters of interest[22] and elastic electron-mercury atom collision cross sections are higher for mercury than they are for argon or xenon.[26] This last obseration bears on the selection because it implies the energy carried to the anode by Maxwellian electrons would be less for mercury than the values given for xenon by the experimentally determined equation[2] $\varepsilon_M = \frac{4}{3} T_M + 2$.

Using the data of Figs. 48 and 49 in Eq. 7 the curves like those shown in Fig. 50 that join near 90 eV at low electron temperatures are obtained at the parametric values of primary-to-Maxwellian electron density ratio indicated on the figure. As the legend of Fig. 50 suggests these results were obtained at an electron source potential (V_c) of 4v. Parametric solution of Eqs. 8 and 9 in terms of the primary-to-Maxwellian electron density ratio yields the other set of curves in Fig. 50 for this case where V_c = 4v. The intersections of the two sets of curves corresponding to the common values of n_p/n_M, which are identified by the circles, in Fig. 50, represent the actual solutions. Hence the true solution is a line joining the circles that have been plotted. Using Fig. 50 one observes that a mercury plasma with 5 eV Maxwellian electrons and 28 eV primary electrons ($V_D - V_c$ = 28v) would, for example, have a baseline plasma ion energy cost (ε_p^*) of 43 eV. Note also that the primary-to-Maxwellian electron

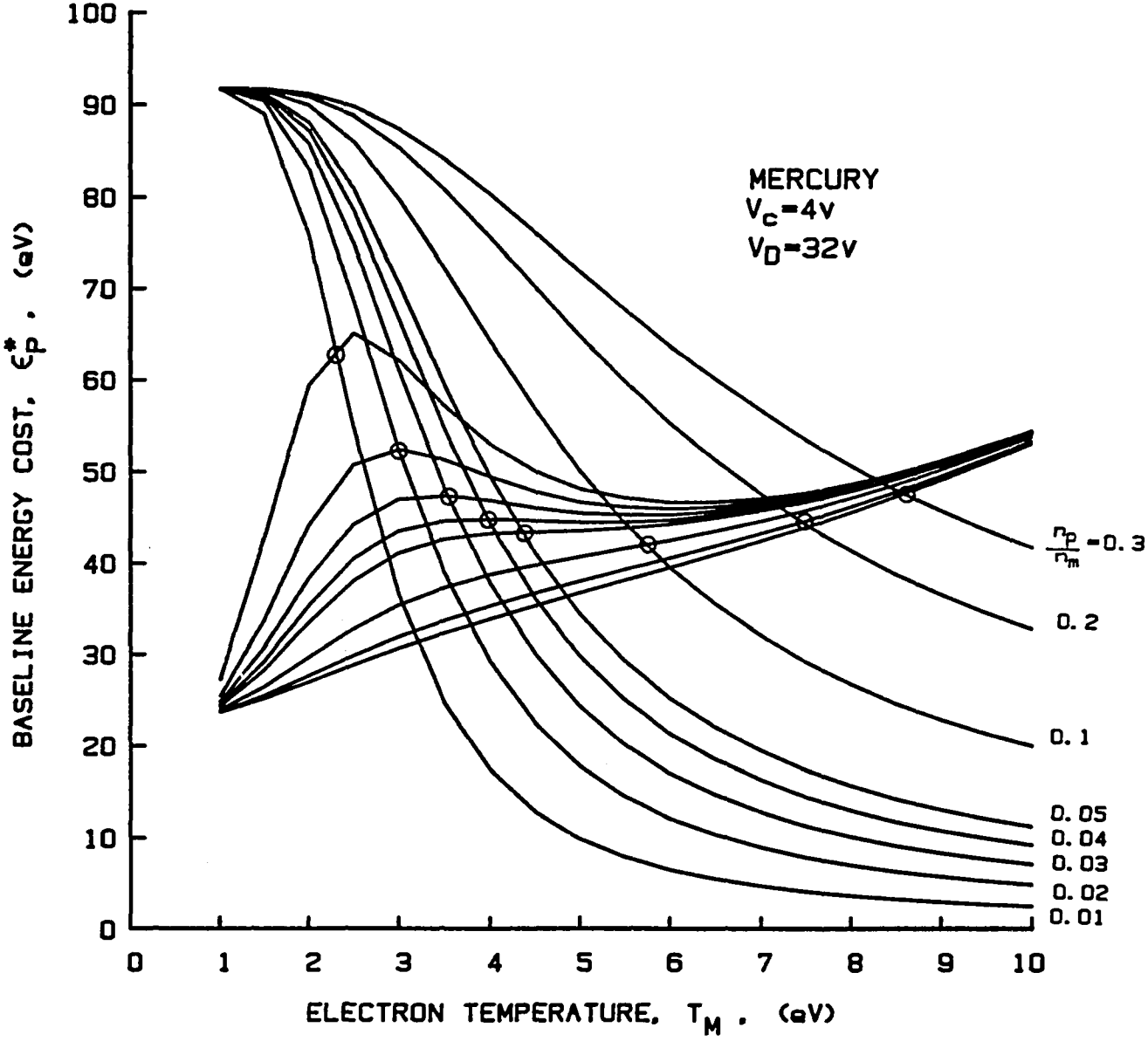

Fig. 50 Baseline Plasma Ion Energy Cost Data for V_c = 4 v

density ratio at this operating condition would be 0.075. Results obtained in a similar manner for the cases where the electron source potential is 8 v and 12 v are given in Figs. 51 and 52 respectively. It is interesting to note that the minimum baseline plasma ion energy cost is realized for electron temperatures near 5 eV in all three of these figures and this value is typical of electron temperatures measured in mercury discharge chambers at normal operating conditions.

Results

30 cm Dia. Ring Cusp Thruster Analysis

For this thruster the fraction of ions produced that are directed toward the screen grid is 70%[21] and the effective screen grid transparency to ions is 82%[27]. The extracted ion fraction (f_B) is given by the product of these numbers (57%). If one assumes the fraction of ions produced that are lost to the anode (f_a) is 5% then the fraction lost to cathode potential surfaces (f_c) would be 38%. The baseline beam ion energy cost for this thruster[22] operating at a discharge voltage (V_D) of 32v and a beam current (J_B) of 2.0A is 118 eV/ion. The equation describing the beam ion energy cost for operation at constant beam current (J_B) is[2]

$$\varepsilon_B = \frac{\varepsilon_p^*}{f_B\left[1 - \exp\left\{-C_o J_B\left(\frac{1}{\eta_u} - 1\right)\right\}\right]} + \frac{f_c}{f_B} V_D. \qquad (10)$$

The baseline beam ion energy cost would be observed for the case where $\eta_u \ll 1$. Under this condition Eq. (10) becomes

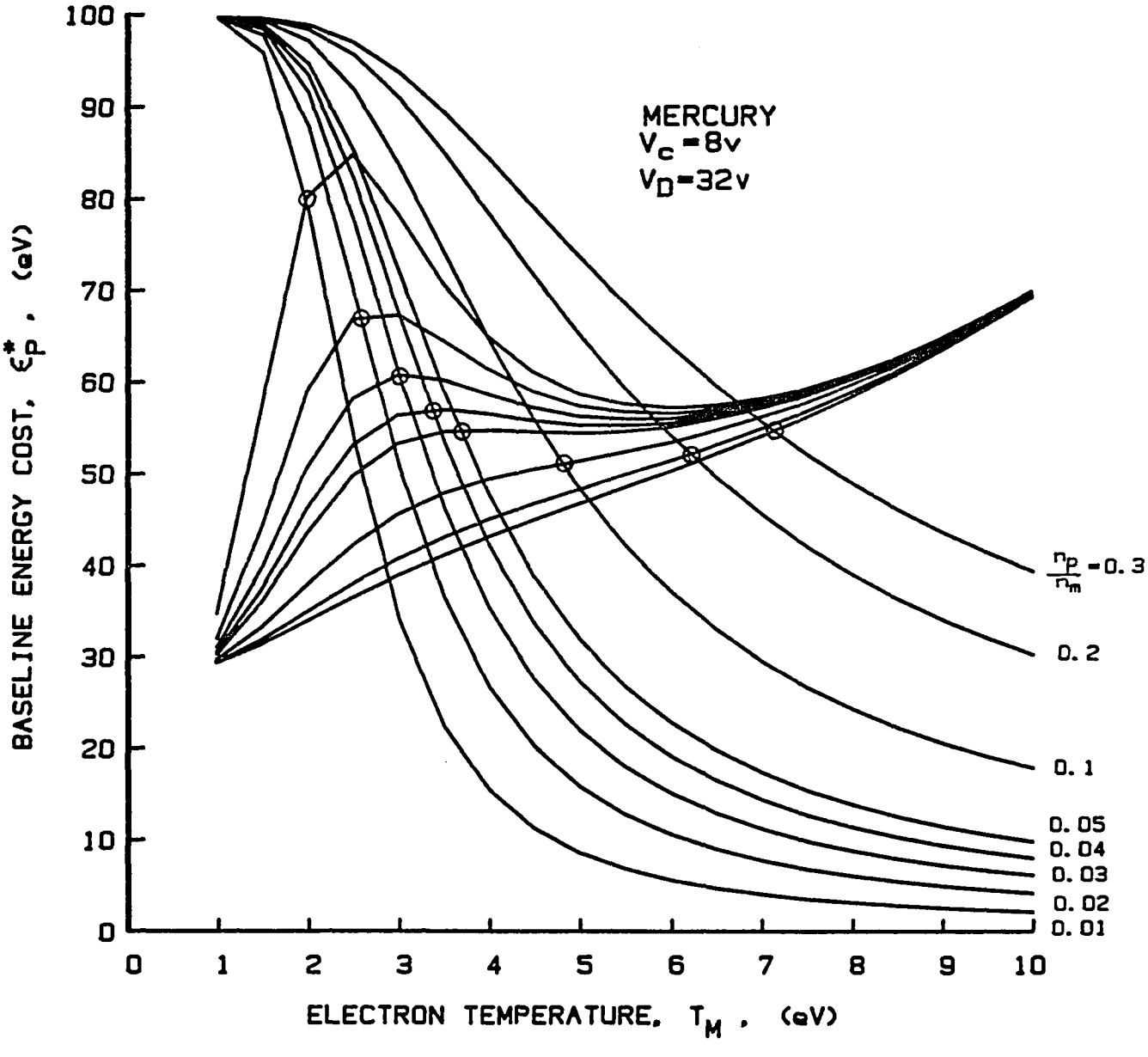

Fig. 51 Baseline Plasma Ion Energy Cost Data for V_c = 8 v

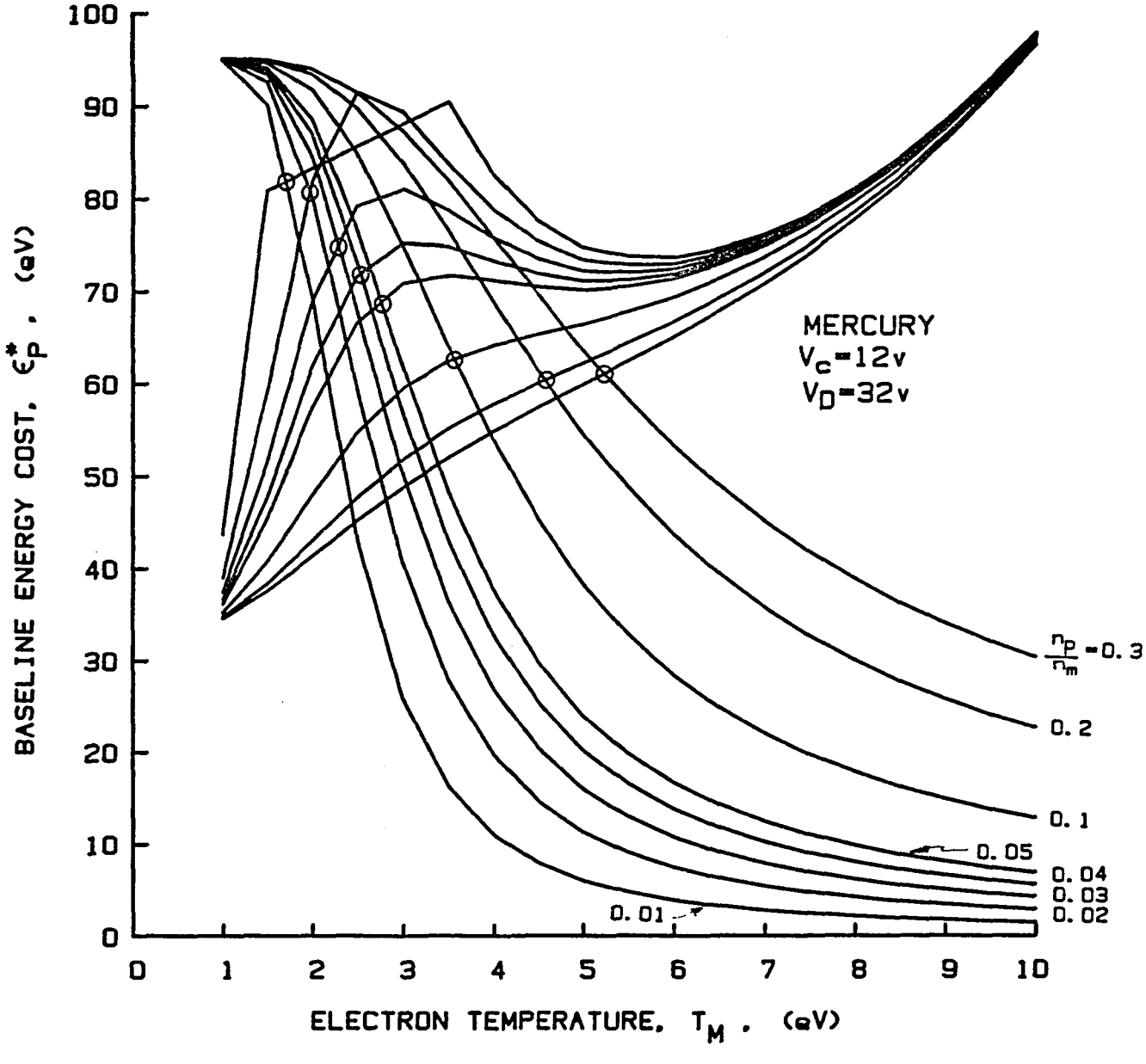

Fig. 52 Baseline Plasma Ion Energy Cost Data for V_c = 12 v

$$\varepsilon_{B_{Baseline}} = \frac{\varepsilon_p^* + f_c V_D}{f_B} \tag{11}$$

Substitution of the numerical values just cited for the ring cusp thruster into this equation for the baseline plasma ion energy cost yields the result

$$\varepsilon_p^* = 55.1 \text{ eV}.$$

In Fig. 53 three performance points measured for the ring cusp thruster[22] are plotted on the usual beam ion energy cost vs. propellant utilization plot. Also shown is the plot of Eq. 10 for the case where the parameters of this equation take on the values which have just been developed and are listed on the figure. It is noted that the value of the primary electron utilization factor (C_o) has been selected to give reasonable agreement with the measured data points shown. The curve is observed to depart from two of the data points. This occurs because both of these points both lie one above the other at a utilization near 90% and the model as expressed by Eq. (10) predicts a near vertical rise only at 100% utilization. The equation could be modified to fit the vertical rise at 90%, but this would imply neutral propellant was being lost at some place other than through the grids. Further, the experimental data points have been corrected for doubly charged ions and their effect has not been considered in the model. This may also help account for the difference between the datapoints and the curve.

The reasonableness of the value of C_o used to obtain the curve of Fig. 53 also deserves some discussion. The value of C_o could be determined using Brophy's model[2] from the equation

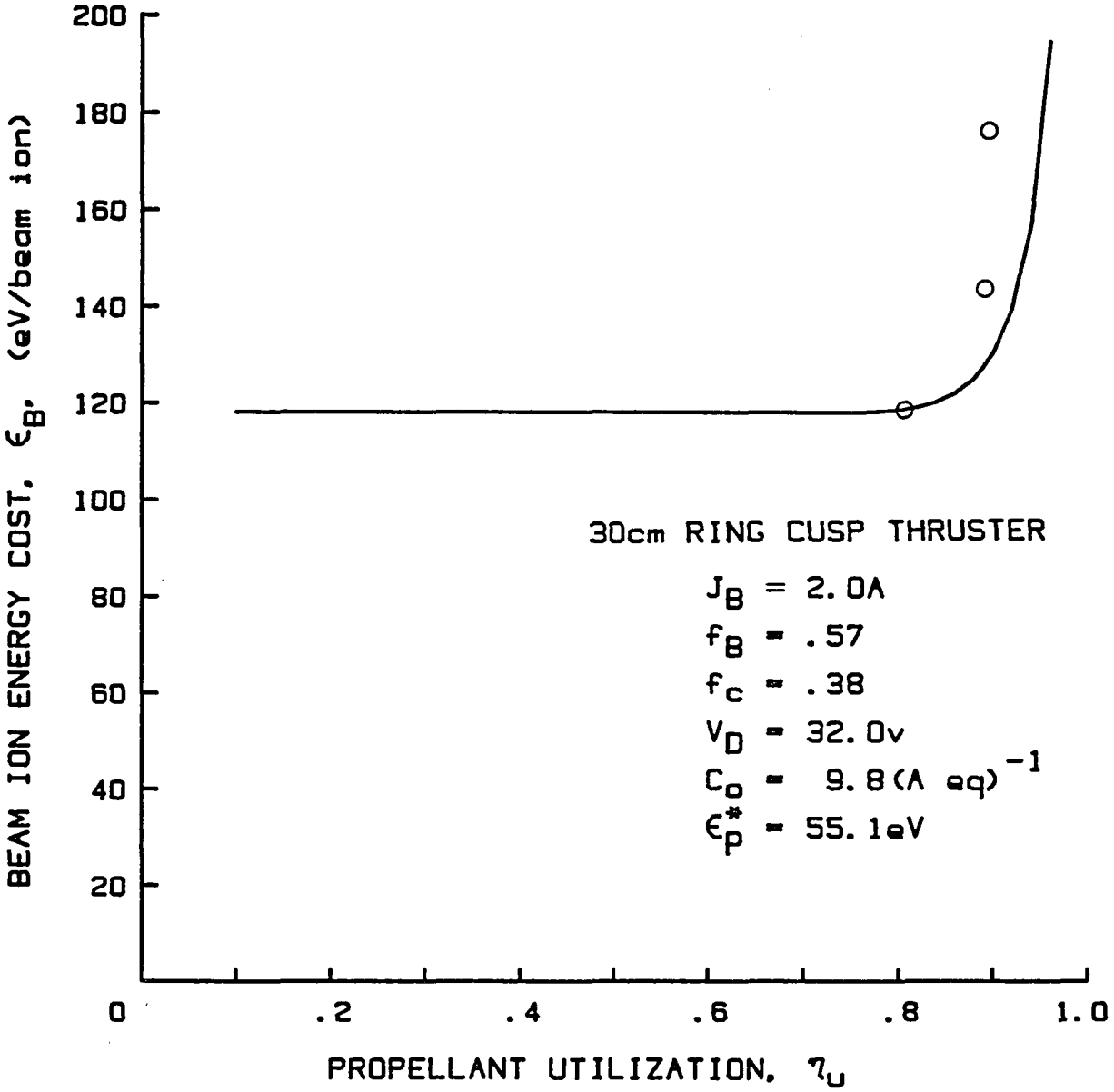

Fig. 53 Performance Curve for 30 cm Ring Cusp Mercury Thruster

$$C_o = \frac{4\,\sigma_o'\,\ell_e}{e\,v_o\,A_g\,\phi_o} \tag{12}$$

but in general the primary electron containment length ℓ_e is not known. One can, however, compare the value of ℓ_e for this mercury thruster of Fig. 53 with the value of this parameter determined by Brophy for a 12 cm dia. xenon thruster. These thrusters both used grids with the same transparency to neutrals (ϕ_o) but they had different grid areas (A_g). They used different propellants so their total inelastic cross sections (σ_o) and their atomic weights (M) appearing in the expression for netural atom thermal velocity (v_o) would differ. The equation for the ratio of containment lengths for these two thrusters obtained from Eq. 12 becomes

$$\frac{\ell_{e_{Hg}}}{\ell_{e_{Xe}}} = \frac{C_{o_{Hg}}}{C_{o_{Xe}}} \quad \frac{\sigma'_{Xe}}{\sigma'_{o_{Hg}}} \quad \sqrt{\frac{M_{Xe}}{M_{Hg}}} \left(\frac{d_{Hg}}{d_{Xe}}\right)^2 \tag{13}$$

where d represents the diameter of the beam. Substitution of numerical values using cross section data from Ref. 2 for xenon and Fig. 48 for mercury yields

$$\frac{\ell_{e_{Hg}}}{\ell_{e_{Xe}}} = 2.25.$$

This number is quite reasonable as it would be expected to be near the ratio of the beam diameters (2.5) which should be close to the ratio of the average distance a primary electron would travel between encounters with the plasma confining boundaries of these thrusters.

If one enters Fig. 51 with the value of baseline plasma ion energy cost computed for this thruster (ε_p^* = 55.1 eV/ion) one determines the mean discharge chamber plasma should have a Maxwellian electron temperature of 3.5 eV and primary-to-Maxwellian electron density ratio of 4.5%. These values differ somewhat from the measured mean values[22, 27] of 5 eV and 3% probably because the model of the mercury atom used to develop Figs. 50 - 52 oversimplifies the actual electronic structure of these atoms. It is noted that Fig. 51 has been used in making this comparison because the keeper voltage for the ring cusp thruster[27] with its cathode exposed directly to the discharge plasma is 10 v. It is estimated that the electron source potential (V_c) would be a few volts less than this value (i.e., 8v).

30 cm J-Series Thruster Analysis

Analysis of the J-series thruster operating on mercury, following the same procedure just defined to analyze the ring cusp thruster, has been carried out using the data from Ref. 22. When an ion loss fraction to the anode of 5% was assumed the results of Fig. 54 shown in the legend and the curve identified by ε_p^* = 60 eV were obtained. Measured performance points, identified on Fig. 54 by the circular symbols, are observed to fit this curve well. If it is assumed that electrons are supplied through the baffle aperture of the pole piece at an effective electron source potential of 12 v and the electron temperature measured in the thruster is 5 eV then Fig. 52 suggests the same baseline plasma ion energy (ε_p^*) of 60 eV. It is noted, however, that it also suggests an unreasonably high primary-to-Maxwellian density ratio of 0.25. If one assumes removal of the baffle would induce a reduction in the electron source potential from 12 v to the 8 v value that might be typical of the cathode region plasma and the electron temperature would remain unchanged at 5 eV then Fig 51 suggests

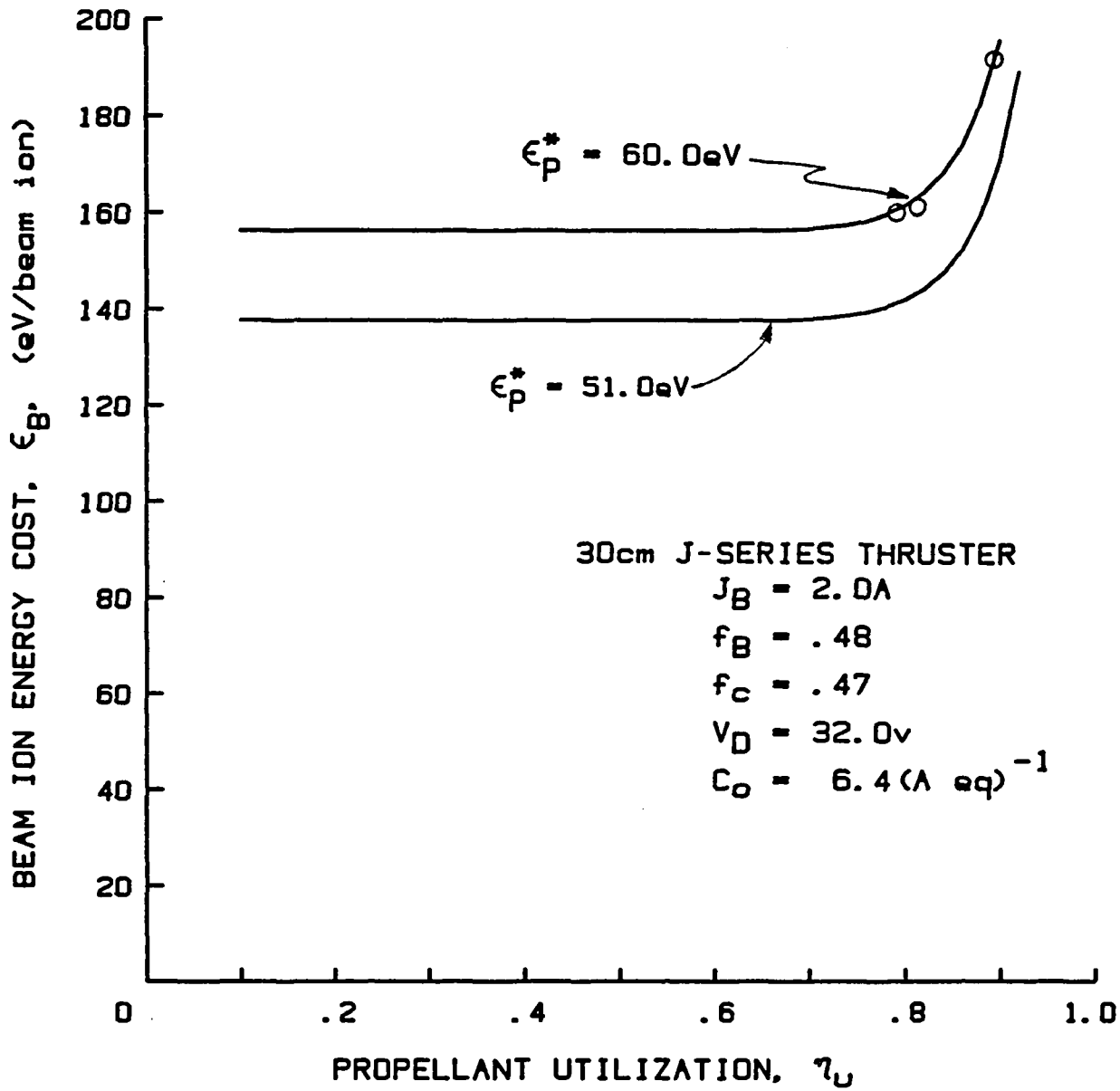

Fig. 54 Effect of Baffle Removal for 30 cm J-Series Mercury Thruster

baffle removal would cause the baseline plasma ion energy cost would drop to 51 eV. Using this value for ε_p^* in Eq. 10 yields the curve on Fig. 54 labeled $\varepsilon_p^* = 51$ eV. Comparison of this curve with the other one suggests that baffle removal would induce a 20 eV reduction in the beam ion energy cost. It should be noted that the value of C_o associated with the J-Series Thruster (Fig. 54) is about 30% less than the one for the Ring Cusp Thruster (Fig. 53). This is indicative of the improved primary electron containment in ring cusp thrusters.

Comparison of Mercury and Xenon Plasma Ion Energy Costs

The electronic strutures of mercury and xenon atoms differ and as a result one would expect the baseline plasma ion energy costs ε_p^* to differ for these two propellants. Values of this parameter obtained using Eqs. 7, 8 and 9 and the data of Figs. 48 and 49 for mercury can be compared with values obtained using corresponding data and equations from Ref. 2 for xenon. The ionization and excitation input data which are also required as input are as follows:

	Mercury[24]	Xenon[29]
Ionization Energy (U_+)	10.4 eV	12.1 eV
Lowest Excited State Energy (U_ℓ)	4.5 eV	8.3 eV
Lumped Excitation Energy (U_{ex})	4.5 eV	10.2 eV

It should be noted in looking at these data that the lumped excitation energy for mercury is equal to the excitation energy associated with its lowest excited state (4.5 eV). For xenon, however, the lowest excited state energy is 8.3 eV and in a case like this where the lowest excited state energy is greater than 45% of the ionization energy Dugan and Sovie[24] suggest the lumped excitation energy should be the mean of the ionization and lowest excited state energies.

It is apparent from these data that while it takes less energy to ionize mercury than xenon the lower threshold energy levels for excitation of mercury may still result in losses that will cause the plasma ion energy costs for mercury to be greater than those for xenon.

When Eqs. 7, 8 and 9 are solved using the mercury data of Figs. 48 and 49 plots like those in Figs. 50 to 52 are obtained. The solution of interest is then obtained by joining the circled intersections obtained from these plots. This yields the variation in baseline plasma ion energy cost as a function of Maxwellian electron temperature. When this is done for a typical mercury operating condition; a discharge voltage (V_D) of 30v and an electron source potential (V_c) of zero the centerline curve shown in the upper plot of Fig. 55 is obtained. Increasing the discharge voltage to 35 v and 40 v results in the centerline curves appearing the other two plots. The solid curves in this figure pertain to xenon at the same operating conditions and they are based on the data from Ref. 2. These curves however utilize the equation

$$\varepsilon_M = \frac{4}{3} T_M + 2 \qquad (14)$$

in place of Eq. 9 because this equation has been shown to describe the energy collection rate associated with Maxwellian electrons at the anode for xenon.[2] Since Eq. 9 has not been verified by direct measurements for mercury Eq. (14) was also applied to the mercury analysis to obtain the dashed curves shown in Fig. 55.

Collectively the data of Fig. 55 show that the baseline plasma ion energy cost is sensitive to the model applied to the Maxwellian electron collection process ($\varepsilon_M = f(T_M)$). They also indicate that the xenon baseline plasma ion energy cost could be either greater or less than that for mercury. At a typical

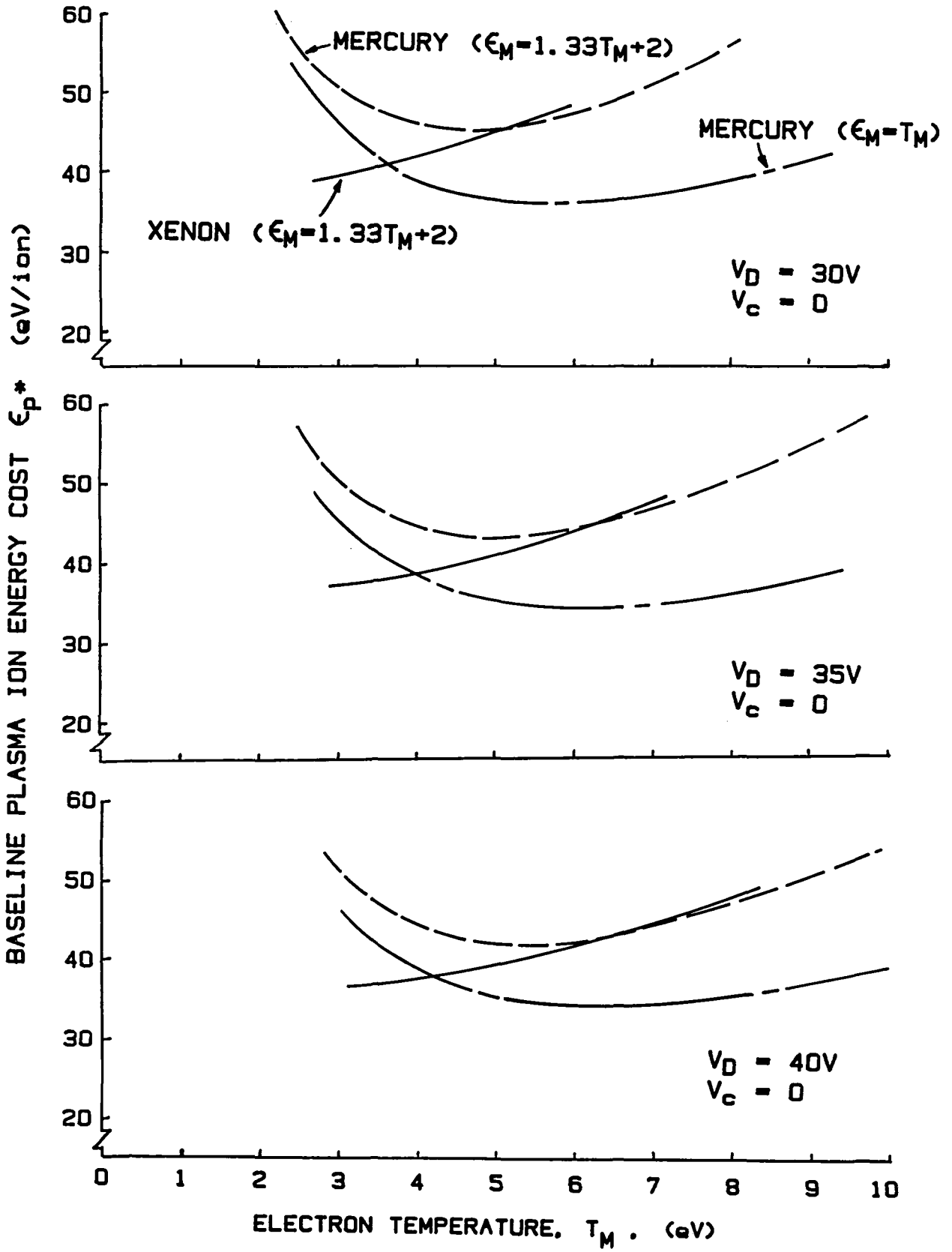

Fig. 55 Effect of Propellant on Baseline Plasma Ion Energy Cost

mercury discharge electron temperature of 5 eV and a typical xenon discharge electron temperature of 3 eV (c.f. Ref. 2) the data of Fig. 55 suggest the xenon baseline plasma ion energy cost would be less than that for mercury if the Eq. (12) model for electron collection were used and that they would be about the same if the Eq. (9) model were used.

Conclusions

The analysis performed to determine the baseline plasma ion energy costs for mercury has required a number of assumptions that make the accuracy of the results uncertain. Further a lumped excitation cross section has been used and no ionization from excited states has been considered. Since analysis[28] suggests substantial excitation from excited states does occur in mercury this introduces still greater uncertainty. In spite of these shortcomings the model generally yields theoretical results that are in reasonable agreement with data measured on a 30 cm dia. mercury ring cusp thruster and a J-series thruster. The analysis suggests that removal of the baffle on a J-series thruster might be expected to induce a reduction in beam ion energy cost of 20 eV/ion. A comparative analysis for mercury and xenon propellants suggests that xenon may actually exhibit a lower baseline plasma ion energy cost than mercury and this in turn implies that the traditional performance curve (eV/beam ion vs. utilization) for a xenon thruster could be better than the one for a mercury thruster.

REFERENCES

1. Brophy, J.R. and Wilbur, P.J. "The Flexible Magnetic Field Thruster," J. Spacecraft and Rockets, Vol. 20, No. 6, Nov.-Dec. 1983.

2. Brophy, John R., "Ion Thruster Performance Model," NASA CR-174810, Dec. 1984.

3. Sovey, J.S., "Improved Ion Containment Using a Ring-Cusp Ion Thruster," AIAA Paper No. 82-1928, Nov. 1982.

4. Wilbur, P.J., "Advanced Ion Thruster Research," NASA CR-174862, pp. 5-33 and 56, Jan. 1985.

5. Hiatt, J.M. and Wilbur, P.J. "Ring Cusp Discharge Chamber Performance Optmization," AIAA Paper 85-2007, Alexandria, Va., Oct. 1985.

6. Longhurst, G.R. and Wilbur, P.J., "Plasma Property and Performance Prediction for Mercury Ion Thrusters," Electric Propulsion and Its Application to Space Missions, Vol. 79 of Progress in Astronautics and Aeronautics, 1981.

7. King, H.J. et. al., "2 1/2 kw Low Specific Impulse, Hollow Cathode Thruster," AIAA Paper No. 69-300, March 3-5, 1969.

8. Robinson, R.S. "Physical Processes in Directed Ion Beam Sputtering," NASA CR-159567, pp.14-20, March 1979.

9. Wilbur, P.J., "Correlation of Ion and Beam Current Densities in Kaufman Thrusters," J. Spacecraft and Rockets, Vol. 10, No.9, Sept. 1973, pp. 623-624.

10. Beattie, J.R. and Wilbur, P.J., "Cusped Magnetic Field Mercury Ion Thruster," NASA CR-135047, July, 1976.

11. McCoy, J.E. "Electrodynamic Tether Applications - Massive Tether Dynamics Study," NASA-JSC, General Status Review, May 3, 1984.

12. von Tiesenhausen, G., et. al. "The Roles of Tethers on Space Station," NASA TM-86519, Oct. 1985.

13. Siegfried, D.E. "A Phenomenological Model for Orificed Hollow Cathodes," NASA CR-168026, Dec. 1982.

14. Sisson, J.M. "Development Status of First Tethered Satellite System," AIAA Paper 86-0049, Jan. 6-9, 1986, Reno, Nevada.

15. Aston, G., "Ion Extraction from a Plasma," NASA CR-1159849, June 1980, pp. 12-19.

16. Kerslake, W.R. and L. R. Ignaczak, "SERT II 1980 Extended Flight Thruster Experiments," AIAA Paper 81-0665, AIAA 15th Electric Propulsion Conf., Las Vegas, NV, 1981.

17. Kerslake, W.R., "SERT II Thrusters - Still Ticking after Eleven Years," AIAA Paper 811-1539, AIAA 17th Joint Propulsion Conference, Colorado Springs, CO, 1981.

18. Langmuir, I., "The Interaction of Electron and Positive Ion Space Charges in Cathode Sheaths," Phys. Rev., V. 33, p. 954, 1929.

19. Wilbur, P.J., "Advanced Ion Thruster Research Annual Report," NASA CR-174862, Jan. 1985.

20. Aston, G., private communication, Aug. 1985.

21. Beattie, J.R. and R.L. Poeschel, "Ring Cusp Ion Thrusters," Int'l Electric Propulsion Conference Paper 84-71, Tokyo, Japan 1984.

22. Hughes Research Laboratories, "Inert Gas Ion Thruster Technology - Technical Progress Narrative No. 14," Dec. 1984.

23. Rockwood, S.D., "Elastic and Inelastic Cross Sections for Electron-Hg Scattering from Hg Transport Data," Phys. Rev., V. 8, No. 5, pp. 2348-2358, Nov. 1973.

24. Dugan, J.V. and R.J. Sovie, "Volume Ion Production Costs in Tenuous Plasmas: A General Atom Theory and Detailed Results for Helium" NASA TN D-4150, 1967.

25. Rawlin, V.K., "Reduced Power Processor Requirements for the 30 cm Diameter Hg Ion Thruster," NASA TM 79257 or AIAA Paper 79-2081, Nov. 1979.

26. Kieffer, L.J., "A Compilation of Electron Collision Cross Section Data for Modeling Gas Discharge Lasers," Joint Institute for Laboratory Astrophysics Report 13, Sept. 30, 1973.

27. Beattie, J.R., private communications to P.J. Wilbur, Jan. 16 and 24, 1985.

28. Peters, R.R., and P.J. Wilbur, "A Doubly Charged Ion Model for Ion Thrusters," Journal of Spacecraft and Rockets, v. 14 No. 8, Aug. 1977, pp. 4611-468.

29. Moore, C.E., "Atomic Energy Levels," Nat'l Bur. Stds. (U.S.), Circ. No. 467 (1958).

30. Beattie, J.R. "Numerical Procedure for Analyzing Langmuir Probe Data," AIAA Journal, v. 13, No. 7, July 1975, pp. 950-952.

31. Chen, F.F., "Electric Probes," appears in Plasma Diagnostic Techniques, Huddlestone and Leonard, eds., Academic Press, 1965.

APPENDIX A

THICK SHEATH LANGMUIR PROBE TRACE ANALYSIS

Thomas Laupa

Introduction

Langmuir probes have been used extensively at Colorado State University to determine the properties of the dense plasmas within ion thrusters and hollow cathodes. In these applications they have been found to be reliable and to yield reasonable results. Further, they provide strong output signals without significantly perturbing the plasma. Finally it has been possible to analyze the raw data using simple graphical techniques because the probe dimensions have been large compared to the thin sheaths that develop at the probe surface.

In less dense plasmas, Langmuir probe traces are more difficult to obtain and to analyze. The probes must be made small enough to perturb the plasma minimally, and this results in a weak output signal which can be obscured by noise. Data analysis also becomes more complex; simple graphical techniques cannot be applied because the dimensions of the sheath surrounding the probe can become large compared to the probe. This introduces a complication because a thick sheath grows significantly as probe bias is increased above plasma potential thereby increasing the effective area through which electrons are collected from the plasma.

A system for collecting thick sheath Langmuir probe data in low density plasmas and a computer routine for analyzing these data have been developed. This equipment and software have been used as part of the hollow cathode plasma contactor investigation discussed elsewhere within this report.

Background

It is easier to understand the approach used in thick sheath Langmuir probe data collection and analysis if one considers first the techniques used in thin sheath work. When used in thin sheath situations, Langmuir probes provide milliamperes of output and high signal-to-noise ratios. Typical raw data for a Maxwellian plasma follow the trend of the plot shown in Fig. A1 which can be recorded directly on an X-Y plotter. Once recorded, each thin sheath Langmuir probe trace can be broken into two regions, namely the one in which electrons are retarded as they approach the probe (i.e., where probe potential is less than plasma potential) and the one in which they are accelerated toward it (i.e., where the probe is biased above plasma potential). The intersection of these two portions of the curve defines the value of plasma potential and probe saturation current. This intersection is frequently not clear-cut due to the non-ideal nature of the plasma and the effects of sheath growth for a non-planar probe. However, by extrapolating ideal curve shapes in the manner suggested in Fig. A1, unique values of plasma potential and probe saturation current can generally be defined.

The analysis routine used to interpret thin sheath Langmuir probe traces in typical discharge chamber plasmas has been described by Beattie.[30] The current collected by the probe in the electron retarding region of such a probe trace as a function of probe bias voltage is described by the equation:

$$J_o = J_{po} + J_{po}\left(\frac{V - V_p}{E'}\right) + J_{Mo}\exp\left(\frac{V - V_p}{T_M}\right) \qquad \text{(A1)}$$

where

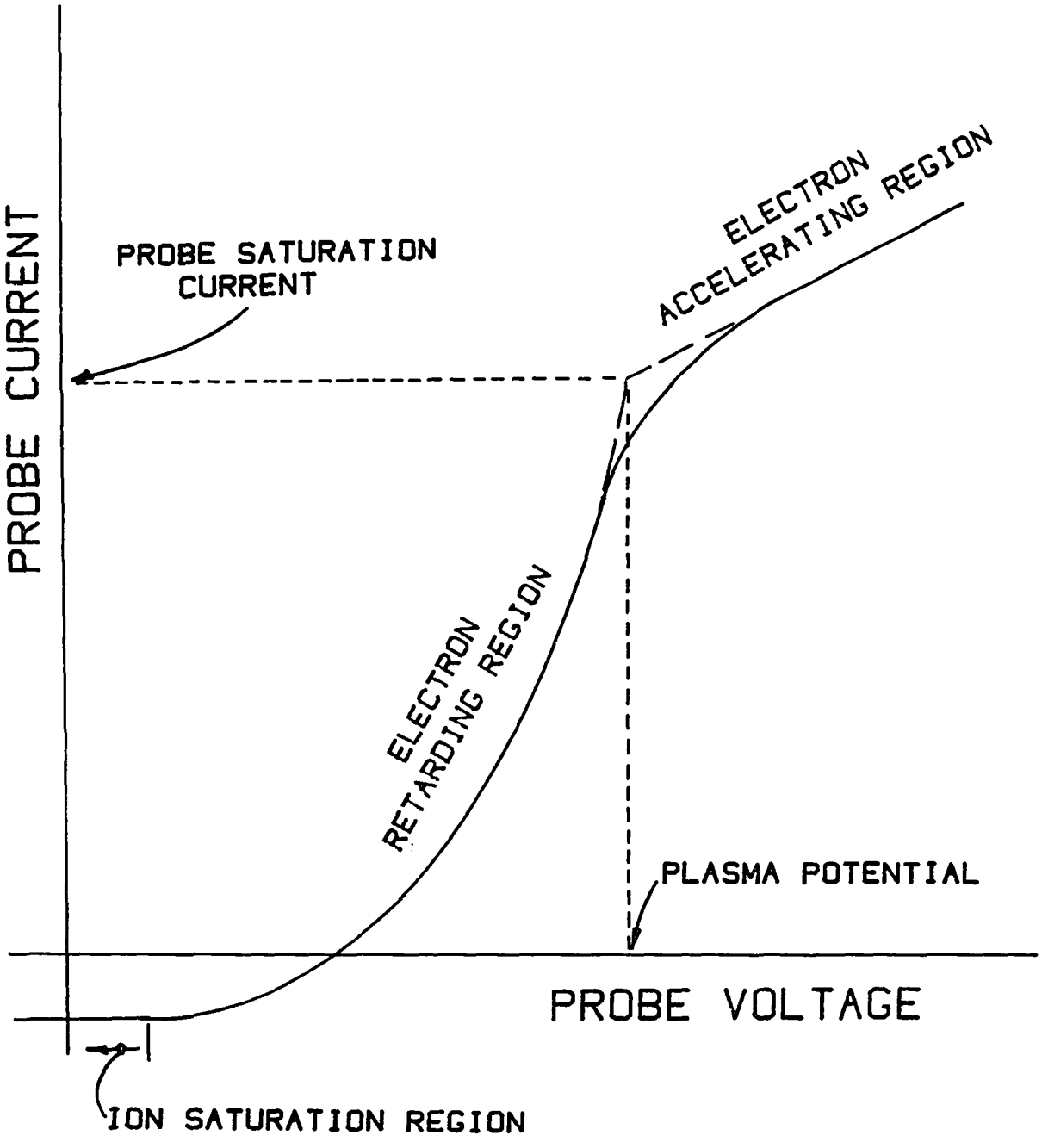

Fig. A1 Thin Sheath Langmuir Probe Trace

$$J_{po} = \frac{n_p e A}{4} \sqrt{\frac{2e E'}{m_e}}, \tag{A2}$$

$$J_{Mo} = \frac{n_M e A}{4} \sqrt{\frac{8 e T_M}{\pi m_e}} \tag{A3}$$

where J_o is the current collected by the probe in the electron retarding region, J_{po} is the portion of probe saturation current contributed by the primary electron group, J_{Mo} is the portion of probe saturation current contributed by the Maxwellian electron group, V is the probe potential, V_p is the plasma potential, E' is the primary electron energy, T_M is the Maxwellian electron temperature, n_p is the primary electron density, n_M is the Maxwellian electron density, e is the electron charge (1.6×10^{-19} coul), A is the area of the probe, and m_e is the electron mass (9.1×10^{-31} kg).

Equation A1 is simply a linear function (the first two terms) added to an exponential function (the last term). Beattie's analysis technique used least squares analysis routine to fit the retarding region data to an equation of the form:

$$J_o = B_o + B_1 V + B_2 \exp (B_3 V) \tag{A4}$$

where B_0 through B_3 are constants determined by the curve fit, and the other terms are as previously defined. B_0 through B_3 were then used by Beattie to calculate the values of T_M, n_M, E', and n_M. The analysis involves the usual assumption that electrons are the majority charge carrier and neglects any

change in ion current that might occur as the probe is biased.

Thick Sheath Data Collection

In order to conduct the plasma contactor work presently underway it has been necessary to both design and build equipment to collect data for the low density plasmas being studied and then to analyze these data. A system for recording Langmuir probe data in plasma densities as low as 10^4 electrons/cm^3 has been fabricated and tested. The spherical probe diameter is sufficiently small (0.533 cm) so that biasing the probe over its full voltage range will not induce any measurable change in the current flowing between the hollow cathode and filaments exposed to the plasma. The small probe generates signals at the microampere level, which are measured and amplified using a picoammeter and then recorded. The system used for recording probe data is shown in Figure A2. The bias power supply shown brings the probe near plasma potential. Once the system is biased near plasma potential, the -18 to +18 volt sweep supply is used to bias the probe through the electron retarding and accelerating regions of the probe trace. The X-Y plotter X-axis input is elevated using the bias supply so it sees only the voltage supplied by the sweep supply. This narrow voltage sweep facilitates adequate plotter sensitivity and therefore adequate precision in the plasma potential and electron temperature results. The picoammeter shown in Fig. A2 measures the electron current collected by the probe and provides an analog output to the Y-axis of the X-Y plotter. Finally, a voltmeter displays the sweep supply bias relative to the reference potential that has been selected (e.g., tank or cathode potential). The reading of the voltmeter is simply marked on the plot at some pen position so the unknown output of the bias power supply can be taken into account. All equipment is shielded and all connections are made with coaxial cable to reduce noise pickup in the system.

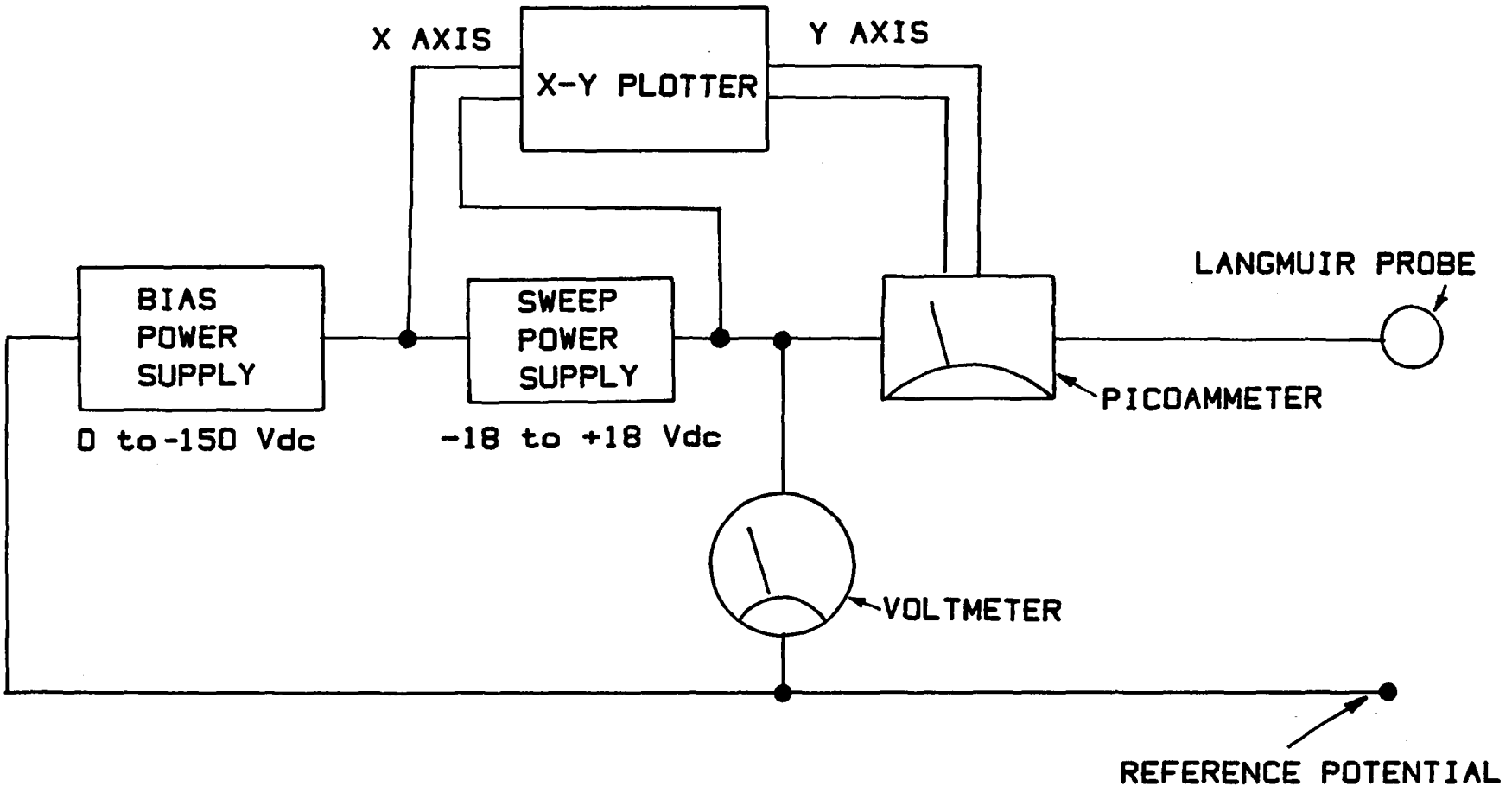

Fig. A2 Langmuir Probe Data Collection Hardware

Thick Sheath Data Analysis

When data are recorded using the system described above, a typical thick sheath probe trace like that shown in Figure A3 is obtained. The trace still consists of two regions, the electron retarding region and the electron accelerating (accel) region, but now it is hard to differentiate between them. Typically, there is no definite inflection point near plasma potential (V_p) making it impossible to locate this potential and probe saturation current by visual examination. Without a value of V_p to define the upper limit of the retarding region, it is not possible to apply directly the multi-variable curve fit (Eq. A4) used in the thin sheath analysis. Thus, the difficulty in analyzing thick sheath probe traces can be reduced to a problem of accurately identifying V_p.

Understanding and describing mathematically the manner in which current is collected to the probe in the accel region leads to a method of finding V_p. When the probe is at plasma potential, no sheath exists around it. As the probe is biased positive of plasma potential, however, a sheath develops and grows thicker as the probe becomes more positive. The area which collects electrons is no longer the actual probe area but the variable surface area of the sheath surrounding it. In a thin sheath situation, on the other hand, the sheath thickness was such that the collection area remained close to the probe area. This caused the collected electron current at plasma potential (saturation current) to remain close to the random electron arrival current to the probe and caused the probe trace to level off in the accel region (Fig. A1). In the thick sheath situation of Fig. A3, however, the sheath thickness becomes large compared to the probe dimension, and the effective electron collection area becomes larger than the original probe area. Thus, the collected electron current continues to increase as the probe is biased positive, and the curve continues upward.

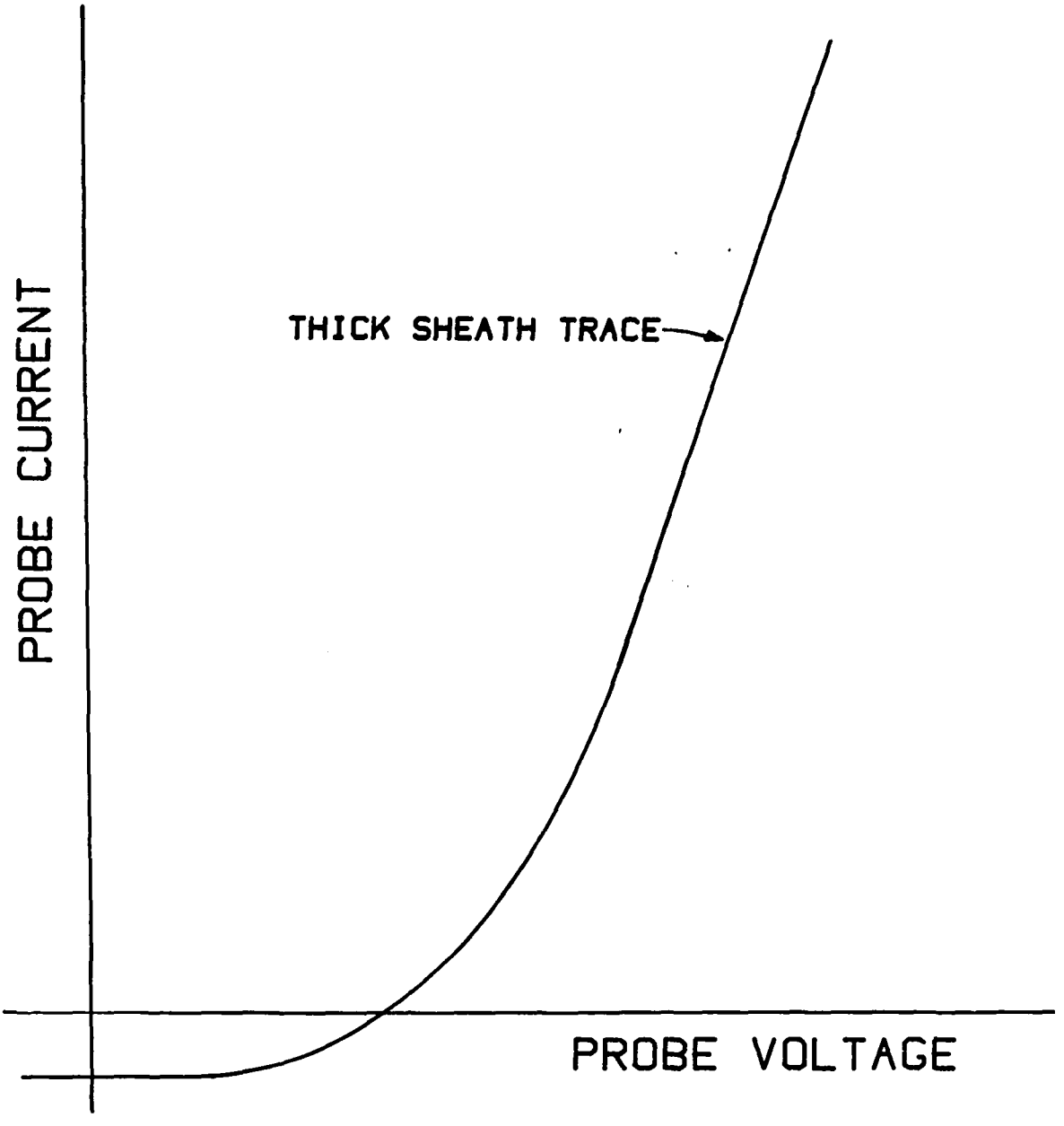

Fig. A3 Thick Sheath Langmuir Probe Trace

For this thick sheath current collection process the current collected by the probe in the accel region (J_A) is decribed in the mathematical expression[31]

$$J_A = J_{po}\left[\frac{V - V_p}{E'} + 1\right] + J_{Mo}\left[\frac{V - V_p}{T_M} + 1\right] \qquad (A5)$$

where all terms have been previously defined. This equation indicates that as the probe is biased positive of plasma potential, the sheath expands at a rate that causes the current collected by the probe to increase linearly.

Equation (A5) can be written in the form:

$$J_A = C_C V + \text{Constant} \qquad (A6)$$

where C_C is the calculated slope of the accel region. It can be determined using the following expression obtained from Eqs. A2, A3, A5, and A6:

$$C_C = \frac{e^{3/2} A}{\sqrt{8 m_e}}\left[\frac{2n_M}{\sqrt{\pi T_M}} + \frac{n_p}{\sqrt{E'}}\right] \qquad (A7)$$

Equation A7 is the key to determining plasma potential thereby defining the boundary between the retarding and accel regions. The slope for the accel region is calculated from plasma properties determined by analysis of an assumed retarding region. When this calculated slope agrees with the slope actually measured, the limit of the retarding region, and thus the plasma potential, has

been correctly chosen. The actual procedure used to accomplish this utilizes the computer routine suggested by the flowchart of Figure A4. As this flowchart suggests the data recorded using the hardware of Fig. A2 are first digitized to prepare it for computer analysis. The plot is then converted to a semilog plot which the operator views to make an initial guess of V_p. A line is fitted to the accel region data as defined by the guess of V_p which has a slope designated C_a. Next, a multi-variable curve is fitted to the retarding region data, and as a result the values of B_0, B_1. B_2, and B_3 are determined (Eq. A4). These values are then used to calculate values for T_M, n_M, E' and n_p. These plasma properties, determined from data in the retarding region, are in turn used to calculate the slope of the accel curve (C_c from Eq. A7). The calculated slope (C_c) is then compared to the measured slope (C_a). If the agreement between the slopes is acceptable, the value of V_p is considered valid and the plasma property values are printed. If C_c and C_a do not agree, the routine selects a new value of V_p and the process is repeated until acceptable agreement is realized.

Comparison of Langmuir and Emissive Probe Measurements of Plasma Potential

The validity of the anlysis procedure dicussed here has been checked to a limited extent by comparing emissive and Langmuir probe measurements obtained at what is believed to be the same plasma conditions. The extent of the agreement that has been achieved can be seen by comparing the open and solid symbol data of Fig. 22. The Langmuir and emissive probe data shown in this figure are seen to agree to within about twenty volts. On some occasions the agreement between these measurements have been even poorer than those associated with Fig. 22. More testing is considered necessary to improve the agreement between these two independent measurements of plasma potential.

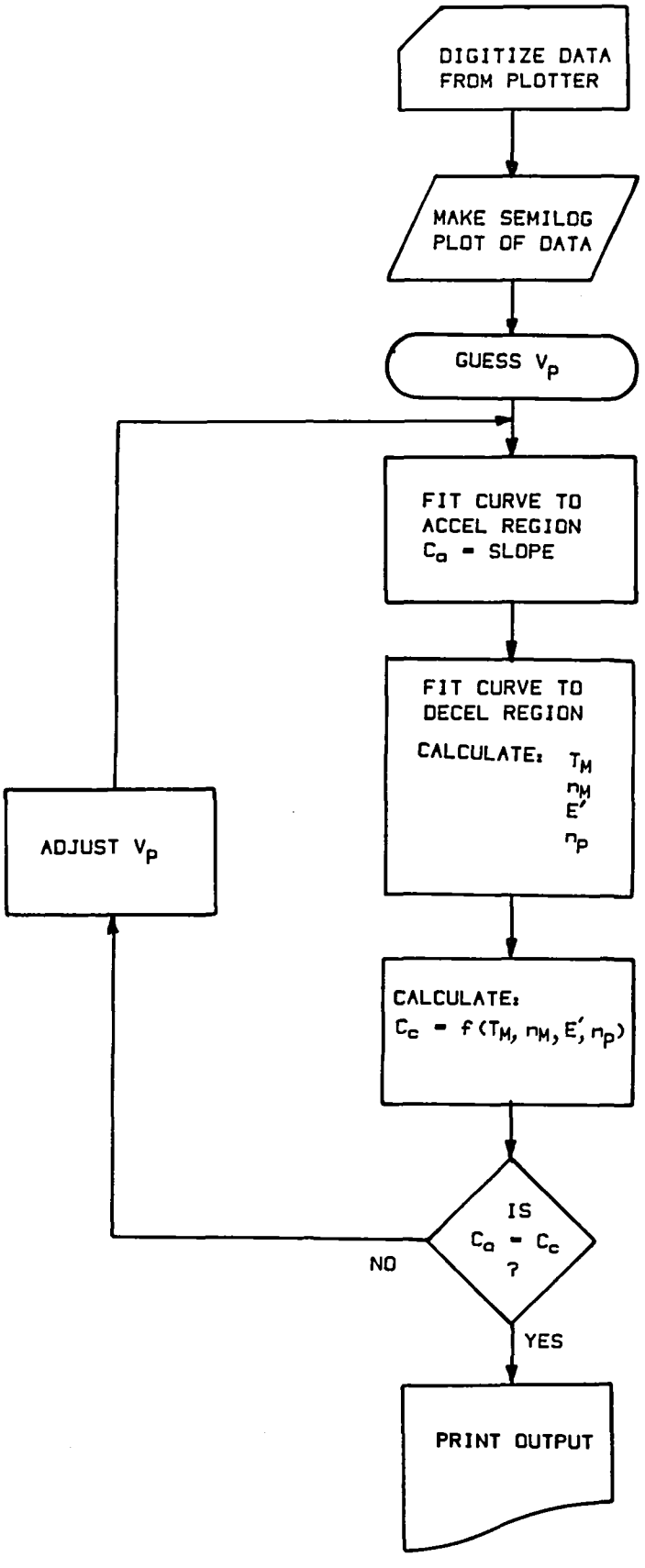

Fig. A4 Thick Sheath Langmuir Probe Trace Analysis Flowchart

DISTRIBUTION LIST

	Copies
National Aeronautics and Space Administration Washington, DC 20546 Attn:	
RP/Mr. Earl E. VanLaningham, MS B600	1
RP/Mr. Robert A. Wasel, MS B600	1
MT/Mr. Edward J. Brazill, MS B326	1
National Aeronautics and Space Administration Lewis Research Center 21000 Brookpark Road Cleveland, OH 44135 Attn:	
Technology Utilization Office, MS 7-3	1
Report Control Office, MS 60-1	1
Library, MS 60-3	2
Mr. N. Musial, MS 500-113	1
Dr. M. Goldstein, Chief Scientist, MS 5-9	1
Mr. Dave Byers, MS 500-219	1
Mr. Frank Berkopec, MS 500-220	1
Mr. Jim Stone, MS 500-219	1
Mr. Vince Rawlin, MS 500-220	10
Mr. Bruce Banks, MS 302-1	1
Mr. Carl Aukerman, MS 500-220	1
Ms. Carolyn Purvis, MS 302-1	1
Mr. Terry Hardy, MS 500-219	10
Mr. Joseph C. Kolecki, MS 302-1	10
National Aeronautics and Space Administration Lyndon B. Johnson Space Center Houston, TX 77058 Attn:	
Mr. Hu Davis	1
Dr. James E. McCoy, Code SN3	1
National Aeronautics and Space Administration Marshall Space Flight Center Huntsville, AL 35812 Attn:	
Mr. Robert Bechtel	1
Dr. Georg von Tiesenhausen	1

Research and Technology Division
Wright-Patterson AFB, OH 45433
Attn:
(ADTN) Mr. Everett Bailey 1

NASA Scientific and Technical
Information Facility
P.O. Box 8757
Baltimore, MD 21240
Attn:
Accessioning Dept. 1

Dept. of the Navy
Office of Naval Research
Universiy of New Mexico
Bandolier Hall West
Albuquerque, NM 87131
Attn:
G. Max Irving 1

Air Force Office of Scientific Research
Bolling AFB
Washington, DC 20332
Attn:
Dr. Robert Vondra 1

Case Western Reserve University
10900 Euclid Avenue
Cleveland, OH 44106
Attn:
Dr. Eli Reshotko 1

DST 1
Ministry of Defence
Metropole Building
Northumberland Avenue
London, WC2 N5BL ENGLAND
Attn:
Dr. D. G. Fearn 1

United Kingdom Atomic Energy Authority
Culham Laboratory
Abingdon, Oxfordshire OX143DB
ENGLAND
Attn:
Dr. P. J. Harbour 1
Dr. A. R. Martin (Rm F4/135) 1

National Aeronautics and Space Administration
Goddard Space Flight Center
Greenbelt, MD 20771
Attn:
Dr. David H. Suddeth 1

COMSAT Laboratories
P.O. Box 115
Clarksburg, MD 20734
Attn:
Mr. B. Free 1

Comsat Corporation
950 L'Enfant Plaza, S.W.
Washington, DC 20024
Attn:
Mr. Sidney O. Metzger 1

Intelsat
490 L'Enfant Plaza, S.W.
Washington, DC 20024
Attn:
Mr. Rolland Schreib 1

Rocket Propulsion Laboratory
Edwards AFB, CA 93523
Attn:
LKDH/Lt. Orin Kilgore 1
LKDH/Lt. Phil Roberts, MS 24 1

DFVLR - Institute fur Plasmadynamik
Technische Universitat Stuttgart
7 Stuttgart-Vaihingen
Allmandstr 124
West Germany
Attn:
Dr. Gerhard Krulle 1

Giessen University
1st Institute of Physics
Giessen, West Germany
Attn:
Professor H. W. Loeb 1

Jet Propulsion Laboratory
4800 Oak Grove Laboratory
Pasadena, CA 91102
Attn:
Technical Library 1
Mr. Jams Graf 1
Dr. Graeme Aston 1
Dr. Dennis Fitzgerald 1
Dr. John Brophy 1

Electro-Optical Systems, Inc.
300 North Halstead
Pasadena, CA 91107
Attn:
Mr. E. James 1
Mr. W. Ramsey 1

TRW Inc.
TRW Systems
One Space Park
Redondo Beach, CA 90278
Attn:
Mr. Sid Zafran 1

National Aeronautics and Space Administration
Ames Research Center
Moffett Field, CA 94035
Attn:
Technical Library 1

National Aeronautics and Space Administration
Langley Research Center
Langley Field Station
Hampton, VA 23365
Attn:
Technical Library 1

Hughes Research Laboratoris
3011 Malibu Canyon Road
Malibu, CA 90265
Attn:
Mr. J. H. Molitor 1
Dr. Jay Hyman, MS RL 57 1
Dr. J. R. Beattie, MS RL 57 1
Dr. J. N. Matossian, MS RL 57 1

Princeton University
Princeton, NJ 08540
Attn:
Dean R. G. Jahn 1
Dr. Arnold Kelly 1

Boeing Aerospace Co.
P. O. Box 3999
Seattle, WA 98124
Attn:
Mr. Donald Grim, MS 8K31 1

Lockheed Missiles and Space Co.
Sunnyvale, CA 94088
Attn:
Dr. William L. Owens
Dept. 57-24 1

Electrotechnical Laboratory
1-1-4, Umezono, Sakura-Mura,
Niihari-Gun
Ibaraki, JAPAN
Attn:
Dr. Katsuya Nakayama 1

Sandia Laboratories
P. O. Box 5800
Albuquerque, NM 87185
Attn:
Mr. Ralph R. Peters, Mail Code 4537 1
Mr. Dean Rovang, Mail Code 1251 1

Ion Tech Inc.
2330 E. Prospect Road
Fort Collins, CO 80525
Attn:
Dr. Gerald C. Isaacson 1
Dr. Dan Siegfried 1

EG & G Idaho
P. O. Box 1625
Idaho Falls, ID 83401
Attn:
Dr. G. R. Longhurst, TSA-104 1

Michigan State University
East Lansing, MI 48824
Attn:
Dr. J. Asmussen 1
Dr. M.C. Hawley 1

The Takagi Research Laboratory
Department of Electronics
Kyoto University
Yoshidahonmachi Sakyo-ku Kyoto 606
JAPAN
Attn:
Dr. Toshinori Takagi 1

Department of Aeronautics
Faculty of Engineering
University of Tokyo
7-3-1, Hongo Bunkyo-ku
Tokyo, JAPAN
Attn:
Prof. Itsuro Kimura 1

Mr. Susumu Masaki
Department of Electronics
Tokyo National Technical College
No. 1220-2
Kunugida-cha, Hachioji 193
Tokyo, JAPAN 1

Dr. Pradosh Ray
Tuskegee Institute
School of Engineering
Tuskegee Institute, AL 36088 1

Dr. M. Krishnan
Dept. of Applied Physics
P. O. Box 2159
Yale Station
New Haven, CT 06520 1

Mr. Lee W. Parker
252 Lexington Road
Concord, MA 01741 1

Dr. Chris Olson
Dept. of Physics
University of Huntsville
Huntsville, AL 35899 1

Dr. Kevin Rudolph
MS M0482
Martin Marietta Aerospace
P. O. Box 179
Denver, CO 80201 1

Dr. Ira Katz
Systems, Science and Software
P. O. Box 1620
LaJolla, CA 92038 1

Dr. David Finkelstein
Physics Department
Georgia Instiiute of Technology
Atlanta, GA 30332 1

Dr. Rod Burton
G-T Devices, Inc.
5705 A General Washington Dr.
Alexandria, VA 22312 1

Instiuto de Pesquisas Espaciais - INPE
Library and Documenation Division
C.P. 515
Sao Jose dos Campos - SP
12200 - BRAZIL 1

Mr. Chuck Crawford
Kimball Physics Inc.
Kimball Hill Road
Wilton, NH 03086 1

Dr. Roy Clampitt
Crawley Mill, Witney
Oxfordshire OX8 5TJ
ENGLAND 1

Mr. Curtis Haynes
Teletronix Inc.
MS 50-431
P. O. Box 500
Beaverton, OR 97077 1

Internal Distribution
Dr. R. S. Robinson 1